November 1987 INT 132/87

LION: A TOROIDAL GLOBAL-WAVE NUMERICAL CODE FOR ICRF HEATING ON JET

JET Article 14 - Contract No JT4/9007

L. Villard, K. Appert, T. Hellsten, J. Vaclavik

FINAL REPORT

JET ARTICLE 14 - CONTRACT No. JT4/9007

between

The JET JOINT UNDERTAKING, Joint European Torus

and

the CENTRE DE RECHERCHES EN PHYSIQUE DES PLASMAS (CRPP)
Association EURATOM - Confédération Suisse

LION: A TOROIDAL GLOBAL-WAVE NUMERICAL CODE FOR ICRF HEATING ON JET

L. Villard, K. Appert, T. Hellsten*, and J. Vaclavik

Centre de Recherches en Physique des Plasmas
Association Euratom - Confédération Suisse
Ecole Polytechnique Fédérale de Lausanne
21, Av. des Bains, CH-1007 Lausanne, Switzerland

* JET Joint Undertaking, Abingdon, OX14 3EA, Great Britain

Table of Contents

1. Executive Summary

1.1 Introduction

In the last few years much effort has been devoted to the theoretical study of wave propagation and absorption in magnetized plasmas [1-8, 13-15], in connection with rf heating experiments. Though the properties of waves in homogeneous and infinite plasmas have been known since a long time [9-11], many difficulties arise when the non-uniformity, the finite size and the actual geometry of the magnetic configuration in the present day experiments are taken into account in the theoretical models.

The limitations which the ray-tracing method suffers from [16,17] and the complexity of analytical methods [18] motivated a new approach to the problem: the global determination of the wave field in inhomogeneous, non-uniformly magnetized, finite size plasmas, using appropriate numerical techniques to solve the pertinent partial differential equations with boundary conditions. By global solution we mean that the problem is solved in one well-defined geometry, with no matching between different regions having different geometries. We also mean that the global solution is the sum of all incident, transmitted, reflected and evanescent waves.

One could summarize the comparison of ray-tracing with global wave methods in the following way. In the Alfvén Wave Range of Frequency (AWRF) the wavelengths are larger than the dimensions of the plasma in the actual experiments. Moreover, in the most interesting region of the spectrum for practical considerations (good coupling and favourable power deposition profile), the fast wave is evanescent through the whole plasma cross-section. Ray tracing is then inapplicable and meaningless, whereas global wave methods yield good results [7,15]. In the high frequency range (Lower Hybrid, Electron Cyclotron), however, the many wavelengths inside the plasma make the global wave field determination more and more difficult. In this case ray-tracing techniques should be more appropriate. In the Ion Cyclotron Range of Frequency (ICRF) both methods have their range of validity. The global wave techniques do not suffer from any fundamental limita-

tion. However, sometimes the numerical convergence is difficult to obtain [4]. On the other hand, ray-tracing suffers in that it is not valid in the evanscent regions or near the resonances. In fact both methods yield similar results in the case of 100% single-pass absorption in large plasmas such as JET [19].

An advantage of the global wave calculation is that it gives the value of the wavefield in a consistent way and thus will make possible further studies such as transport or density fluctuations induced by rf waves.

We have developed a two-dimensional global-wave numerical code for ICRF and Alfvén wave heating in toroidal geometry. Soon after the planning for this work it became known that other codes were already partly operational or under development in the world [1,2,3]. However, ours is the first to solve the partial differential equations relevant for both Alfvén wave and ICRF heating in a toroidal plasma without approximation concerning the geometry [4]. The code has been named LION (Lausanne ION-cyclotron-2-D-toroidal-global-wave-code). It has been implemented on the Harwell CRAY-1 in April 1986 and has been operating successfully since.

The LION code fulfills the requirements of the technical description given in Annex A of the contract. In this report we would like to recall and summarize what the code is able to do and also clearly lay out what its limitations are.

A large part of the work concerning the method and the results of the LION code has already been published [4,6,7,19]. In order to avoid duplicate work only the most important things will be mentioned in this report. We shall extensively refer to published papers, the most important of which is Ref. 4 added to this report as Appendix I where the detailed description of the method and numerical analysis of the results of the LION code are given. This work has been the subject of PhD thesis, written in French [20], where an encompassing analysis has been made of both the physical and numerical properties of our model. The thesis gives more details concerning the variational formulation, the vacuum treatment, the antenna description and the numerical opti-

mization. The behaviour of the resonant surfaces and of the global modes in function of equilibrium parameters is analyzed in both the Alfvén wave and ion cyclotron ranges of frequencies. The main difference in the present work as compared to Ref. 4 is the inclusion of the warm plasma model (see Section 1.2), in other words of the ion cyclotron damping.

In Section 1.2 the main features of the LION code are briefly described. In Section 1.3 a selection of results is presented. Chapter 2 contains all technical information which is necessary to use the LION code on the JET site.

1.2 Features of the LION Code

The geometry treated is toroidal with full profiles of equilibrium magnetic field, current density, temperature and plasma density. Up to 10 different ion species can be specified. Data concerning the equilibrium can be obtained in two different ways, at user's choice: either LION is coupled to an equilibrium code, EQLAUS, or it generates a Solovev analytical equilibrium. Note that experimental JET equilibria can be transferred to LION via Blum's interpretation code, thus making possible the study of one particular shot. The poloidal cross-section can have any shape: circular, elliptical, D, racetrack, bean, boomerang, etc. The only limitation is that no x-point is allowed.

The user has the choice between two different plasma models: cold or warm plasma (i.e. including cyclotron absorption). The approximation of vanishing electron inertia is made, thus $E_\parallel = 0$. The basic equations are

$$\left(\mathrm{rot}\ \mathrm{rot}\ \underline{E} - \frac{\omega^2}{c^2}\ \underline{\underline{\varepsilon}}\ \underline{E}\right)_{(N\perp)} = 0 \qquad (1)$$

$$\underline{\underline{\varepsilon}} = \underline{\underline{\varepsilon}}^{(0)} + \frac{\underline{j}_o \cdot \underline{B}_o}{B_o^2}\ \mathrm{rot}_{(N\perp)}; \qquad \underline{\underline{\varepsilon}}^{(0)} = \begin{pmatrix} \varepsilon_{NN} & \varepsilon_{N\perp} \\ -\varepsilon_{N\perp} & \varepsilon_{NN} \end{pmatrix} \qquad (2)$$

$$\varepsilon_{NN}^{(cold)} = \frac{c^2}{c_A^2} \sum_{ions} \frac{f_i}{1-\omega^2/\omega_{ci}^2} \quad ; \quad \varepsilon_{N\perp}^{(cold)} = \frac{c^2}{c_A^2} \sum_{ions} \frac{f_i \omega/\omega_{ci}}{1-\omega^2/\omega_{ci}^2} \qquad (3)$$

$$\varepsilon_{NN}^{(warm)} = \sum_{ions} \frac{\omega^2_{pi}}{2k_\parallel v_{thi}\omega} \left(Z_{1_i} + Z_{-1_i}\right)$$

$$\varepsilon_{N\perp}^{(warm)} = \sum_{ions} \frac{i\omega^2_{pi}}{2k_\parallel v_{thi}\omega} \left(Z_{1_i} - Z_{-1_i}\right) \qquad (4)$$

$$Z_{k_i} = Z\left(\frac{\omega - k\omega_{ci}}{k_\parallel v_{thi}}\right) \; ; \; Z(\xi) = e^{-\xi^2}\left(i\sqrt{\pi} - 2\int_0^\xi e^{t^2} dt\right) \; ; \; k_\parallel = \frac{n}{r}$$

$$f_i = \frac{n_i m_i}{\sum_j n_j m_j} \; ; \; \underline{E} = E_N \underline{e}_N + E_\perp \underline{e}_\perp$$

$$\underline{e}_\parallel = \underline{B}_o / B_o \; ; \; \underline{e}_N = \nabla\psi / \left|\nabla\psi\right| \; ; \; \underline{e}_\perp = \underline{e}_\parallel \times \underline{e}_N \qquad (5)$$

Note that the cold plasma equations are exact for force-free equilibria, but the warm model is not since $k_\parallel$, which is in fact a differential operator due to the finite poloidal field, has been aproximated by n/r in the dielectric tensor where n is the toroidal mode number and r is the distance to the axis of the torus.

The plasma is surrounded by a vacuum domain enclosed in a perfectly conducting shell. Various antenna models can be specified: high-field side (HFS), low-field side (LFS), top and bottom (T-B) or helical. The displacement current has been neglected.

The antenna is modeled by an infinitely thin sheet on which the rf current is prescribed. For LFS antenna, for example, the rf current has been assumed to be purely poloidal. The antenna is defined by its poloidal extension, position of the feeder currents and distance to the plasma surface. The shell is supposed to be infinitely conductive and is defined by its distance to the plasma surface.

To study a real antenna of finite toroidal extension, its current distribution $I(\phi)$ must be decomposed in a toroidal Fourier series:

$$I(\phi) = \sum_n I_n e^{in\phi} \qquad (6)$$

The power of each Fourier component, P_n, is computed with the LION code. The total power is $P_{tot} = \sum P_n$ and the antenna impedance is $Z = 2P_{tot}/I_{ant}^2$, where I_{ant} is the amplitude of the total rf current.

The equations are written in a variational form in toroidal magnetic coordinates and solved numerically using non-conformal, non-polluting first order finite hybrid elements [4]. The discretization is made on a general irregular mesh. The packing of the mesh points is at user's choice. The code is vectorized in most parts, with a gain due to vectorization of at least 10. Its structure consists of five programmes communicating through a disk data base (see Section 2.1). The maximum number of mesh cells which can be handled on a CRAY-1 is 40000, the limitation being due to disk space requirements. A calculation with 5000 cells necessitates 50 s CP and with 12800 cells 160 s CP. The central memory (CM) and disk space (DS) requirements are

$$CM = 18\ N_{pol}^2 + 4N_\psi N_{pol} \qquad (7)$$

and

$$DS = 18\ N_\psi N_{pol}^2 \qquad (8)$$

where N_ψ and N_{pol} are the radial and poloidal number of intervals, respectively.

As output the code produces tables and graphs of the solution, the Poynting vector, the power absorption density, the power absorption density averaged over magnetic surfaces, the poloidal Fourier decomposition of the solution, the polarizations, etc. Note that the version of LION installed at JET uses the GHOST-80 graphical routines package.

A user's manual, complete tables of subprogrammes and Fortran COMMON variables, description of input and output data are given in Appendix II. The code satisfies the standards for computer programmes used for JET (Contract, Annex B).

1.3 Summary of results

a) Testing the code

Extensive numerical convergence studies have been performed [4] showing the sane numerical properties of the code, but also giving a measure of the accuracy of the results. In some cases the structure of the solution is so complicated that the convergence laws are not satisfied within the limitations imposed by eq. (8). The user should, therefore, be very careful when interpreting results obtained with LION.

The code has also been tested [4] in the limit of high aspect ratio where an analytic dispersion relation can be derived. Another limit is the ideal MHD ($\omega/\omega_{ci} \to 0$) with finite aspect ratio where a comparison with another toroidal code (ERATO) has successfully been made.

For more details concerning the numerical properties of LION, see Ref. [4].

b) General physical results

The results of the LION code have shown that in both the Alfvén and ion-cyclotron ranges of frequencies the perpendicular resonances of the cold plasma fast wave lie on ψ = const. surfaces. We have thus confirmed a previous analytical work [5]. For ICRF it is only in the limit of the poloidal field going to zero that the usual picture is recovered: the resonances shrink in the poloidal direction and merge with one another, yielding a vertical resonance structure [6].

We have also shown a continuous transition from Alfvén Wave Heating (AWH) to ICRF by introducing a heavy minority species so that the

original Alfvén resonant surfaces split to produce Alfvén and ion-ion hybrid resonances [6].

We have also studied the influence of the equilibrium current profile on the power deposition. For AWH we have confirmed the cylindrical calculations: it is advantageous to select negative toroidal wavenumbers ($n < 0$) and try to select negative poloidal wavenumbers ($m < 0$). However, due to toroidal coupling, it is not possible to excite a pure m mode. Optimizing AWH in a torus is therefore different than in a cylinder: one has to take care of the toroidally-coupled resonance surfaces which usually lie further out than that one would like to excite. However, we have been able to calculate another scenario for AWH where the main and innermost resonant surface is a toroidally coupled one ($m = 0$, the antenna being $m = \pm 1$). Toroidally coupled global Alfvén eigenmodes have been found in complete agreement with the TCA experiment [7]. We have seen that the global Alfvén eigenmodes are sensitive to the equilibrium current profile: for some profiles they do not exist. This also is in agreement with the experiment.

For ICRF the influence of the equilibrium current is not as clear as in the Alfvén range of frequencies. Nevertheless we have shown that there is an asymmetry between positive and negative toroidal wave numbers (n).

c) Application to JET

The LION code has been applied to many different ICRF scenarios in JET plasmas: D+7%^{3}He, D+4%H, D+30%H, H+4%D and pure D-plasma. As an example, Fig. 1 shows the solution for a mixture of D+7%^{3}He, $f = 33$ MHz, for one toroidal wave number $n = -15$. Note the imperfect focusing of the fast wave towards the central regions. There is a non-vanishing transmission of the field across the ion-ion resonances, and Alfvén resonances are weakly excited on the high-field side of the plasma. Since WKB calculations for this case predict finite reflection also, we can expect an excitation of global modes. This is confirmed by our calculations. Figure 2 shows the coupled power as a function of the toroidal wavenumber n for a given antenna current $I_n = 1$ (eq. 6). We see that peaks appear at different n's. Note that the JET

antennae excite a broad n spectrum. Thus one can expect that many global modes are simultaneously excited. It is therefore not sure whether in this case the global modes would be seen as peaks in the loading of the antenna! If we now study the power for one toroidal wavenumber (n = -15) as a function of the applied frequency, we obtain Fig. 3. Rather broad peaks appear which seem to be composed of many different peaks, though the numerical resolution in this case was not sufficient to resolve them. A 1-D global calculation for the same parameters has shown peaks at the same places as in Fig. 3 but of higher quality. We identify those as different radial modes of the fast wave, the "compound" peaks of Fig. 3 being different poloidal modes coupled by toroidal effects. A further confirmation of this toroidal coupling will be given shortly.

If we let the concentration of ^{3}He go to zero, sharper peaks appear on the loading (not shown) but the average loading remains approximately the same. This is in good agreement with the experiment.

In a case of stronger absorption, like a minority of 4% of H in a D-plasma, the peaks get smoother (Fig. 4). Note that the real antenna loading curve, made of the superposition of all toroidal wavenumbers n, in this case would appear completely flat. The value of the antenna load, however, depends on macroscopic quantities such as the density or the distance between plasma and antenna.

Let us now consider the case of a large minority concentration, 30% of H in a D-plasma. The power absorbed for one toroidal wavenumber (n = -15), plotted as a function of the applied frequency, shows a host of sharp peaks (Fig. 5). This is a consequence of the strong reflection occuring on the low-field side of the resonances. To give an interpretation of these peaks, we show the wave field solution corresponding to a "main peak", f = 42.85 MHz, in Fig. 6 and to a "satellite peak", f = 42.24 MHz, in Fig. 7. In both cases the wave field is confined between the antenna and the reflection region. If we compare Figs. 6 and 7, we see that the same radial wavenumber is excited but with different poloidal wavenumbers.

We have also computed, for the same scenario, the power coupling spectrum excited by other types of antennae: the "top-bottom (T/B)" and the "high field side" (HFS) antennae. The result is shown in Fig. 8. For the T/B antennae the coupling is not bad but unfortunately much of the power is absorbed near the plasma boundary in front of the antennae (not shown). We see that global modes are excited, though at different places than for the LFS antenna (compare Figs. 5 and 8). For HFS antenna no global modes are excited (since there is no reflection), the power deposition profile is well centred (not shown), but the coupling is miserable (see Fig. 8, bottom curve). The ratio of reactive over resistive powers is of the order of 400! This astonishing result is an effect of the toroidal geometry. The parallel wavenumber, which can be approximated by n/r, is 2.4 times larger on the HFS edge of the plasma than on the LFS. Consequently the fast wave is evanescent over 25 cm on the HFS but only over 2.5 cm on the LFS. This strong evanescence reduces the amplitude of the field by a factor of the order of 6 and consequently the total power by a factor of the order of 36. This factor is just the ratio between the average LFS and HFS couplings. Since the single-pass absorption for HFS is almost 100% there is no possibility for the wave to build up an eigenmode, which would increase the coupling.

From our studies we see that a large number of modes is excited by the JET antennae. We have also given an explanation why these modes may not be seen on the loading response of the antenna: due to the very broad toroidal spectrum (Fig. 2) and due to the coupling of different poloidal modes by toroidal effects (Figs. 5, 6 and 7), the antenna "sees" only an average over all different excited modes.

We have compared different scenarios, deuterium and hydrogen or helium-3 minority, changing the concentration of the minority species, the density and the density profile. We have found that the coupling of the LFS antenna, when averaged over the variations due to the presence of global modes (if any), is independent of the scenario used. However, the coupling depends on the density near the edge of the plasma and the distance between the plasma and the antenna: it is larger with high edge density and with shorter plasma-antenna distance. This can be understood in terms of the evanescence of the

fast wave at low density and in vacuum. Thus the coupling mainly depends on the distance between the antenna and the fast wave cutoff at low density. This result of the LION code is in agreement with the JET experiment.

Let us now consider a minority heating scheme where all the absorption is given by ion cyclotron damping. The plasma consists of deuterium and hydrogen with $n_H/n_D = 4\%$. The parameters are the following: $n_{Do} = 4 \cdot 10^{19} m^{-3}$, $R_o = 3m$, $a = 1.25m$, $b = 2.1m$, $B_o = 2T$, $f = 30$ MHz ($\omega = \omega_{cH}$ on magnetic axis). The warm plasma model is used with central temperatures $T_{Do} = T_{Ho} = 5$ keV. We examine first a single toroidal wavenumber, $n = 25$. In Fig. 9a we show the Poynting flux across the magnetic surfaces,

$$P_S(\phi) = \int_{\phi=\text{const}} \mathrm{Re}(\underline{E}^* \times \underline{B}) \cdot \underline{d\sigma} \ , \qquad (9)$$

as a function of the radial coordinate s which labels the magnetic surfaces. In fact s is proportional to $\sqrt{\phi}$ and goes from 0 on the magnetic axis to 1 at the plasma surface. It is almost proportional to the minor radius in the equatorial plane. We can see from Fig. 9a that 50% of the total power delivered by the antenna is absorbed inside the surface $s = 0.18$, which is the surface that passes at 22.5 cm from magnetic axis on the equatorial plane. Also shown in Fig. 9a is the quantity dP_S/ds. In Fig. 9b we plot the power deposition profile averaged on the magnetic surfaces,

$$P_V = \frac{dP_s(\phi)}{dV(\phi)} = \frac{dP_s}{ds} \frac{ds}{d\phi} \left(\frac{dV}{d\phi}\right)^{-1} \ , \qquad (10)$$

where $P_S(\phi)$ is defined by eq. (9) and $V(\phi)$ is the volume enclosed by a magnetic surface. In Fig. 9b P_V is in units of W/m^3 per Watt of total rf power. Its maximum value is 0.44 W/m^3 on the magnetic axis.

To further document this minority case we show in Fig. 10 a contour plot of the wave field polarization $|E_+| = |E_N + iE_\perp|$. We note that due to the strong Doppler broadening of the hydrogen cyclotron

resonance $|E_+|$ is non-zero at $\omega = \omega_{CH}$. The same calculation but with the cold plasma model shows that in this case there is a screening effect of $|E_+|$ at the cyclotron resonance (Fig. 11). In Fig. 12 we show the real part of E_N and in Fig. 13 the real part of E_ϕ, for the warm case. We notice that the fast wave is not completely focused on the magnetic axis, but there is a non-negligible vertical spread of the wave field along the cyclotron resonance. This lack of focusing is an effect of the ellipticity of the cross-section and of the small aspect ratio. It yields a certain vertical extension of the power absorption density in the poloidal plane (Fig. 14). The same calculation but in a circular large aspect ratio (> 5) tokamak leads to good focusing of the fast wave on the magnetic axis and hence a more peaked power deposition profile (not shown).

For the same scenario as in Figs. 9 - 13, but with a toroidal wavenumber n = 10 instead of n = 25, the Doppler broadening of the cyclotron resonance is smaller and the power deposition is more peaked. In this case the maximum value of P_V (eq. 10) is 0.9 W/m^3 on the magnetic axis instead of 0.44 W/m^3 for n = 25. Thus for this scenario we can expect the power deposition profile to be more peaked for the JET monopole antenna (for which n=10 is typical) than for the dipole and quadrupole antennae (for which n=25 is typical). We have also found that the maximum value of P_V can be reduced by a factor 2 by moving the position of the cyclotron layer by only a few percents. Thus central heating is strongly reduced in the case of slightly off-axis resonance. These results of the LION code could and should be compared with the JET experimental results.

In extensively using the LION code in various scenarios, we were able to derive a semi-empirical analytic formula for the power deposition profile [19] in the case of minority heating scenarios. The formula depends only on the calculation of local absorption coefficients and the Doppler broadening of the cyclotron resonance of the minority species. The use of this formula as an input to Fokker Planck codes made possible the study of the process of a high energy tail formation on the velocity distributions of the heated species, its influence on the absorption coefficients, hence on the power deposition profile. A self-consistent steady-state solution for the power deposition profile has been iteratively computed [19].

2. Technical Information

2.1 Structure of the LION code

The LION code is in fact made of five principal programmes communicating through a disk storage data base. Since it uses a real MHD equilibrium it can be connected to the equilibrium code EQLAUS which gives the values of ψ on an equidistant (r,z) mesh. These values are then read by the first programme of LION, LION1. Note that usually a lot of computations with the LION code are made using the same equilibrium. It is then recommended to compute it only once and to store it as a permanent file.

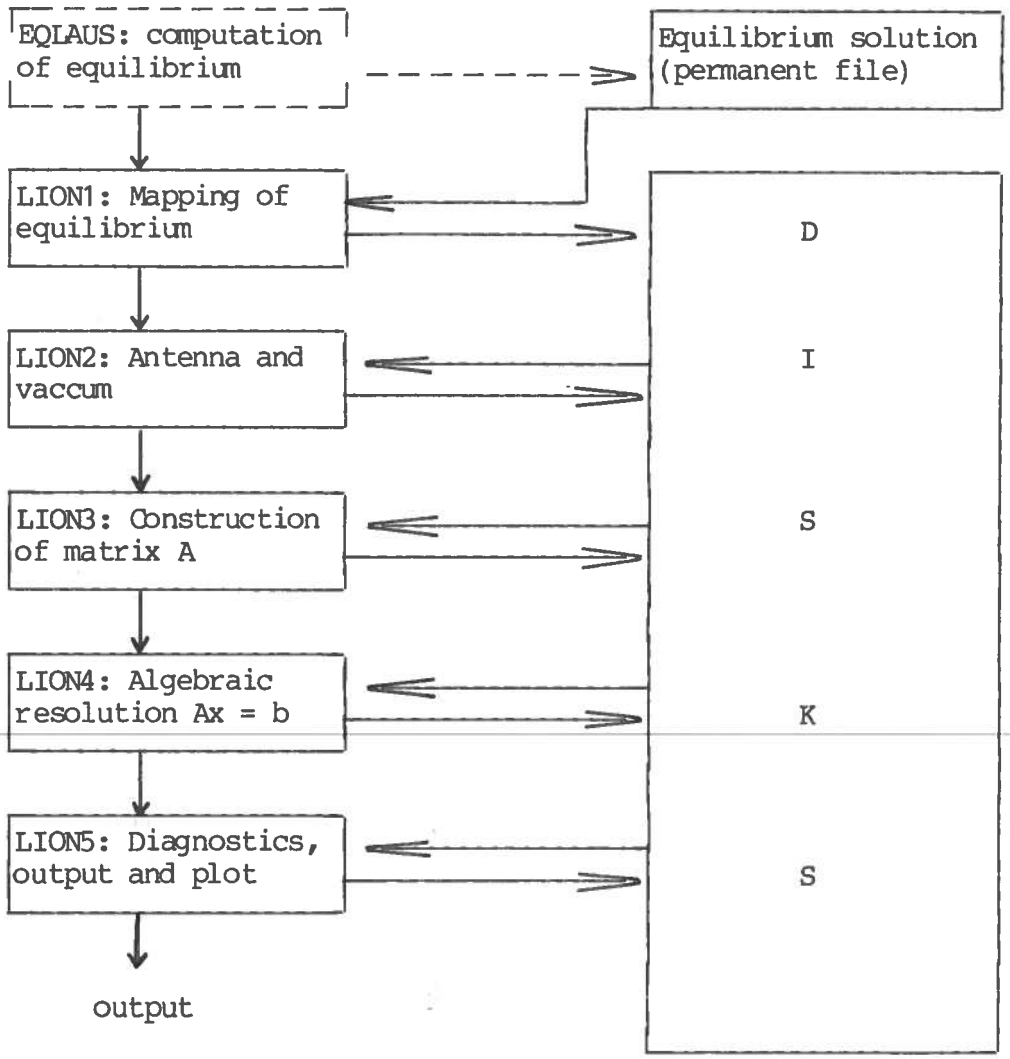

2.2 How to activate and run the LION code

The LION code needs a certain number of files to be resident on the CRAY: the UPDATE library named LION86, the binary library LIBICRH and, if a numerical equilibrium is needed, the file on which the equilibrium solution has been written to. The first step is to check whether these files reside as permanent datasets on the CRAY. If not, then one has to create them by submitting the appropriate jobs to the CRAY (see below, nr 1°, 2°, 3°). If they do, then only operation 4° is necessary to run the LION code.

1°. Create the UPDATE library LION86: submit the job which is contained in the file

JETTHN.LION.CNTL(LIBUP)

2°. Create the binary library LIBICRH: submit

JETTHN.LION.CNTL(L86CORR)

3°. Create a numerical equilibrium: submit

JETTHN.EQERA.CNTL(EQLAUS)

This file contains the input data for the equilibrium code EQLAUS in the NAMELIST EQDATA. Explanations concerning the input variables are given in Section 2.3.

4°. Run the LION code: submit

JETTHN.LION.CNTL(RUN)

This file contains the input data for the LION code in the NAMELIST NEWRUN, which is explained in detail in Section 2.4 and Appendix II. The user can modify the input variables by editing the file JETTHN.LION.CNTL(RUN) and simply change the corresponding values in the NAMELIST NEWRUN.

The mesh size used in the computations is specified by the input variables NPSI (nr. of intervals in the ϕ direction) NCHI (nr. of intervals in the poloidal direction in the upper half-plane; the total nr. is then 2*NCHI-2; the mesh is symmetric with respect to the equatorial plane). The equilibrium solution is given on a (r,z) mesh. We then specify NR (nr. of points in the r direction) and NZ (nr. of points in the z direction in the upper half-plane; the equilibrium is symmetric with respect to the equatorial plane). For a good description of the equilibrium solution which is necessary to have for a given mesh of the LION code it is recommended to compute the equilibrium (action nr. 3^{o}) with a sufficiently large mesh: NR > 3*NPSI, NZ = (NR/2)*ELLIPT. Otherwise numerical convergence is not guaranteed.

The values of NPSI, NCHI, NR and NZ in the NAMELIST NEWRUN cannot be larger than the values of the parameters MDPSI, MDCHI, MDR, MDZ, respectively, which define the array dimensioning and are written in the file JETTHN.LION.CNTL(L86CORR). If a larger mesh is necessary these values must be modified by editing the above-mentioned file. Then this file must be submitted to the CRAY (action nr. 2^{o}) before further runs of the LION code can be performed (action nr.4^{o}) with the desired mesh size.

The output of the LION code consists of line-printer output and graphical plots which are stored as a TRANGRID file in JETTHN.GRAF.TRAN. Description of output and plot is given in Appendix II.

2.3 Normalization for the equilibrium code EQLAUS

The equilibrium code EQLAUS works in normalized units defined by:

- unit length: $R_{o,ph}$, distance from axis of the torus to geometrical centre of the cross-section
- unit magnetic field: $B_{o,ph}$, magnetic field on geometrical centre of cross-section

Therefore the input parameters in the Namelist "EQDATA" must be given according to the following definitions, where the subscript ph denotes the physical units and eq the EQLAUS units:

R0 = 1.0 geometric centre of the plasma cross-section

ASPCT = $a_{ph}/R_{o,ph}$ = a_{eq} inverse aspect ratio

ELLIPT = b_{ph}/a_{ph} = b_{eq}/a_{eq} ellipticity

TRIANG = triangularity δ

$$\text{CURT} = \frac{I_{ph}}{2} \cdot \frac{\mu_o}{R_{o,ph} \cdot B_{o,ph}} = \frac{I_{LION}(\text{scale}=1)}{2}$$

plasma current in half the cross-section

AP,AT : polynomial expressions of $P'_{eqlaus}(\psi)$ and $TT'_{eqlaus}(\psi)$, where p and T/r are the pressure and the toroidal magnetic field so that:

$$P_{ph}(\psi) = \frac{B^2_{o,ph}}{\mu_o} P_{eq}(\psi) \text{ and } T_{ph} = R_{o,ph}\, B_{o,ph}\, T_{eq}(\psi)$$

ASPCT, ELLIPT and TRIANG determine the surface parametrization, which is defined by:

$$\begin{cases} r = R0 + ASPCT * \cos(\theta + TRIANG * \sin\theta) \\ z = ELLIPT * ASPCT * \sin\theta \end{cases}$$

2.4 Normalizations for the LION code

The LION code works in normalized units, defined by:

- unit length: R_o, distance from axis of the torus to magnetic axis.
- unit time: R_o/C_{Ao}, where C_{Ao} is the Alfvén speed on magnetic axis.
- unit mass: ρ_o/R_o^3, where ρ_o is the mass density on magnetic axis.
- unit magnetic field:
  B_o, equilibrium magnetic field on magnetic axis.

All other normalized quantities are defined in function of the four above. For example, we have :

- unit current density: $B_o/(\mu_o R_o)$
- unit electric field : $B_o C_{Ao}$
- unit current: $R_o B_o/\mu_o$
- unit power: $R_o^2 B_o^2 C_{Ao}/\mu_o$
- unit power density: $B_o^2 C_{Ao}/(\mu_o R_o)$
- unit impedance: $\mu_o C_{Ao}$
- unit voltage: $R_o B_o C_{Ao}$
- etc.

Note that all quantities defining the normalizations of LION are taken on magnetic axis. In the equilibrium code EQLAUS, however, the normalizations are defined on the geometrical centre of the discharge (see Section 2.3). There is generally a slight shift between those two positions. Note also that the unit magnetic field, B_o, is the value of the actual magnetic field, i.e. including paramagnetic effects, but not the equivalent vacuum field.

When comparing with experiment, it is better to take both the normalized and the experimental quantities on the Low Field Side extremity of the plasma surface. For example, if $\tilde{r}_{LFS}$ is the normalized position of this point and r_{LFS} the experimental value, then the normalization length, R_o (which is the input variable RMAJOR in

the LION code), must be

$$R_o = \frac{r_{LFS}}{\tilde{r}_{LFS}}$$

For the magnetic field, if $\tilde{T}(\psi_s)$ is the normalized toroidal flux function at plasma surface, the normalized toroidal component of the magnetic field at the low field side extremity of the plasma is

$$\tilde{B}_{ot,LFS} = \tilde{T}(\psi_s)/\tilde{r}_{LFS} \ ;$$

if $B_{ot,LFS}$ is the experimental value of the toroidal component of the magnetic field at the same point, then the unit magnetic field of LION, B_o (which is the input variable BNOT in the LION code) must be:

$$B_o = \frac{B_{ot,LFS}}{(\tilde{T}(\psi_s)/\tilde{r}_{LFS})}$$

3. Conclusions

We have developed, constructed, thoroughly tested and installed at JET a global wave code for the study of Alfvén wave and ICRF heating in exact toroidal geometry. The theory and the numerical implementation have been described in detail in Ref. 4. For the specialist reader an even more detailed description of the theory, the code and the physical results, is available in the form of a PhD thesis [20] written in French.

The code, named LION, has proven its ability to treat various scenarios (mode conversion, minority). We have shown that global effects can be important also in large machines like JET. The importance of toroidal effects has been clearly demonstrated. In the context of Alfvén wave heating it resulted in a totally successful comparison with the TCA experiment [7]. In the ICRF a detailed comparison has not been made yet. However, so far there is no contradiction between experimental (JET) and numerical (LION) results.

It is of fundamental importance that the LION code, which uses a finite element method, has been numerically tested and that the accuracy of the results can be measured [4]. It gives us confidence that the predictions of the LION code are physically relevant.

The performance of the LION code (vectorization in the most critical parts, optimization of input/output, maximum mesh size on CRAY1 of 40000 cells) makes it a powerful and reliable tool for the study of rf wave heating.

Acknowledgements

The authors gratefully acknowledge O. Sauter for his precious help when installing the LION code at JET. This work was partly supported by the Fonds National Suisse pour la Recherche Scientifique.

References

[1] K. Itoh et al., Nucl. Fus. 24, No 1 (1984) 13.

[2] E.F. Jaeger et al., Comput. Phys. Commun. 40, No 1 (1986) 33.

[3] P.L. Colestock, Proc. of the Course and Workshop on Applications of RF Waves to Tokamak Plasmas, September 1985, Varenna, Italy, Vol. I, p. 60.

[4] L. Villard et al., Comput. Phys. Reports 4 (1986) 95.

[5] T. Hellsten and E. Tennfors, Physica Scripta 30 (1984) 30.

[6] K. Appert et al., Plasma Phys. and Contr. Fus. 28, No 1A (1986) 133.

[7] K. Appert et al., Phys. Rev. Lett. 54, No 15 (1984) 1671.

[8] K. Appert et al., Comput. Phys. Commun. 40 (1986) 73.

[9] K.G. Budden, Radio Waves in the Ionosphere (Cambridge University Press, 1961).

[10] V.L. Ginzburg, Propagation of Electromagnetic Waves in Plasma (Gordon and Breach, 1961).

[11] T.H. Stix, The Theory of Plasma Waves (McGraw-Hill, New York, 1962).

[12] F.W. Perkins, IEEE Trans. Plasma Science PS-12 No 2 (1984) 53.

[13] N.F. Cramer and I.J. Donnelly, Plasma Phys. Contr. Fus. 26 (1984) 1285.

[14] A. Fruchtman and H. Weitzner, Phys. Fluids 29 (1986) 1620.

[15] K. Appert, B. Balet, R. Gruber, F. Troyon, T. Tsunematsu and J. Vaclavik, Nucl. Fus. 22 (1982) 903.

[16] M. Brambilla, Comput. Phys. Reports 4 (1986) 71.

[17] V.P. Bhatnagar, R. Koch, P. Geilfus, R. Kirkpatrick and R.R. Weynants, Nucl. Fus. 24 (1984) 955.

[18] D.J. Gambier and D.G. Swanson, Phys. Fluids 28 (1985) 145.

[19] T. Hellsten and L. Villard, Proc. of the 1987 European Conf. on Plasma Phys. and Contr. Fusion, Madrid, Spain, 1987.

[20] L. Villard, Propagation et Absorption d'Ondes aux Fréquences d'Alfvén et Cyclotroniques Ioniques dans les Plasmas Toriques, Thèse No 673 (1987), Ecole Polytechnique Fédérale de Lausanne, Switzerland.

Figure Captions

Fig. 1: Contour plot of the left-hand polarization $|E_+|$ for a D-(^{3}He) mode conversion scenario in JET: $n(^3He)/n_D$ = 7.36%, f = 33 MHz, LFS antenna, n = -15, B_o = 3.4 T.

Fig. 2: Coupling spectrum as a function of the toroidal wavenumber n for the same parameters as Fig. 1
(a) for I_{plasma} = 9.5 MA, (b) for I_{plasma} = 4.4 MA.

Fig. 3: Coupling spectrum as a function of the frequency for a single toroidal mode number (n = 15) and for the same parameters as Fig. 1 for I_{plasma} = 9.5 MA.

Fig. 4: Coupling spectrum as a function of the frequency for a D-(H) minority case in JET.
n_H/n_e = 5%, LFS antenna, n = -15, B_o = 3.4 T.

Fig. 5: Coupling spectrum as a function of the frequency for a D-(H) fast wave heating case in JET.
n_H/n_e = 30%, LFS antenna, n = -15, B_o = 3.4 T.

Fig. 6: Contour plot of the power absorption density for f = 42.85 MHz, corresponding to a main peak of Fig. 5.

Fig. 7: Contour plot of the power absorption density for f = 42.24 MHz, corresponding to a "satellite" peak of Fig. 5.

Fig. 8: Coupling spectrum as a function of the frequency for Top-Bottom (T/B) and HFS antennae. The other parameters and the units of power (vertical axis) are the same as in Fig. 5.

Fig. 9: (a) Poynting flux P_S (eq. 9, arbitrary units) and dP_S/ds versus the radial coordinate s for a D-(H) minority case in JET; $n_{Do} = 4 \cdot 10^{19} m^{-3}$, $n_H/n_D = 4\%$, $B_o = 2T$, f = 30 MHz, warm plasma model with $T_{Do} = T_{Ho} = 5$ keV, n = 25. (b) Power density profile averaged on magnetic surfaces P_V (eq. 10, in W/m^3 per Watt of total power) for the case of Fig. 9(a).

Fig. 10: Contour plot of the wavefield polarization $|E_+|$ for the case of Fig. 9. The dashed line represents $\omega = \omega_{cH}$.

Fig. 11: Same as Fig. 10 but cold plasma model. The dashed line represents $\omega = \omega_{cH}$.

Fig. 12: Real part of E_N for the case of Fig. 9.

Fig. 13: Real part of E for the case of Fig. 9.

Fig. 14: Contour plot of the power absorption density for the case of Fig. 9.

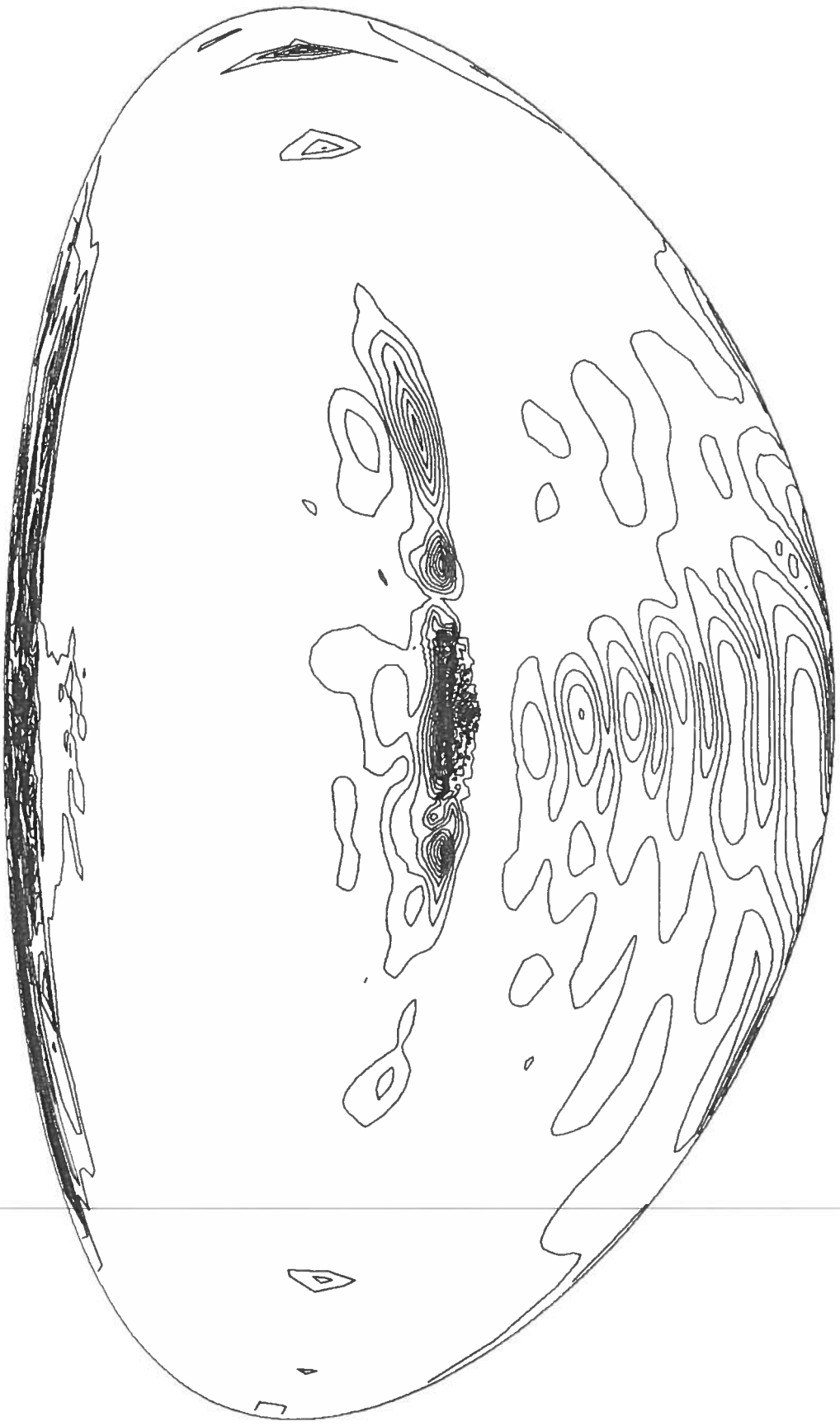

FIG. 1

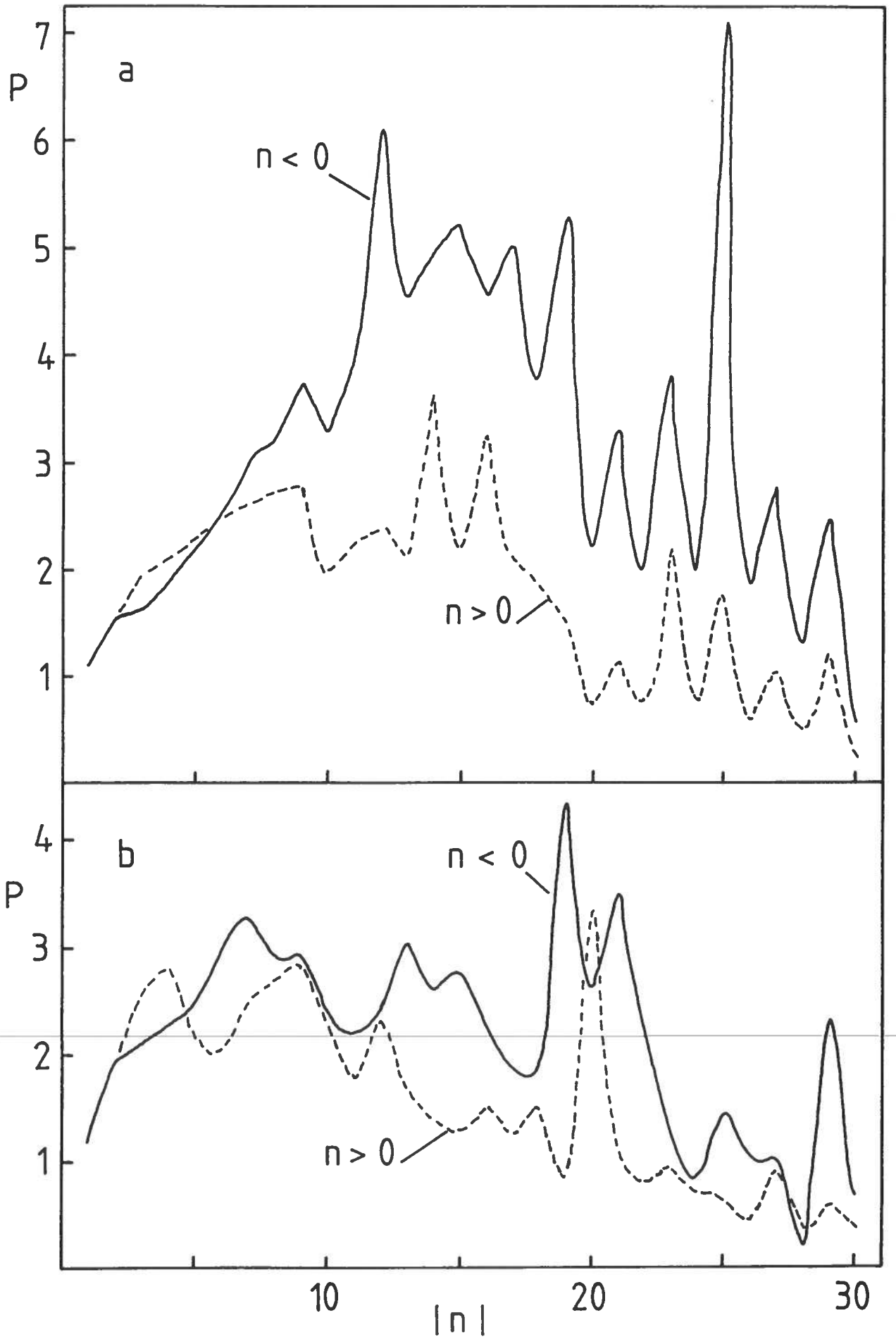

FIG. 2

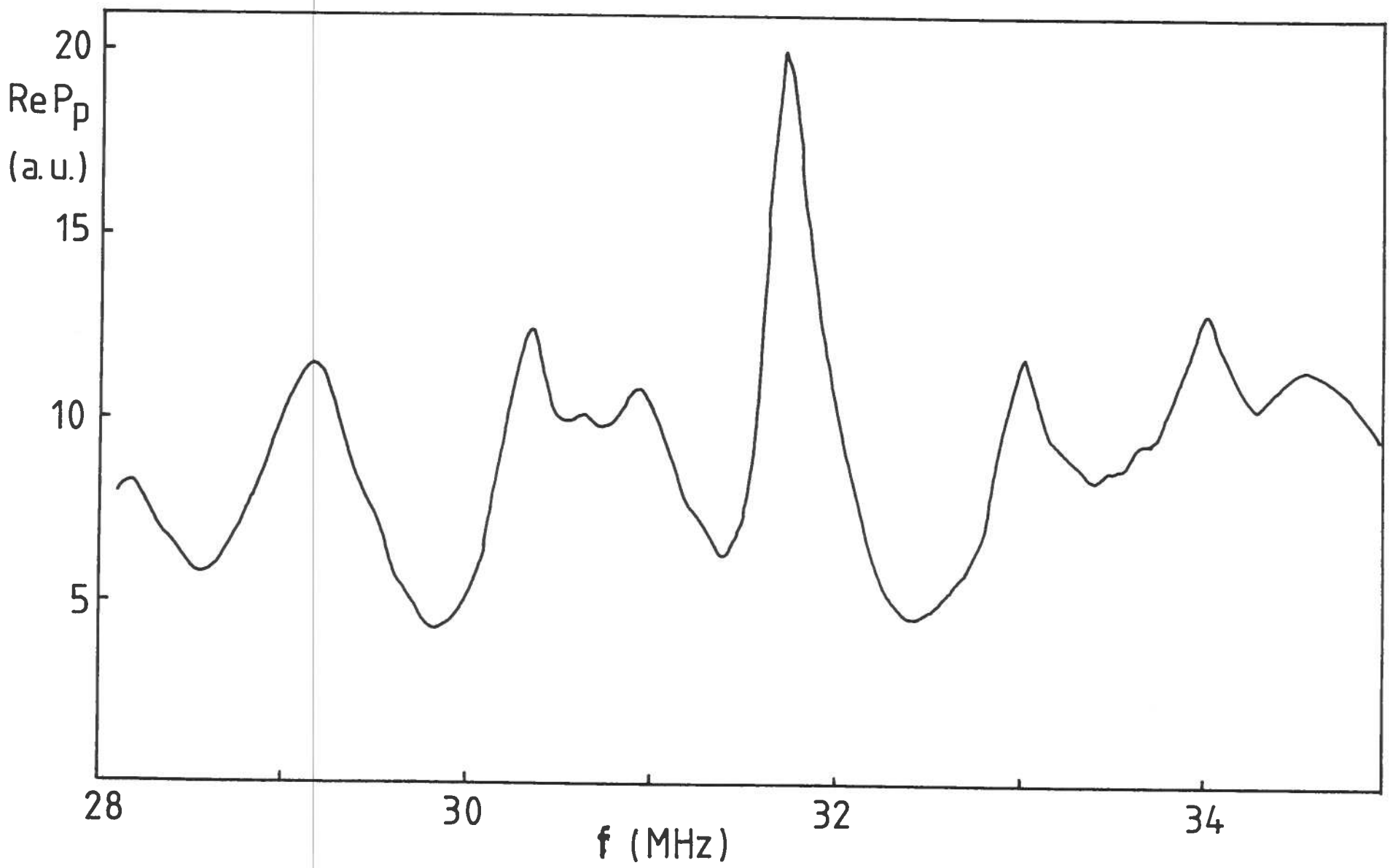

FIG. 3

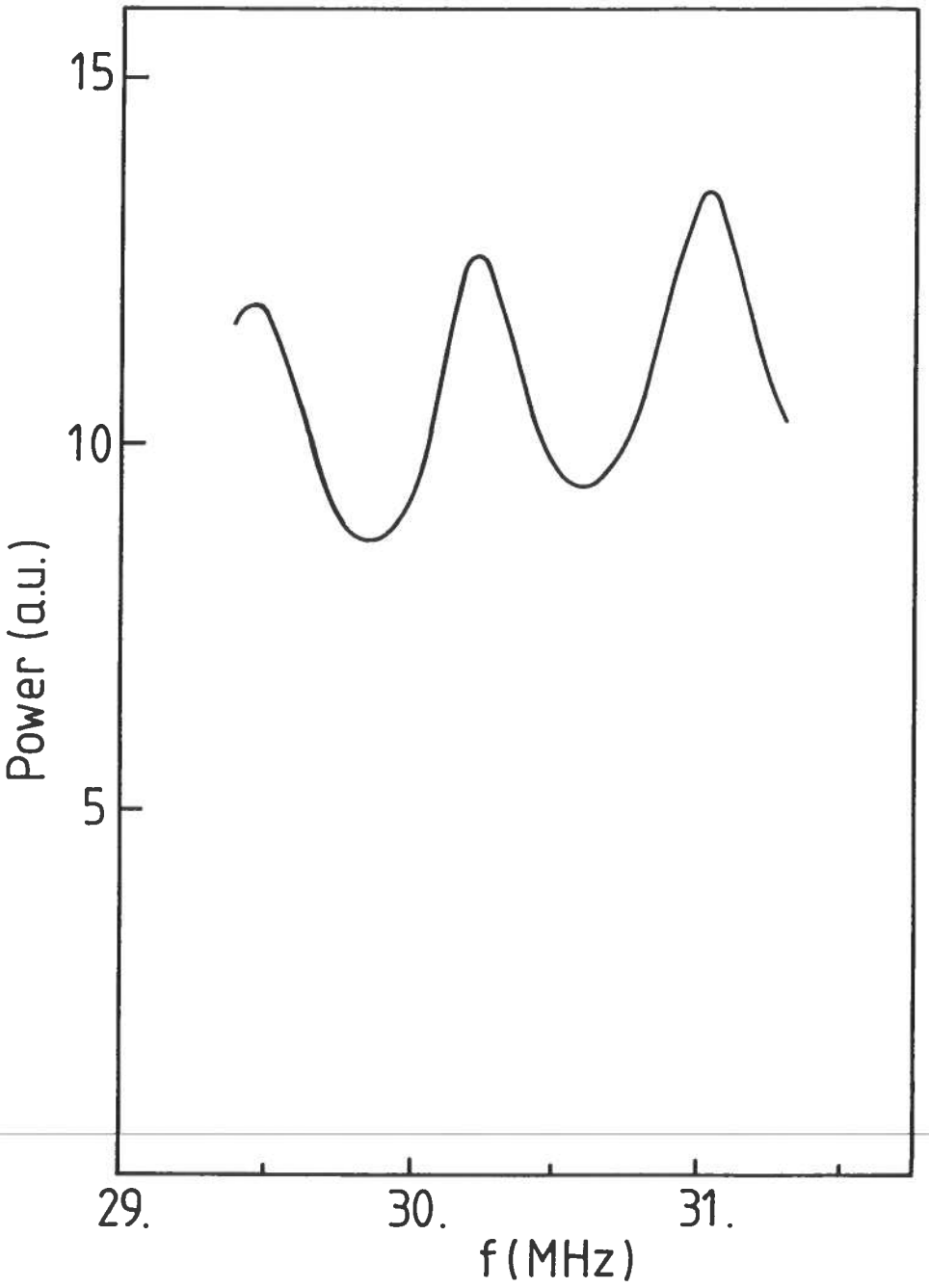

FIG. 4

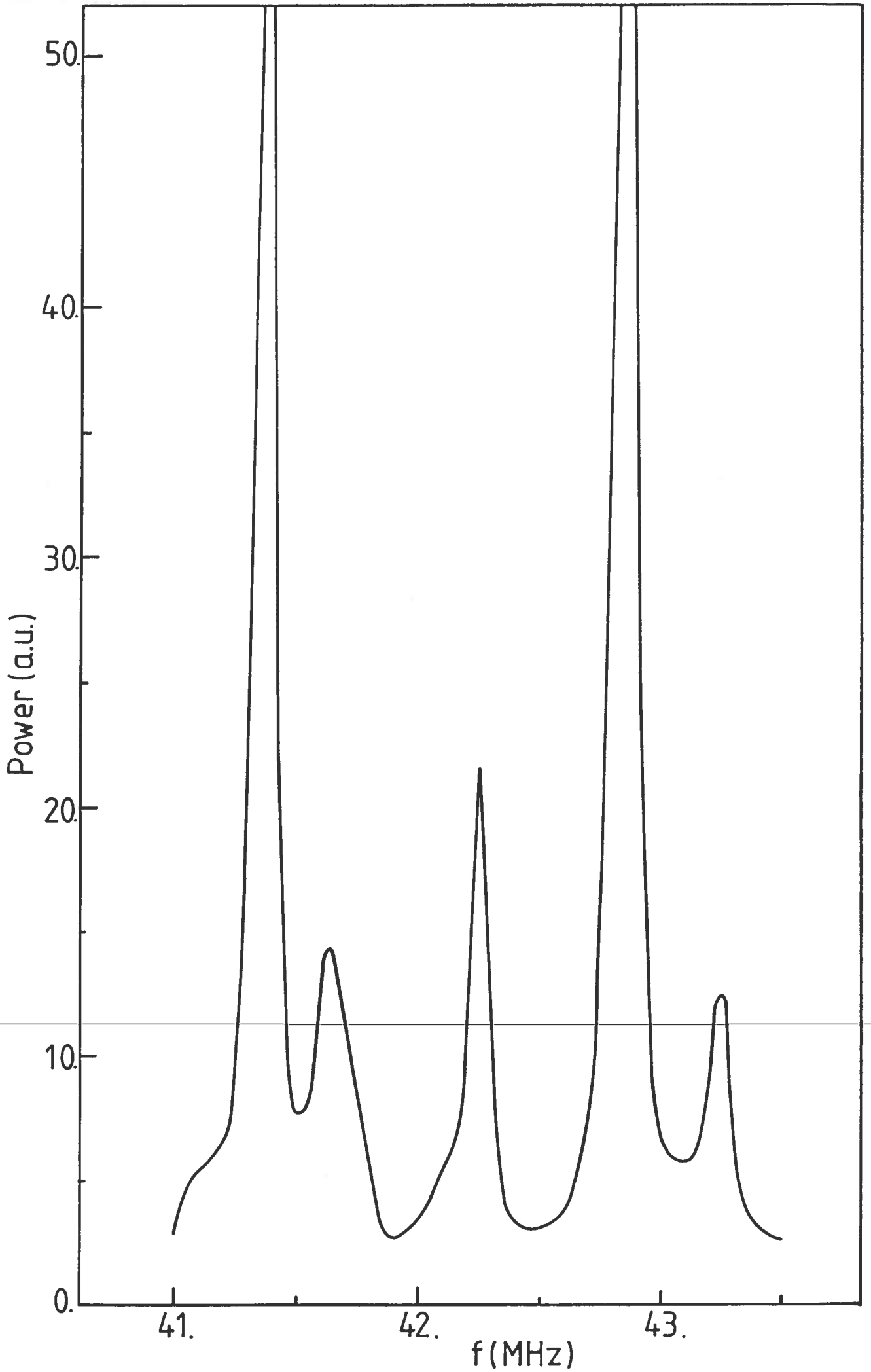

FIG. 5

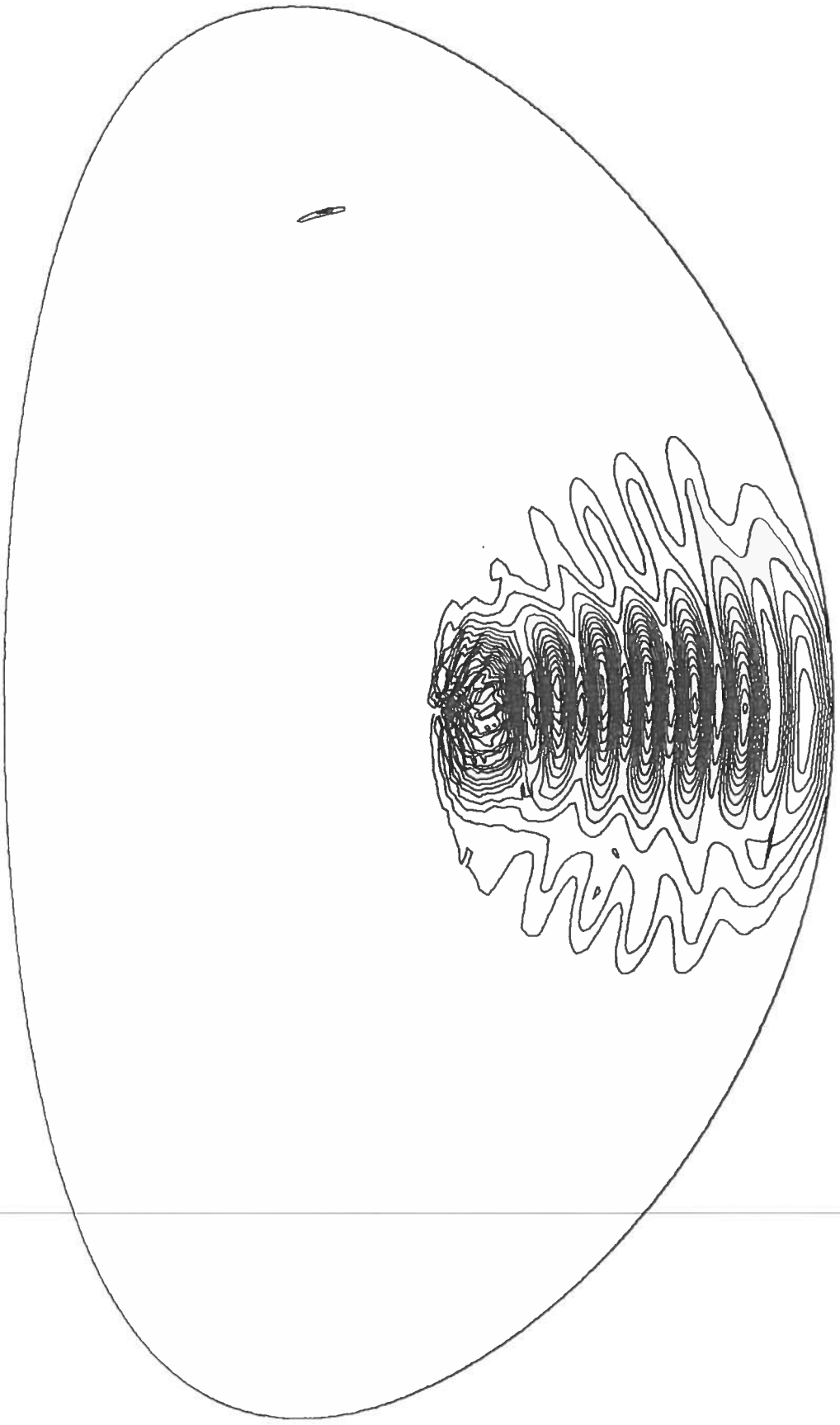

FIG. 6

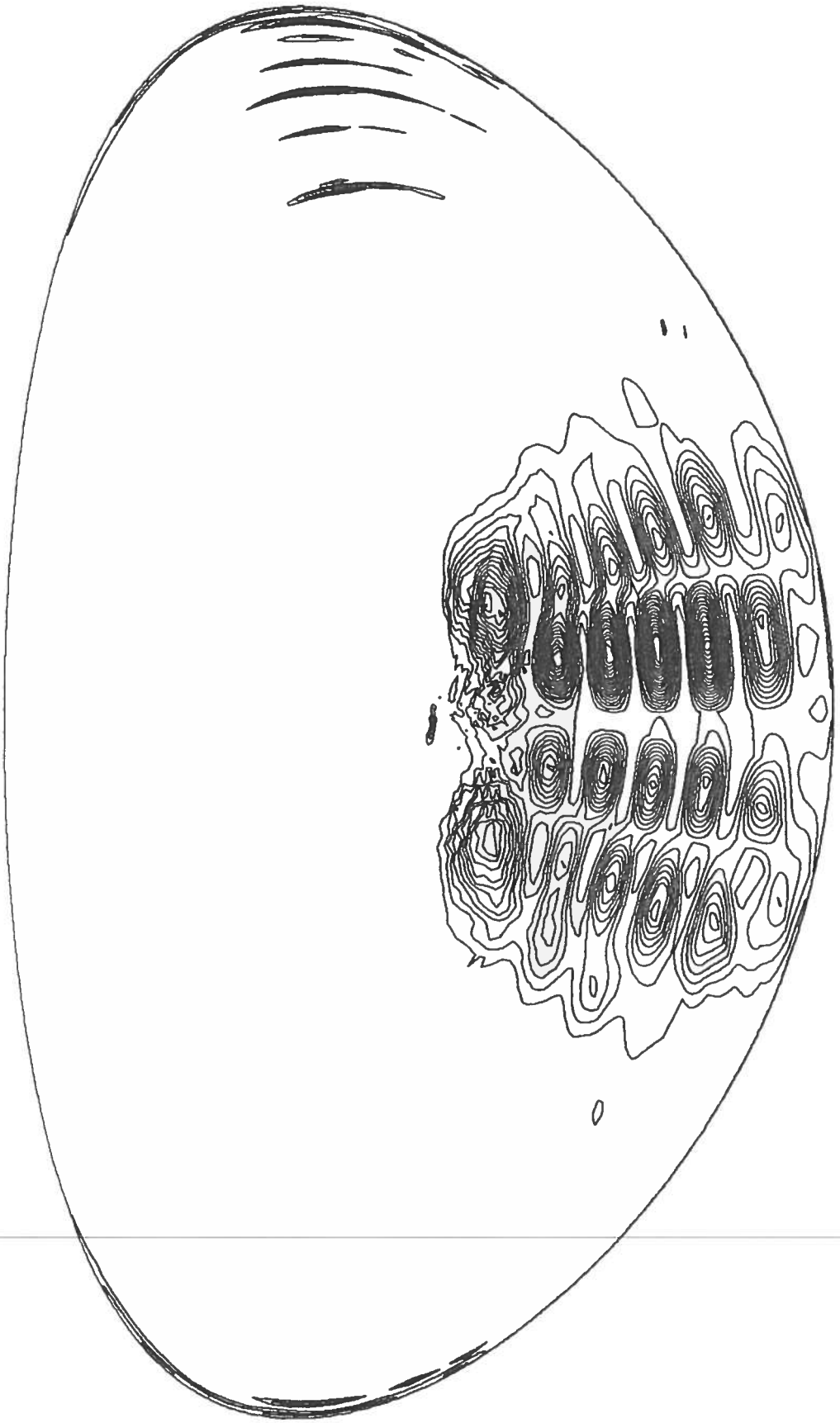

FIG. 7

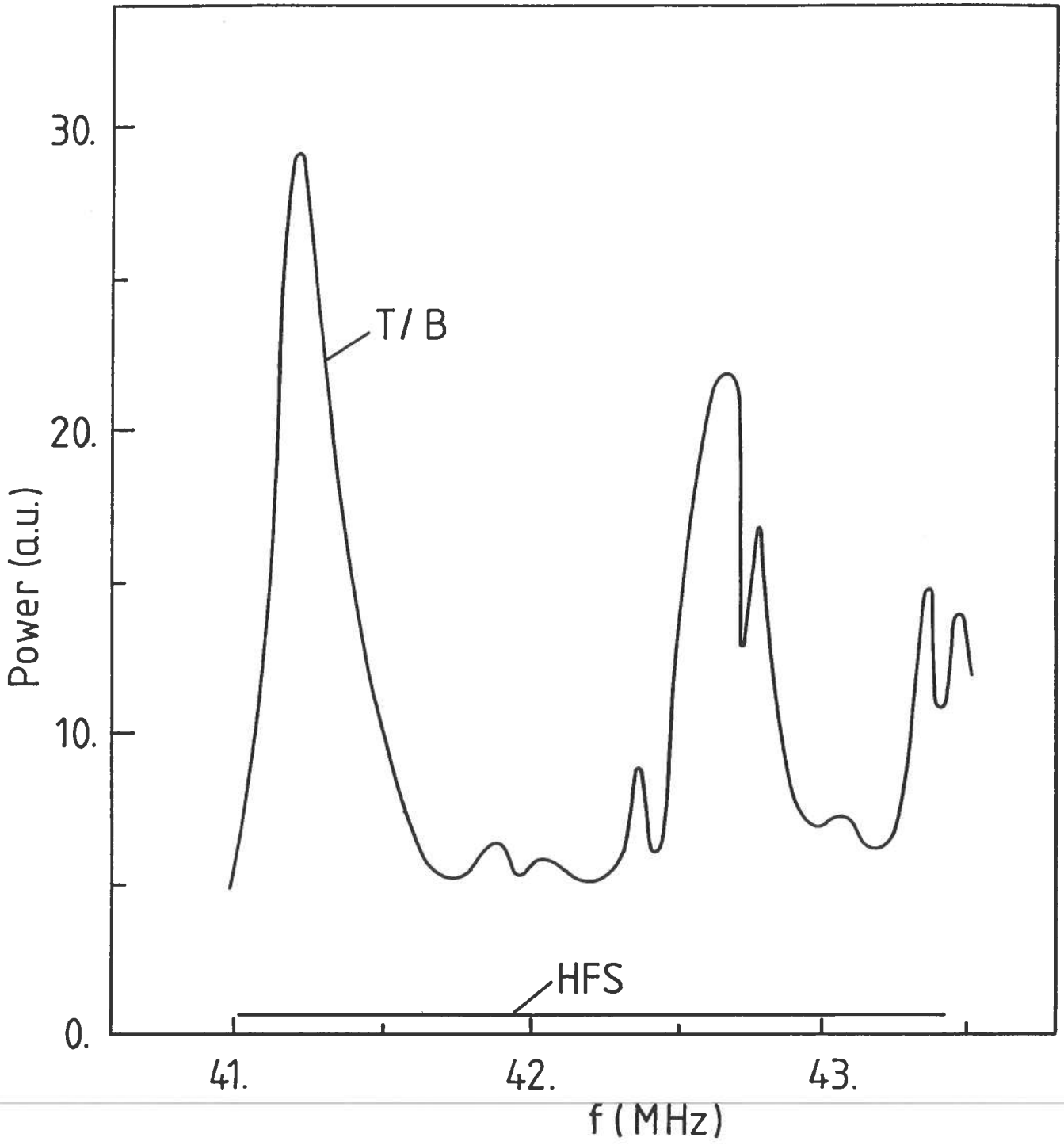

FIG. 8

FIG. 9A

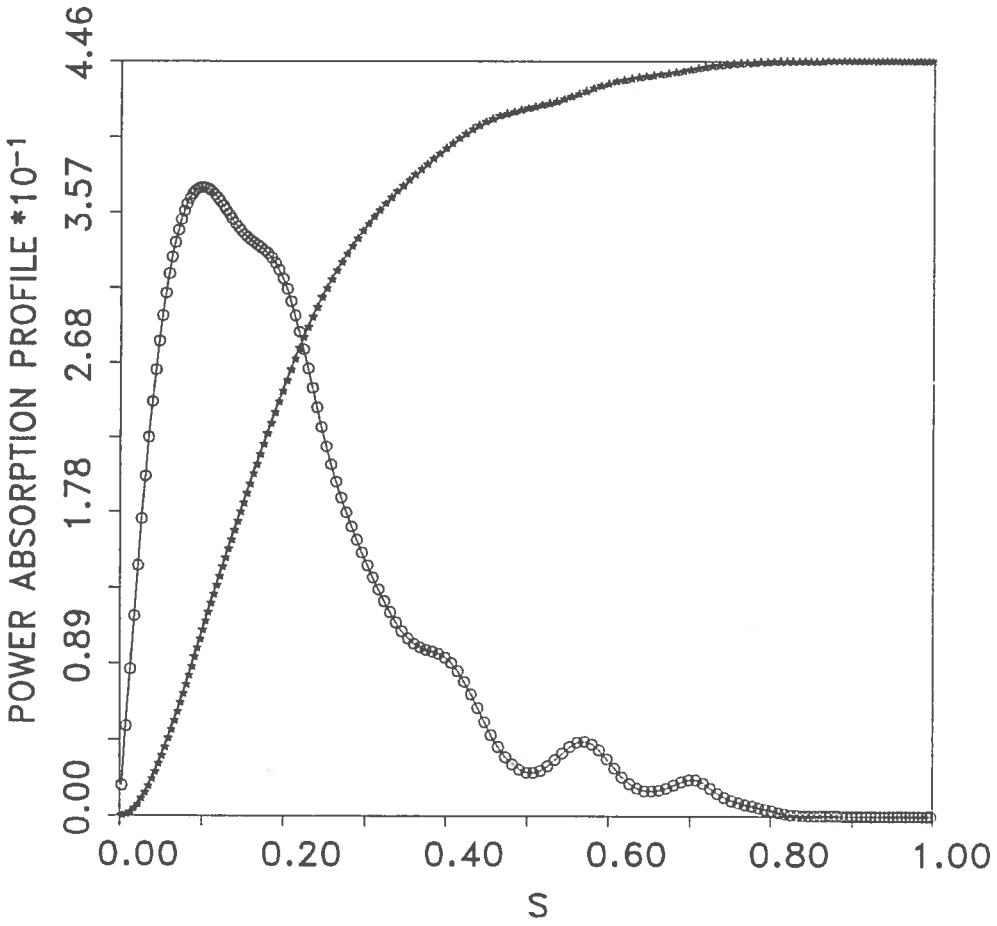
POWER ABSORPTION PROFILE *10⁻¹
0.00
0.89
1.78
2.68
3.57
4.46
0.00
0.20
0.40
0.60
0.80
1.00
S

FIG. 9B

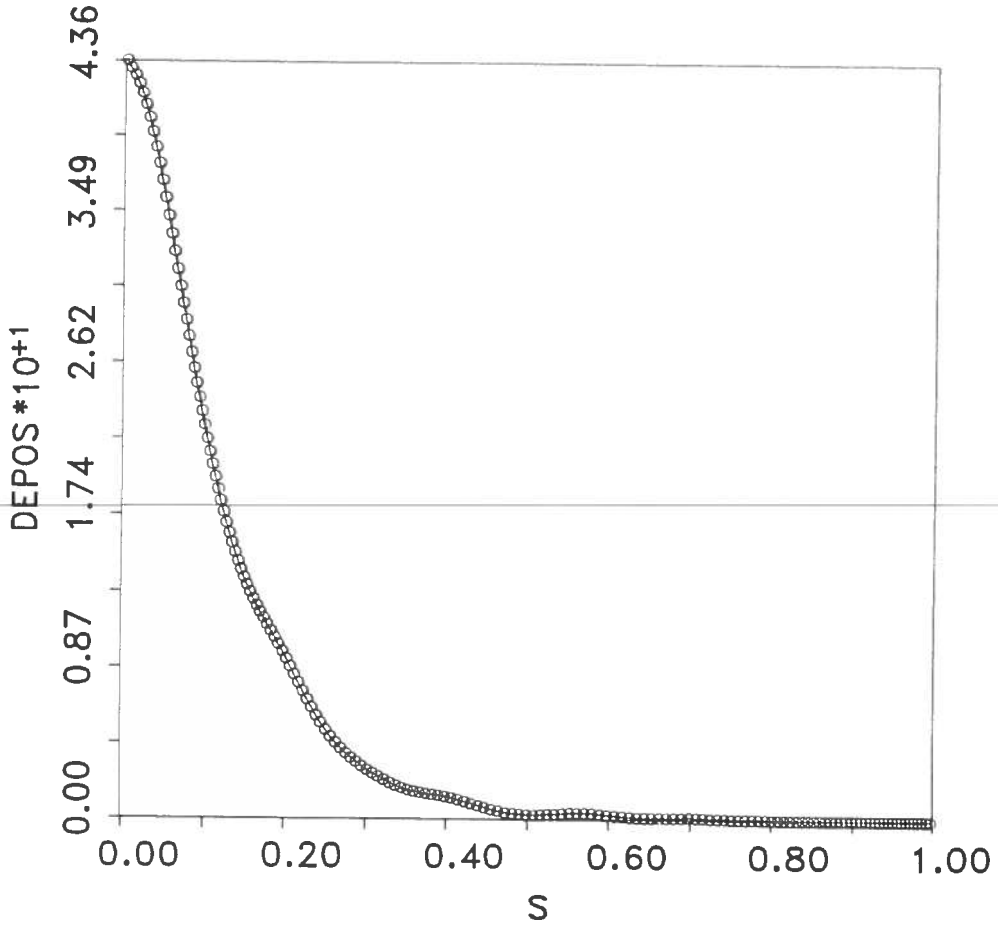
DEPOS *10⁺¹
0.00
0.87
1.74
2.62
3.49
4.36
0.00
0.20
0.40
0.60
0.80
1.00
S

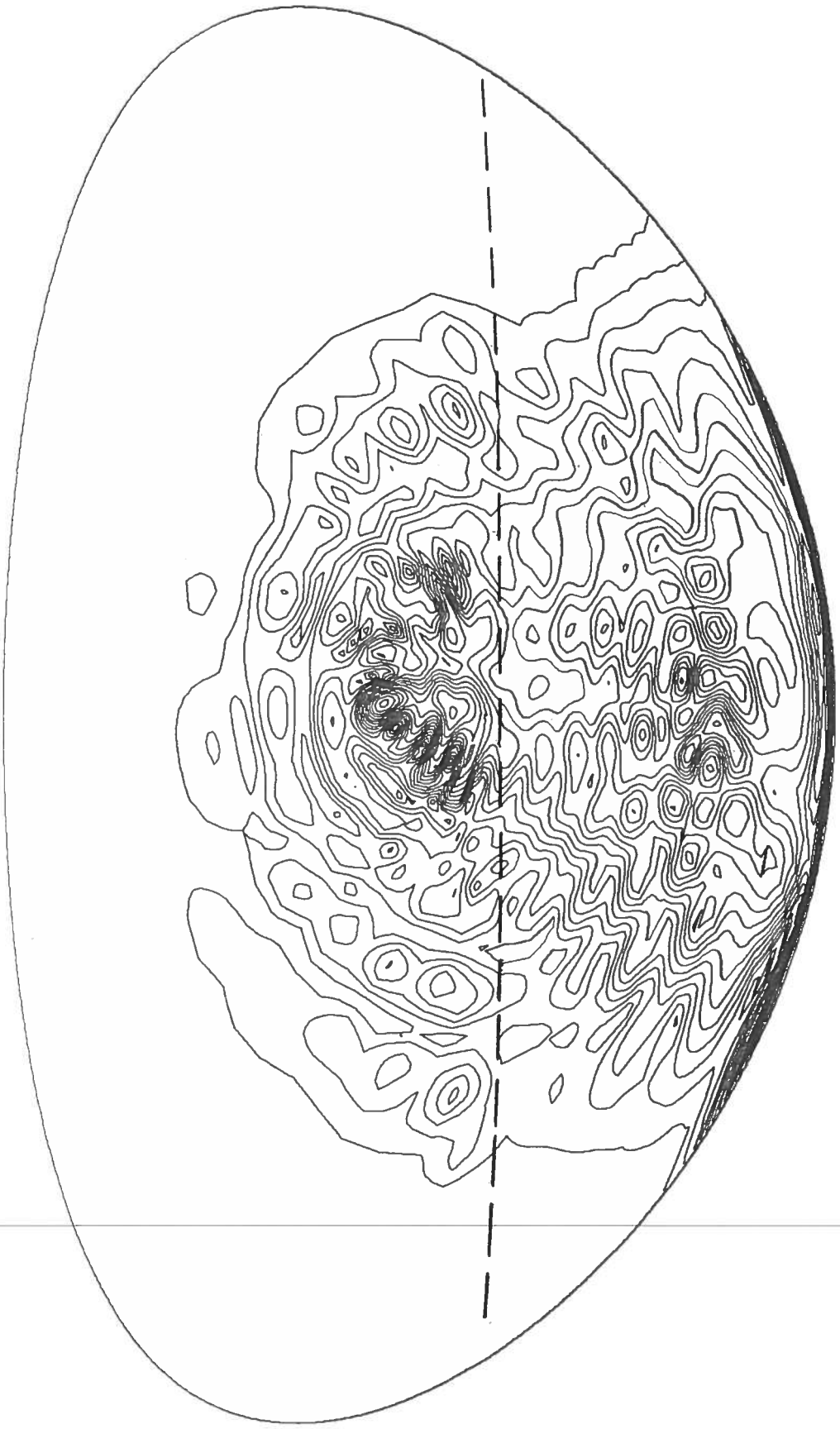

FIG. 10

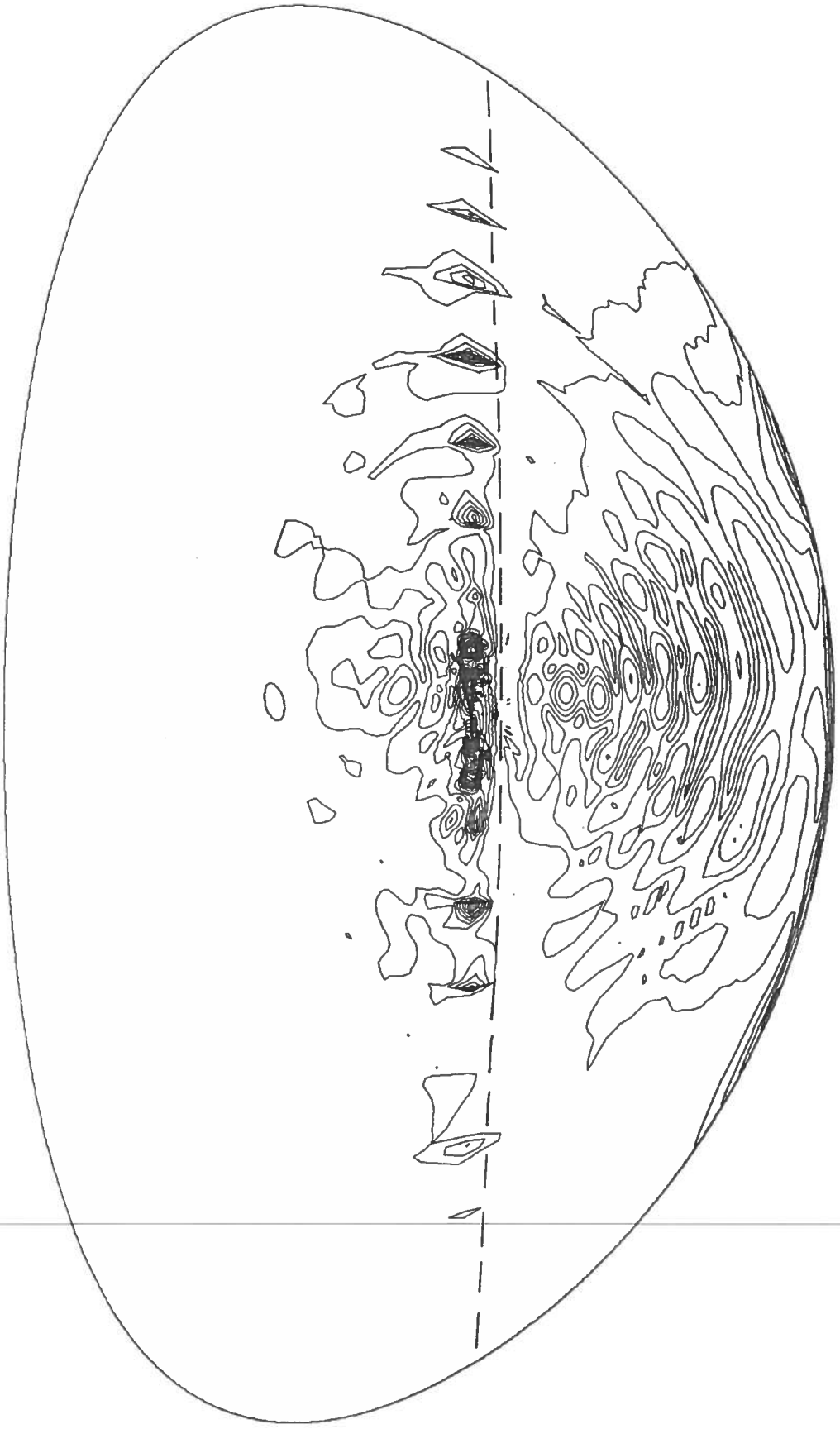

FIG. 11

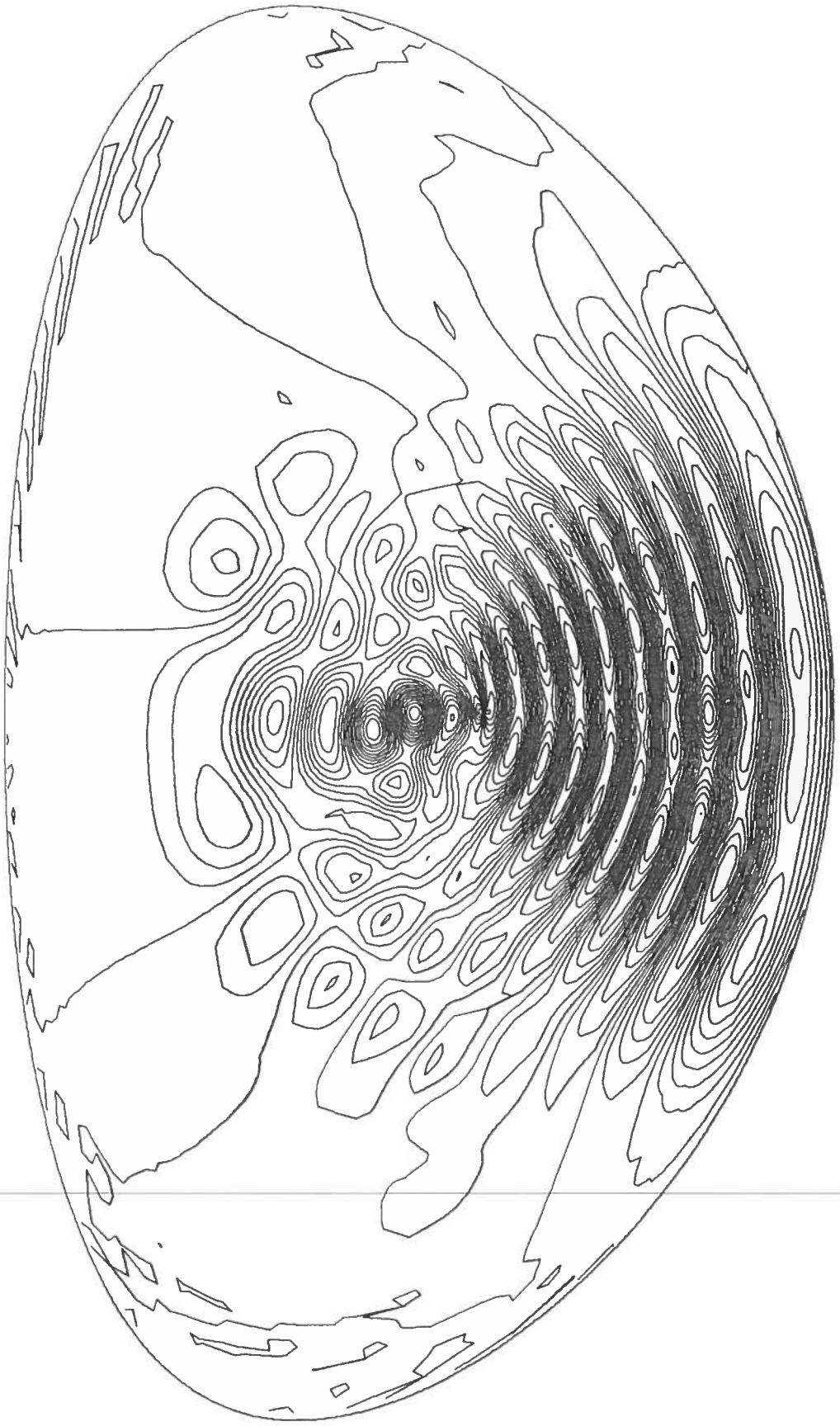

FIG. 12

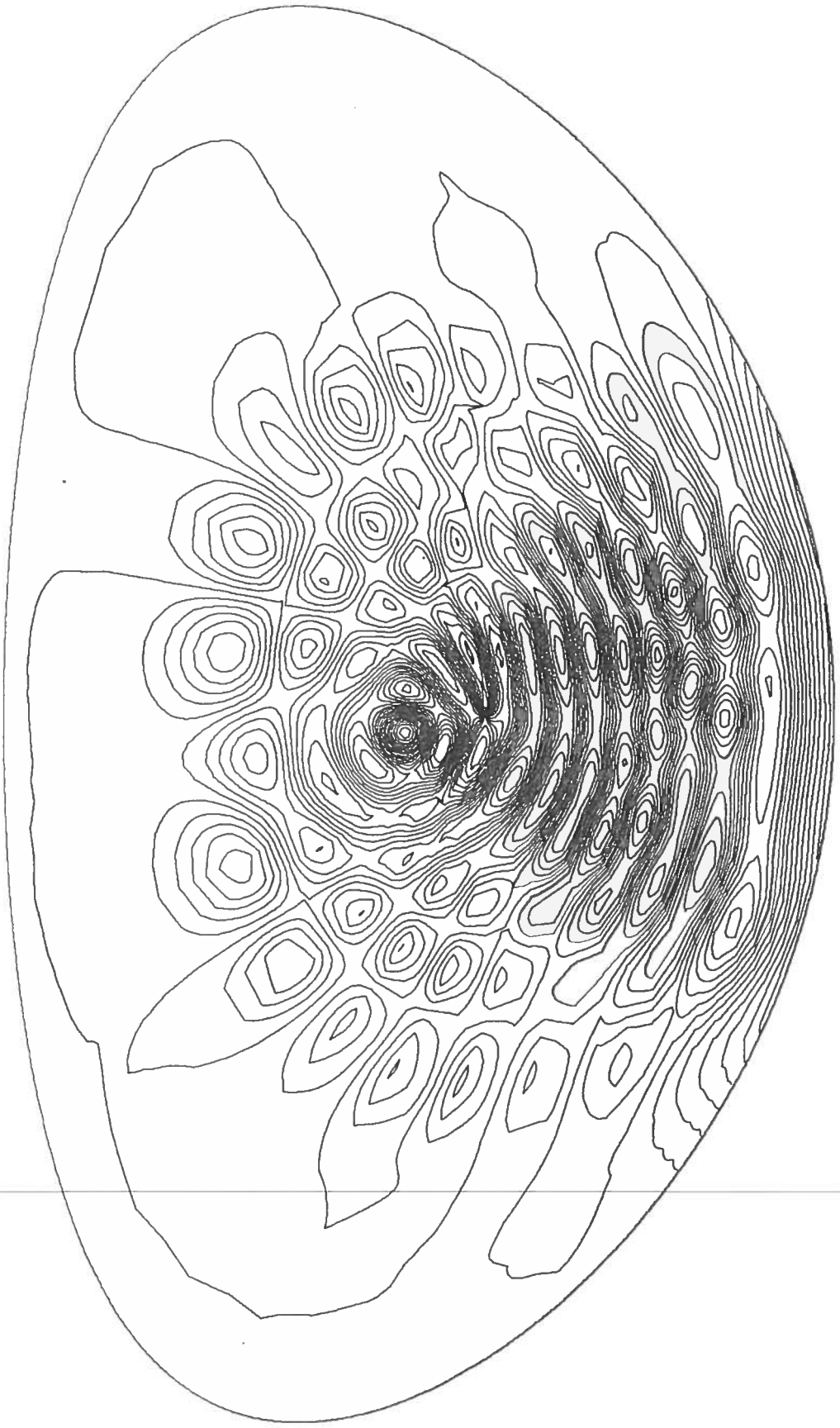

FIG. 13

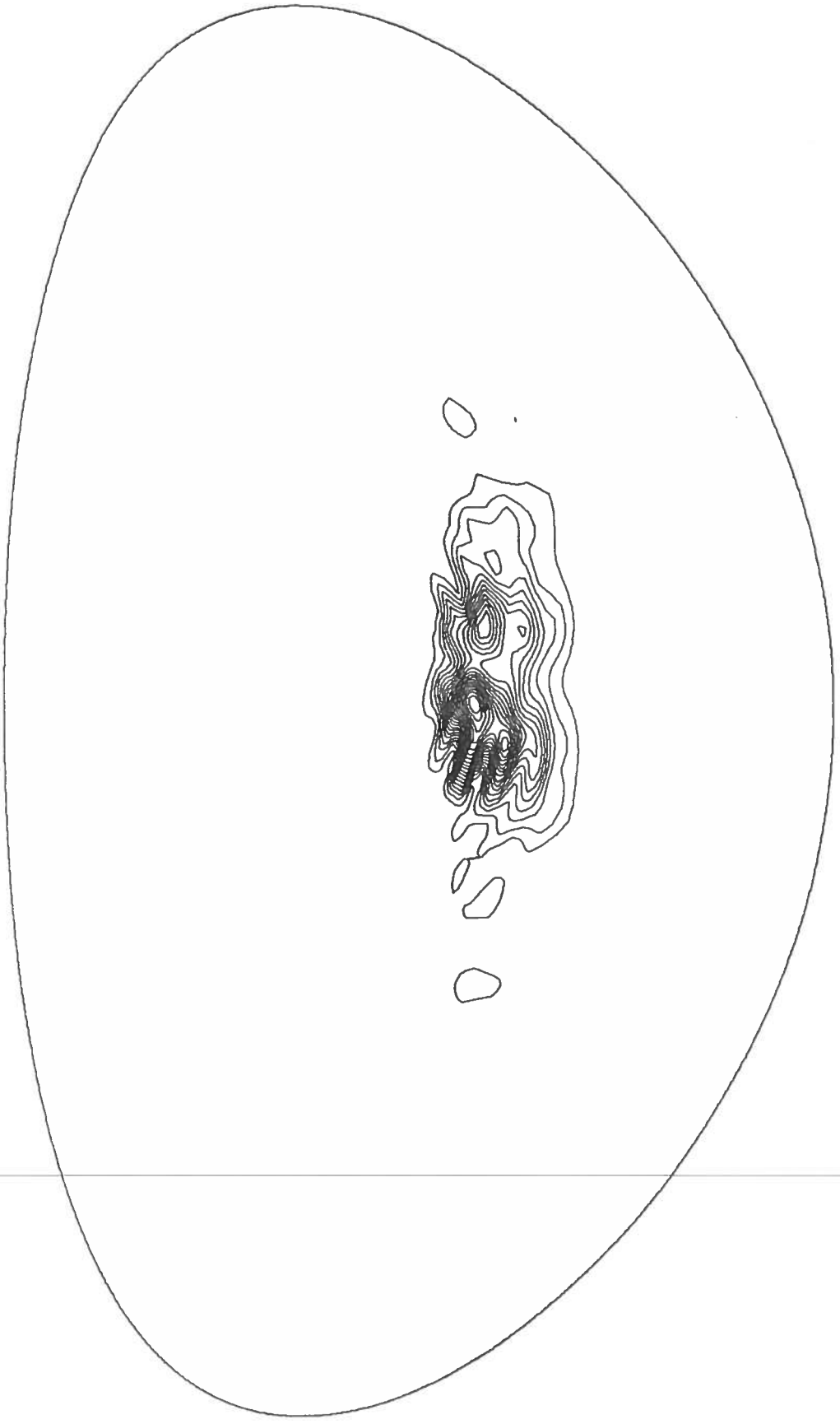

FIG. 14

APPENDIX I :

Detailed Description of the Method and Numerical Analysis of the Results

Computer Physics Reports 4 (1986) 95–135
North-Holland, Amsterdam

GLOBAL WAVES IN COLD PLASMAS

L. VILLARD, K. APPERT, R. GRUBER and J. VACLAVIK

Centre de Recherches en Physique des Plasmas, Association EURATOM – Confédération Suisse, École Polytechnique Fédérale de Lausanne, 21, Av. des Bains, CH-1007 Lausanne, Switzerland

This paper presents numerical methods developed for the calculation of global wave solutions in cold plasmas, in connection with rf heating in the Alfvén and Ion Cyclotron Range of Frequency. Both one-dimensional and two-dimensional geometries are treated, with special emphasis on the toroidal geometry. A scheme based on a variational formulation and the use of finite hybrid elements is presented in detail. The numerical properties of the computational model are carefully examined. It is shown that an approximate solution with good convergence properties in an exact geometry can be obtained.

0167-7977/86/$14.70

Contents

1. Introduction

The study of waves in cold plasmas is one of the oldest subjects of plasma physics [1–3]. In the last few years much effort has been made in this domain [4–10] in great part due to the numerous experimental achievements with using rf waves to heat the plasma [11,12]. Though the properties of such waves in homogeneous plasmas have been well known since a long time, many difficulties arise when the non-uniformity, the finite size and the actual geometry of the plasma in present day experiments, such as tokamaks, are taken into account in the theoretical models.

The first way to tackle the problem has been to treat the differential equations in the WKB approximation, which in multi-dimensional geometries led to the ray-tracing techniques. This approach has given many successful results [13–15]. Unfortunately, it suffers from several limitations. Firstly, the WKB approximation may break down, for example around the resonances. Secondly, in the Alfvén and Ion Cyclotron Range of Frequency (ICRF), in the actual experimental devices the wavelength is of the same order or larger than the size of the plasma, making a geometrical optics approach inappropriate. Thirdly, in ray tracing one has to assume single-pass absorption, making the study of eigenmodes impossible.

These reasons, together with the complexity of the analytical methods [16], motivate a different approach to the problem, namely the *global determination of the wave field in inhomogeneous, non-uniformly magnetized, finite-size plasmas using numerical techniques to solve appropriate differential equations.* By global solution we mean that:

- the problem is solved in *one* well-defined geometry, with no matching between different regions having different geometries;
- the solution obtained is the sum of *all* incident, reflected, transmitted and evanescent waves;
- the differential equations are solved in the whole domain: plasma and vacuum including antenna and shell.

As stated above, it is specially in the Alfvén and ICRF domains that a global solution is needed. We shall therefore limit ourselves to this frequency range.

In this domain, three physical phenomena can be exploited for rf heating:

- the existence of global eigenmodes of the fast magnetosonic wave and of the Alfén wave [17];
- the perpendicular resonances, either Alfvén or ion–ion hybrid of a multi-ion species plasma (mode conversion regimes);
- the cyclotron damping, assisted by introducing a minority ion species (minority regime).

Our global approach will be able to treat the eigenmodes and the perpendicular resonances in cold plasmas, as well as their simultaneous occurrence.

The numerical methods used to determine the global solution are well-known textbook methods [18,19]. Nevertheless, their application to the study of rf waves in plasmas is rather recent. It is therefore necessary to discuss them in detail, in particular to show clearly their mathematical foundation and to determine where their domain of validity is, in order to develop them to a high degree of credibility. In this paper we shall present the implications of the specific physical and mathematical properties of the problem on the choice of the numerical methods.

The paper is structured as follows. In section 2 we make a few remarks about the one-dimensional problem. The aim of this section is to illustrate some of the basic methods for calculating a global solution. First, we discuss the pertinence of using a cold plasma model for rf heating. We then mention shooting and finite element methods. The treatment of vacuum, including antenna

and conducting wall, is also presented. In section 3 we describe the two-dimensional problem. Special care has been taken of the treatment of the toroidal geometry. In particular, we present the recent development of the LION code. LION is based on a variational formulation and finite hybrid elements. The numerical scheme is very carefully examined. By doing convergence studies the accuracy can be measured; comparison with analytical work [20], where possible, as well as with experiment [21] is made; other physical tests, for example of the power balance, are presented. Section 4 discusses the limitations of global wave codes and the possible future improvements of the numerical techniques. We conclude in section 5.

2. Global wave solution in one-dimensional geometry

2.1. Cold plasma

The first question which arises is the pertinence of cold plasma model for studying rf heating. In the Alfvén and ion cyclotron range of frequencies, two phenomena are pure warm plasma effects: the existence of kinetic Alfvén and ion Bernstein waves, and the cyclotron damping. It is therefore necessary to keep in mind that neither 2nd harmonic heating, where the interaction with the ion Bernstein wave is crucial, nor fundamental minority heating, where ion cyclotron absorption takes place, can ever be described in the context of cold plasma. It then remains the question of the influence of finite temperature on mode conversion scenarios. It has been shown that the cold plasma model is in very good agreement with the warm plasma model, at least in 1-D geometry. When the temperature of the plasma tends to zero, the ion Bernstein wave reduces to the ion–ion perpendicular resonance. But the total power absorbed is exactly the same. In other words, the antenna ignores that the plasma is warm. For more details, see ref. [22].

2.2. Equations

2.2.1. Basic equations

We consider a cylindrical, non-uniform, current-carrying, multi-species plasma (fig. 1). All equilibrium quantities depending on r only, we can Fourier-decompose the fields in $\exp\{i(m\theta + kz)\}$. Let us define a local magnetic coordinate system $(\boldsymbol{e}_N, \boldsymbol{e}_\perp, \boldsymbol{e}_\parallel)$ by

$$\begin{aligned} \boldsymbol{e}_N &= \nabla r/|\nabla r|, \\ \boldsymbol{e}_\parallel &= \boldsymbol{B}_0/B_0, \\ \boldsymbol{e}_\perp &= \boldsymbol{e}_\parallel \times \boldsymbol{e}_N, \end{aligned} \tag{2.1}$$

and project Maxwell's equations on this system. Moreover, we make the approximation of zero electron mass, leading to $E_\parallel = 0$. The most elegant way to write the equations is to use $E_\perp$ and $B_\parallel$ as variables:

$$\begin{aligned} A\frac{1}{r}\frac{d}{dr}(rE_\perp) &= Gk_\perp E_\perp + (A - k_\perp^2)i\omega B_\parallel, \\ A\frac{d}{dr}(i\omega B_\parallel) &= (G^2 - A^2)E_\perp - Gk_\perp i\omega B_\parallel, \end{aligned} \tag{2.2}$$

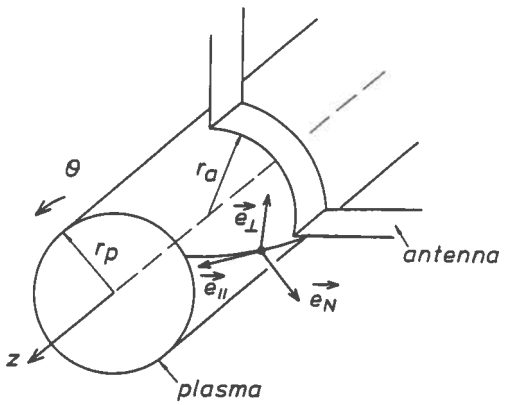

Fig. 1. Cylindrical configuration.

with

$$A = \epsilon_{NN} - k_\parallel^2, \qquad \epsilon_{NN} = \frac{\omega^2}{C^2} S = \frac{\omega^2}{C_A^2} \sum_i \frac{f_i}{1 - (\omega/\omega_{ci})^2},$$

$$G = -i\epsilon_{N\perp} - \frac{2k_\parallel B_{0\theta}}{rB_{0z}}, \quad \epsilon_{N\perp} = \frac{\omega^2}{C^2} iD = i\frac{\omega^2}{C_A^2} \sum_i \frac{f_i \omega/\omega_{ci}}{1 - (\omega/\omega_{ci})^2},$$

$$k_\parallel = \left(kB_{0z} + \frac{m}{r} B_{0\theta}\right)/B_0, \tag{2.3}$$

$$k_\perp = \left(\frac{m}{r} B_{0z} - kB_{0\theta}\right)/B_0,$$

$$C_A^2 = B_0^2/\mu_0 \rho_0,$$

f_i = mass fraction of the ith ion species $= n_i m_i/\rho_0$ (The summations are over all the ion species.).

2.2.2. Singularities

Except for $r = 0$, the only possible singularities of the equations are given by $A = 0$. One can easily show that the behaviour of the singular solution around the points $r = r_{res}$, defined by $A(r_{res}) = 0$, is

$$\begin{aligned} E_\perp &\sim \ln|r - r_{res}|, \\ B_\parallel &\sim \ln|r - r_{res}|, \\ B_N &\sim \ln|r - r_{res}|, \\ E_N &\sim 1/|r - r_{res}|, \\ B_\perp &\sim 1/|r - r_{res}|. \end{aligned} \tag{2.4}$$

The presence of a continuous spectrum, defined by $A = 0$, and the type of behaviour of the different field components (2.4) will have a consequence on the choice of the numerical method.

A simple way to turn around the singularities is to introduce a small imaginary part ν in A:

$$A \to A + \mathrm{i}\nu, \tag{2.5}$$

with $\nu > 0$ to satisfy the causality. Then the system (2.2) is no longer singular.

Let us make two important remarks:

1) $\omega = \omega_{ci}$ is not a singularity of the equations, despite of the presence of the resonant denominators in ϵ_{NN} and $\epsilon_{N\perp}$. Actually, one can show that the circular component of the polarization of the wave field in the ion gyromagnetic direction, $E_+ = E_N + \mathrm{i}E_\perp$, satisfies

$$\lim_{\omega \to \omega_{ci}} |E_+| = 0. \tag{2.6}$$

2) It is crucial that the singular behaviour of $E_\perp$ and $B_\parallel$ is non-analytical (2.4): the power absorption at the singularity is given by

$$\mathrm{Re}\,[\![E_\perp^* B_\parallel]\!]_{r_{res}-0}^{r_{res}+0} \sim -\mathrm{i}(\mathrm{i}\pi + \mathcal{O}(\nu)) \tag{2.7}$$

This feature allows resonance absorption to occur; the apparent paradox is that we have non-vanishing absorption with damping going to zero. It is then crucial that the numerical techniques guarantee a good description of the singular behaviour.

2.2.3. Antenna and vacuum

We shall neglect the displacement current in all what follows. This is a good approximation for Alfvén wave heating where the vacuum wavelength is much larger than the dimensions of the system. For ICRF in large devices it might be questionable.

Our antenna model is a current sheet located at $r = r_a$ (fig. 1), with surface currents j_θ and j_z

$$\begin{aligned} j_\theta &= \tfrac{1}{2}\hat{j}_\theta \delta(r - r_a)\exp(\mathrm{i}(m\theta + kz - \omega t)) + \text{c.c.},\\ j_z &= \tfrac{1}{2}\hat{j}_z \delta(r - r_a)\exp(i(m\theta + kz - \omega t)) + \text{c.c.}. \end{aligned} \tag{2.8}$$

In the region between antenna and shell, feeder currents j_r and $j_\perp$ are introduced to satisfy $\mathrm{div}\, j = 0$.

The surface currents can be treated as a discontinuity of the wave magnetic field, while the feeder currents are volume currents which have to be included in the vacuum wave equations. These can be brought to the form

$$\frac{\mathrm{d}}{\mathrm{d}r}\begin{bmatrix} rB_N \\ B_\parallel \end{bmatrix} + \begin{bmatrix} 0 & \mathrm{i}\dfrac{(k_\perp^2 + k_\parallel^2)r}{k_\parallel} \\ -\mathrm{i}\dfrac{k_\parallel}{r} & \dfrac{2B_{0\theta}k_\perp}{rB_{0z}k_\parallel} \end{bmatrix}\begin{bmatrix} rB_N \\ B_\parallel \end{bmatrix} = \begin{bmatrix} \dfrac{k_\perp}{k_\parallel} r j_r \\ -\dfrac{2\mathrm{i}B_{0\theta}}{rB_{0z}k_\parallel} j_r - j_\perp \end{bmatrix}. \tag{2.9}$$

2.2.4. Regularity, boundary and matching conditions

1) On the axis, the equations have the usual singularity of the cylindrical geometry. But for physical reasons, the solution has to be regular. Writing $E_\perp$ and $B_\parallel$ as

$$E_\perp = r^{|m|-1}\hat{E},$$
$$B_\parallel = \frac{1}{i\omega} r^{|m|}\hat{B}, \tag{2.10}$$

and expanding around $r=0$: $\hat{E} = e_0 + e_1 r + \cdots$, $\hat{B} = b_0 + b_1 r + \cdots$, $A = a_0 + a_1 r + \cdots$, $G = g_0 + g_1 r + \cdots$, we use eq. (2.2) to obtain in lowest order in r

$$\begin{bmatrix} a_0|m| - mg_0 & m^2 \\ a_0^2 - g_0^2 & a_0|m| + mg_0 \end{bmatrix} \begin{bmatrix} e_0 \\ b_0 \end{bmatrix} = 0. \tag{2.11}$$

The regularity condition is then

$$\hat{E}(r=0) = \frac{m^2}{mg_0 - |m|a_0}\hat{B}(r=0). \tag{2.12}$$

2) At the plasma–vacuum interface, we require the fields be continuous. We only have to transform $E_\perp$ to B_N

$$B_N(r=r_p) = -\frac{k_\parallel}{\omega} E_\perp(r=r_p). \tag{2.13}$$

3) At the antenna, the surface currents (2.8) impose

$$[\![B_N]\!] = 0, \quad [\![B_\parallel]\!] = -\hat{j}_\theta + \frac{B_{0\parallel}}{B_{0z}}\hat{j}_z, \tag{2.14}$$

where the double bracket indicates a jump across the antenna from the inside to the outside.

4) On the shell, the infinite conductivity imposes

$$B_N(r=r_s) = 0. \tag{2.15}$$

The eqs. (2.2) and (2.9), with (2.12)–(2.15), determine a unique solution.

2.2.5. Power

The total complex power delivered by the antenna is

$$P_a = \tfrac{1}{2}\int_V \boldsymbol{J}\cdot\boldsymbol{E}^* \mathrm{d}V, \tag{2.16}$$

where V is the vacuum domain.

It can be compared to the total power transmitted through the plasma–vacuum interface

$$P_p = \tfrac{1}{2}\int_{\partial\Omega} E_\perp^* B_\parallel \mathrm{d}\sigma. \tag{2.17}$$

2.3. Shooting methods

The simplest numerical scheme is to solve (2.2), (2.9), (2.12)–(2.15) as an initial value problem with a Runge–Kutta algorithm. The principle is to determine the fundamentals of the system of equations and to use the matching conditions to fix the constants of integration. The presence of singularities forces us to introduce $\nu \neq 0$ in the equations (see 2.5) and to have an adjustable step in order to control the accuracy. We proceed as follows:

1) We start at $r = \delta \ll 1$ with a given initial value, using the regularity condition (2.12). We integrate the plasma equations (2.2) up to the plasma–vacuum interface $r = r_p$.
2) We use (2.13) to transform $E_\perp$ to B_N, and integrate the vacuum equations (2.9) with $j_r = j_\perp = 0$ up to the antenna $r = r_a$. We have then the solution at $r_a - 0$

$$C_1 \begin{bmatrix} B_N^{(A)} \\ B_\parallel^{(A)} \end{bmatrix}. \tag{2.18}$$

3) In the region between the antenna and shell we integrate once the homogeneous (H) equations, i.e. (2.9) with $j_N = j_\perp = 0$, and once the inhomogeneous ones (N) starting with the condition (2.15). We have the solution at $r_a + 0$

$$C_2 \begin{bmatrix} B_N^{(H)} \\ B_\parallel^{(H)} \end{bmatrix} + \begin{bmatrix} B^{(N)} \\ B_\parallel^{(N)} \end{bmatrix}. \tag{2.19}$$

4) The matching conditions at the antenna (2.14) introduced into (2.18) and (2.19) yield the integration constants

$$\begin{aligned} C_1 &= \frac{1}{B_N^{(A)}}\left(C_2 B_N^{(H)} + B_N^{(N)}\right), \\ C_2 &= \frac{1}{D}\left(-B_\parallel^{(N)} + \frac{B_\parallel^{(A)} B_N^{(N)}}{B_N^{(A)}} - \hat{j}_\theta + \frac{B_{0\theta}}{B_{0z}}\hat{j}_z\right), \\ D &= B_\parallel^{(H)} - \frac{B_\parallel^{(A)} B_N^{(H)}}{B_N^{(A)}}. \end{aligned} \tag{2.20}$$

5) We use (2.16) and (2.17) to calculate the total power.

The real antenna excitation structure can be Fourier-decomposed in $\exp\{\mathrm{i}(m\theta + kz - \omega t)\}$. The whole procedure 1) to 5) is repeated for each Fourier component. The total power is simply the sum of the powers of all components.

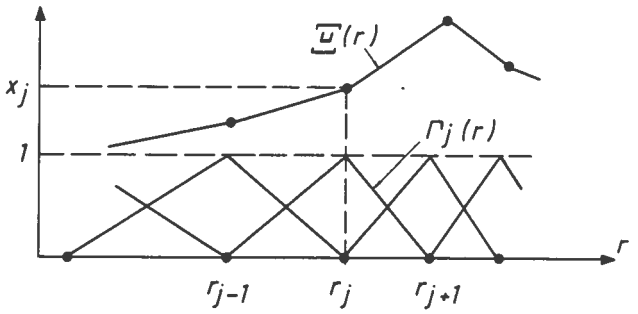

Fig. 2. Basis functions Γ_j for the regular finite elements of first order and representation $\Xi(r)$ of a function with these elements.

An example of application of such a method has been the calculation of antenna coupling for Alfvén wave heating in TCA [23]. Different configurations of antennae were used: variation of its excitation spectrum, tilt, positioning the feeders, etc., in order to optimize the coupling and the radial absorption profile. Global modes can also be found using this method; in this case the power varies as $1/\nu$, while if there is a resonant layer in the plasma the power is independent of ν for sufficiently small ν. If the antenna excites neither a resonant layer nor a global mode the power is proportional to ν.

2.4. Finite element method

The principle of this method [18,19] can be summarized as follows:

1) We discretize the domain on a general non-uniform mesh $\{r_i\}^N$.
2) We expand the unknown fields Ξ in a set of basis functions Γ_j, $j = 1, \ldots, N$:

$$\Xi(r) = \sum_{j=1}^{N} x_j \Gamma_j(r). \tag{2.21}$$

The Γ_j are polynomials having a finite support (see fig. 2).

3) We introduce (2.21) into the differential equations to obtain an algebraic system of equations for the x_j. This is usually done by multiplying the equations by sufficiently regular test functions and integrating by parts. On using the basis functions as test functions we get the algebraic problem

$$\mathbf{A}x = b, \tag{2.22}$$

where b is the source term due to the antenna. The matrix A is the discretized version of the operator defined by the differential equations; in our case it is a complex non-Hermitian band matrix. Its bandwidth depends on the number of unknown field components and on the order of the basis functions.

The choice of the basis functions is in principle free. Our problem, however, presents a particularity: the existence of a continuous spectrum ($A = 0$, see (2.3)) requires that the basis

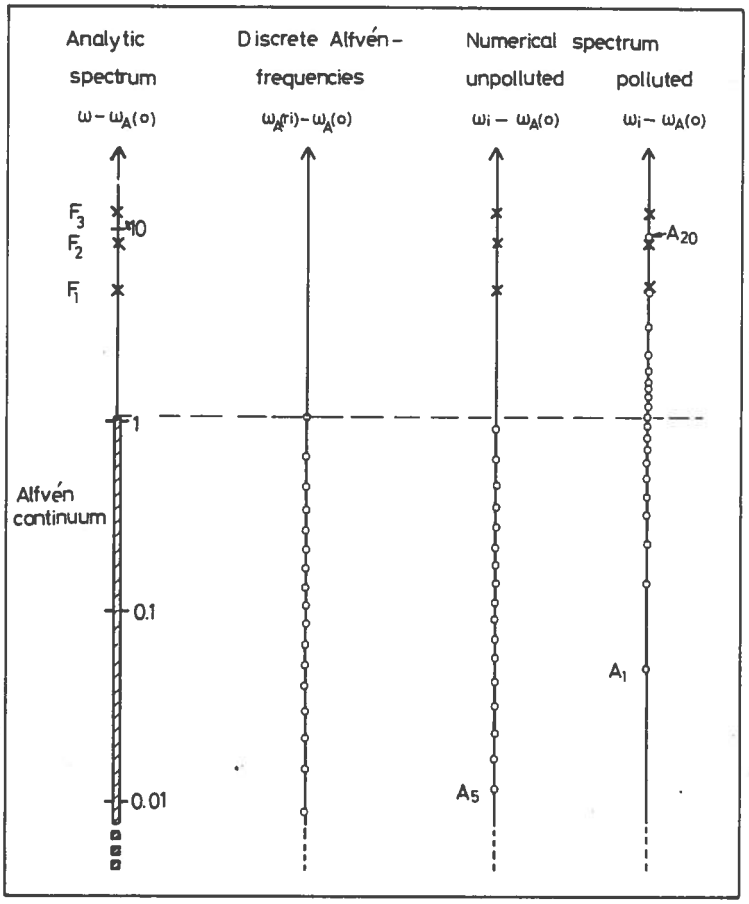

Fig. 3. From the right to the left are shown typical polluted and unpolluted spectra ω_i, together with the Alfvén frequencies $\omega_A(r_i)$ at the spatial grid points r_i, in comparison with the exact analytical spectrum. Alfvén modes (A) are shown with circles, fast magnetiosonic modes (F) with crosses.

functions reproduce locally the different singular behaviours of the different field components (2.4). Otherwise spectral pollution occurs, which means that the discretized continuum exhibits spurious modes which can be completely outside the exact range, and sometimes even spread among physical global modes. An example is given in fig. 3 (right-hand side) for the case of ideal MHD ($\omega/\omega_{ci} = 0$), using regular finite elements of first order [24]. These unphysical modes can be eliminated by increasing the number of intervals, but it can be an unrewarding task to make such convergence studies for each case. In the case of the cylindrical cold plasma, we were able to use $E_\perp$ and $B_\parallel$ as variables by eliminating E_N. Since they have the same singular behaviour (2.4), there is no problem in using regular finite elements.

However, we shall see that it is no longer possible in toroidal geometry; one is forced to use E_N and $E_\perp$ as variables which have different singular behaviour (2.4). This suggests the use of different basis functions for E_N and $E_\perp$, e.g. piecewise constant for E_N and piecewise linear for $E_\perp$, such that $dE_\perp/dr$ has the same behaviour as E_N. This technique was successfully tested in

the frame of ideal MHD [24]; spectral pollution disappears (fig. 3, second spectrum from the right).

Another technique is the use of hybrid elements [25]. It consists in considering a function and its derivative as independent variables. This technique will be presented more in detail in the next chapter.

Brief discussion

The advantage of the shooting method over finite elements is its simplicity. A problem arises, however, if there exists an evanescent wave branch: when integrating backwards, the solution will explode exponentially due to the numerical noise. Fortunately, in a cold plasma the wave is not too strongly evanescent, so that one can still guarantee a reasonable accuracy if the evanescent region is not too large. For a warm plasma, the presence of an evanescent Bernstein wave prevents completely the use of shooting methods.

On the other hand, the finite element method solves the problem as boundary value problem; unphysical exponentially growing solutions cannot appear. This is the great advantage of this method.

3. Global wave solution in two-dimensional (toroidal) geometry

3.1. Introduction

The two first successful attempts to determine a global solution of the wave equations in the ICRF in toroidal geometry were made by Itoh et al. [6,26] and Colestock et al. [27]. Both numerical methods were finite difference schemes. The first authors used a simplified geometry via expansion in inverse aspect ratio. The configuration was a cylindrical plasma with a circular cross section, a density depending on the minor radius and an axial magnetic field depending on the major radius. On the other hand, the first global wave code in real toroidal geometry, but restricted to the study of Alfvén wave heating in ideal MHD ($\omega/\omega_{ci} = 0$), was constructed a few years ago [28,9]; its development was based on the ERATO stability code [29].

In this section we present the first global wave code which solves the wave equations relevant for both Alfvén wave and ICRF heating in a cold toroidal plasma, with no geometrical approximation. The problem is formulated variationally and solved using finite hybrid elements.

3.2. Toroidal geometry

The axisymmetric equilibrium magnetic field can be written

$$\boldsymbol{B}_0 = T(\psi)\nabla\phi + \nabla\phi \times \nabla\psi, \tag{3.1}$$

where ψ = const defines a magnetic surface and ϕ is the toroidal angle (fig. 4).

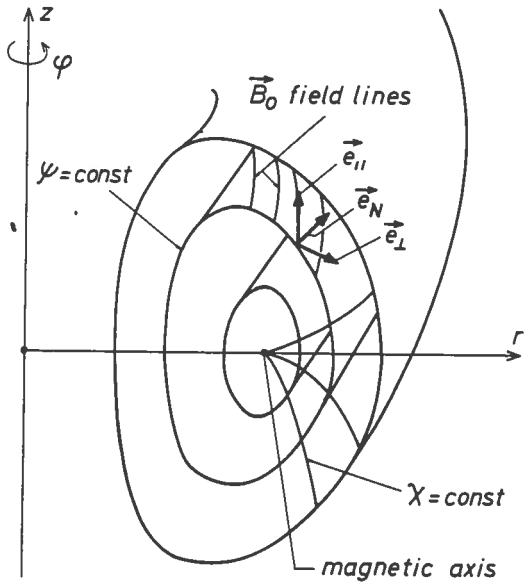

Fig. 4. Toroidal configuration showing the local magnetic coordinate system (e_N, $e_\perp$, $e_\parallel$), the polar coordinates (r, z, ϕ) and the toroidal magnetic coordinates (ψ, χ, ϕ).

The toroidal and poloidal components, $B_{0t} = T/r$ and $B_{0p} = |\nabla\psi|/r$, have a two-dimensional functional dependence. This implies that the magnitude of the magnetic field varies along a field line. As a consequence, it is impossible to define the parallel wavelength in the same way as in the cylinder by an algebraic expression (2.3); $k_\parallel$ is now not only a function of position but it is a differential operator:

$$ik_\parallel = \nabla_\parallel = \frac{1}{B_0}\boldsymbol{B}_0 \cdot \nabla. \tag{3.2}$$

This means that the relation giving the Alfvén and ion–ion hybrid perpendicular resonances ($\epsilon_{NN} - k_\parallel^2 = 0$ in 1-D) – hence the resonance absorption – is also a differential operator. This complication makes analytical work difficult. Studies by Hellsten et al. [7] indicated that the resonant surfaces lie on the magnetic surfaces ($\psi = \text{const}$). With our global code it is possible to check this result as well as to show how the usual one-dimensional picture is recovered when the size of the plasma is increased, or when the poloidal field is decreased [30].

We shall see in the next section that the magnetic surfaces ($\psi = \text{const}$) have an interesting property for the partial differential system of equations.

3.3. Equations

3.3.1. Basic equations

We consider a plasma in an axisymmetric equilibrium. The magnetic field is given by (3.1) and the density profile ρ_0, as well as the concentrations of the different ions species f_j, can be arbitrarily specified. In our case we have chosen ρ_0 and f_j to depend on ψ only. We write

Maxwell's equation in the local magnetic coordinate system $(e_N, e_\perp, e_\parallel)$ defined by $e_N = \nabla\psi/|\nabla\psi|$, $e_\parallel = B_0/B_0$, $e_\perp = e_\parallel \times e_N$

$$\text{rot rot } E - \epsilon E = 0, \tag{3.3}$$

where ϵ is the dielectric tensor of a cold current-carrying multispecies plasma. It is a differential operator. It neglects any finite β effects, such as finite Larmor radius and equilibrium pressure, but it takes into account the equilibrium plasma current density j_0. Finite electron mass has been neglected, leading to $E_\parallel = 0$. We have then

$$\epsilon = \begin{bmatrix} \epsilon_{NN} & \epsilon_{N\perp} \\ -\epsilon_{N\perp} & \epsilon_{NN} \end{bmatrix} + \frac{j_0 \cdot B_0}{B_0^2} \begin{bmatrix} \text{rot}_N e_N & \text{rot}_N e_\perp \\ \text{rot}_\perp e_N & \text{rot}_\perp e_\perp \end{bmatrix}, \tag{3.4}$$

where

$$\begin{aligned} \epsilon_{NN} &= \frac{\omega^2}{C^2} S = \frac{\omega^2}{C_A^2} \sum_i \frac{f_i}{1 - (\omega/\omega_{ci})^2}, \\ \epsilon_{N\perp} &= \frac{\omega^2}{C^2} iD = i \frac{\omega^2}{C_A^2} \sum_i \frac{f_i \omega/\omega_{ci}}{1 - (\omega/\omega_{ci})^2}. \end{aligned} \quad \text{(idem in 2.3)} \tag{3.5}$$

Notice that the operators rot_N and $\text{rot}_\perp$ act also on E. The reason why we included the equilibrium current in the dielectric tensor is that this term has been shown to be important for Alfvén wave heating in cylindrical geometry, e.g. the existence of global eigenmodes of the Alfvén wave [17], or the effect of assisting to deposit energy in the central resonant layers [31]. Whether this term is important also in the ICRF is not yet clear.

3.3.2. Variational form of the equations

It can be obtained by operating on eq. (3.3) with:

$$\int_\Omega dV \tilde{E} \cdot, \quad \Omega = \text{plasma volume}, \tag{3.6}$$

where $\tilde{E}$ is a sufficiently regular test function. After partial integration, we have

$$\int_\Omega dV \left(\text{rot } \tilde{E} \cdot \text{rot } E - \frac{j_0 \cdot B_0}{B_0^2} \tilde{E} \cdot \text{rot } E - \tilde{E} \cdot \begin{bmatrix} \epsilon_{NN} & \epsilon_{N\perp} \\ -\epsilon_{N\perp} & \epsilon_{NN} \end{bmatrix} E \right) - i\omega \int_{\partial\Omega} d\sigma \cdot (E \times B) = 0. \tag{3.7}$$

3.3.3. Singularities and symmetries

The operator in (3.7) is non-compact due to the presence of singularities. As discussed in section 3.2, they are described by a differential equation. A simple way to treat the problem is to

make the transformation

$$\epsilon_{NN} \rightarrow \epsilon_{NN} + 2i\nu\omega^2\rho_0, \tag{3.8}$$

with $\nu > 0$ to satisfy the causality. We have chosen $\nu = \text{const}$. One could also take the collisional form of ϵ_{NN} or replace ω by $\omega + i\nu$ [6]. But these options have the disadvantage that the imaginary part of ϵ_{NN} peaks around $\omega = \omega_{ci}$, with a width proportional to ν. Since ν has to be sufficiently large to turn around the discretized singularities, it would introduce pseudo-cyclotron absorption acting on the total electric field $\boldsymbol{E}$ and not only on the polarization E_+ [30].

With $\nu \neq 0$ the operator in (3.7) has no longer singularities, but it has lost its Hermiticity.

The axisymmetry of the equilibrium allows us to decompose the wave field $\boldsymbol{E}$ and the test function $\tilde{\boldsymbol{E}}$ in Fourier series in the toroidal angle

$$\begin{aligned} \boldsymbol{E} &= \sum_n \boldsymbol{E}_n e^{in\phi}, \\ \tilde{\boldsymbol{E}} &= \sum_{n'} \tilde{\boldsymbol{E}}_{n'} e^{in'\phi}. \end{aligned} \tag{3.9}$$

Introducing these expressions in the variational form (3.7) and integrating over ϕ, we can treat each Fourier component separately since for a given n only the term $n' = -n$ will contribute. We then have

$$\begin{aligned} &\partial/\partial\phi = in, \quad \text{when acting on } \boldsymbol{E}, \\ &\partial/\partial\phi = -in, \quad \text{when acting on } \tilde{\boldsymbol{E}}. \end{aligned} \tag{3.9a}$$

The operator in (3.7) is not symmetric with respect to the "updown" transformation (fig. 5)

$$\begin{aligned} \boldsymbol{B}_0 &\rightarrow -\boldsymbol{B}_0, \\ \boldsymbol{j}_0 &\rightarrow -\boldsymbol{j}_0. \end{aligned} \tag{3.10}$$

This is due to the privileged direction of the ion gyromagnetic rotation. As a consequence, we have to solve the equations not only in a half-plane like in ideal MHD, but in the whole poloidal plane.

The finite aspect ratio breaks the cylindrical symmetry. The azimuthal wavenumbers m cease to be good "quantum" numbers. They are no longer independent: toroidal coupling occurs

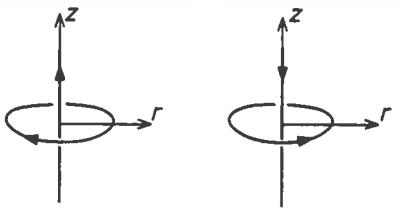

Fig. 5. Schematic view of the "up–down" transformation defined by eq. (3.10).

between modes of a given m and $m \pm 1, \ldots$. The ellipticity of the cross section couples m to $m \pm 2, \ldots$. These effects have been studied in the context of ideal MHD [9]. When a line $\omega = \omega_{ci}$ crosses the plasma, one expects the break of cylindrical symmetry to be even larger, due to the vertical ω_{ci} structure.

Let us make the following remark: each break of symmetry corresponds to a splitting of degenerated modes, thus allowing for many of them to exist and to be possibly excited by the antenna. The less the system is symmetric, the more one can expect the mode structure to be complex.

3.3.4. Toroidal coordinates

We have chosen ψ, χ, ϕ as coordinates (see fig. 4).

1) The relation $\psi = \text{const}$ defines the magnetic surfaces (eq. (3.1)). For convenience we shall use the "radial" variable s:

$$s = \sqrt{\psi/\psi_s}, \tag{3.11}$$

where ψ_s is the value of ψ at the surface of the plasma.

2) The "poloidal angle" χ is such that the Jacobian defined by

$$J = [\nabla\psi \cdot (\nabla\chi \times \nabla\phi)]^{-1} \tag{3.12}$$

becomes

$$J = qr^2/T, \tag{3.13}$$

where $T = T(\psi)$ is defined in (3.1) and $q = q(\psi)$ is the safety factor

$$q(\psi) = \frac{1}{2\pi} \oint \frac{1}{r} \frac{B_{0t}}{B_{0p}} \mathrm{d}l, \tag{3.14}$$

where $\mathrm{d}l$ is a length element in the poloidal plane on a $\psi = \text{const}$ surface. We have

$$\mathrm{d}l = JB_{0p}\, \mathrm{d}\chi \tag{3.15}$$

Notice that r^2/J is a function of ψ only.

3) The choice of the toroidal angle ϕ is natural since we have decomposed the wave field in Fourier series in ϕ (3.9).

Instead of E_N and $E_\perp$, we shall use the variables V and X defined by

$$E = \frac{VT}{2\psi_s s} \nabla\psi - XT\nabla\chi + \frac{Xr^2}{J} \nabla\phi. \tag{3.16a}$$

Thus

$$E_N = \frac{T|\nabla\psi|}{2\psi_s s}(V - \beta_\chi X),$$
$$E_\perp = -\frac{r^2 B_0}{J|\nabla\psi|}X, \tag{3.16b}$$

where β_χ is the non-orthogonality:

$$\beta_\chi = \frac{2\psi_s s}{|\nabla\psi|^2}\nabla\psi\cdot\nabla\chi. \tag{3.16c}$$

Using the relations

$$\nabla = \nabla\psi\frac{\partial}{\partial\psi} + \nabla\chi\frac{\partial}{\partial\chi} + \nabla\phi\frac{\partial}{\partial\phi},$$
$$\boldsymbol{B}_0\cdot\nabla = \frac{1}{J}\left(\frac{\partial}{\partial\chi} + q\frac{\partial}{\partial\phi}\right),$$
$$\frac{\partial}{\partial\psi} = \frac{1}{2\psi_s s}\frac{\partial}{\partial s}, \tag{3.17}$$
$$\mathrm{d}V = 2J\psi_s s\,\mathrm{d}s\,\mathrm{d}\chi,$$

one can write

$$\mathrm{rot}\,\boldsymbol{E} = \left(\nabla\frac{VT}{2\psi_s s}\right)\times\nabla\psi - (\nabla XT)\times\nabla\chi + \left(\nabla\frac{Xr^2}{J}\right)\times\nabla\phi$$
$$= A_1\frac{\nabla\psi}{|\nabla\psi|} + A_2\frac{\nabla\phi}{|\nabla\phi|} + A_3\frac{\nabla\phi\times\nabla\psi}{|\nabla\phi||\nabla\psi|},$$
$$A_1 = \frac{r^2}{J^2|\nabla\psi|}\left(\frac{\partial}{\partial\chi} + inq\right)X,$$
$$A_2 = \frac{-B_{0t}r^2}{2\psi_s sJ}\left(\frac{\partial X}{\partial s} + \frac{\partial V}{\partial\chi} + \left(\frac{\partial}{\partial s}\ln T\right)X\right), \tag{3.18}$$
$$A_3 = \frac{B_{0p}r^2}{2\psi_s sJ}\left(inq(V - \beta_\chi X) - \frac{\partial X}{\partial s} - \beta_\chi\frac{\partial X}{\partial\chi} - \left(\frac{\partial}{\partial s}\ln\frac{r^2}{J}\right)X\right).$$

The same expression holds for rot $\tilde{\boldsymbol{E}}$, except that n has to be replaced by $-n$ (see (3.9b)). With the relations (3.16)–(3.18), the variational form (3.7) can be written as

$$\int_0^1 \mathrm{d}s\int_0^{2\pi}\mathrm{d}\chi\left(\sum_{j=1}^{8} c_j I_j^* J_j\right) + S = 0, \tag{3.19a}$$

where

$$
\begin{aligned}
&I_1 = J_1 = X,\\
&I_2 = J_2 = V - \beta_\chi X,\\
&I_3 = X, \quad J_3 = V,\\
&I_4 = V, \quad J_4 = X,\\
&I_5 = J_5 = \partial X/\partial\chi + \mathrm{i}nqX,\\
&I_6 = J_6 = \partial X/\partial s + \partial V/\partial\chi,\\
&I_7 = J_7 = \partial X/\partial s + \beta_\chi \partial X/\partial\chi + \beta_\chi \mathrm{i}nqX + HX - \mathrm{i}nqV,\\
&I_8 = J_8 = X,
\end{aligned}
\tag{3.19b}
$$

$$
\begin{aligned}
c_1 &= \frac{-2\psi_s s r^2}{B_{0\mathrm{p}}^2 J}\hat{\epsilon},\\
c_2 &= \frac{-JB_{0\mathrm{p}}^2 B_{0\mathrm{t}}^2 r^4}{2\psi_s s B_0^2}\hat{\epsilon},\\
c_3 &= \frac{-B_{0\mathrm{t}} r^3}{B_0}\mathrm{i}\hat{g},\\
c_4 &= -c_3,\\
c_5 &= \frac{2\psi_s s r^2}{B_{0\mathrm{p}}^2 J^3},\\
c_6 &= \frac{B_{0\mathrm{t}}^2 r^4}{2\psi_s s J},\\
c_7 &= \frac{B_{0\mathrm{p}}^2 r^4}{2\psi_s s J},\\
c_8 &= \frac{-2r^4 q_0 K}{Js},
\end{aligned}
\tag{3.19c}
$$

$$
\begin{aligned}
\hat{\epsilon} &= \rho_0\omega^2 \sum_k \frac{f_k}{1-(\omega/\omega_{ck})^2},\\
\hat{g} &= \rho_0\omega^2 \sum_k \frac{f_k \omega/\omega_{ck}}{1-(\omega/\omega_{ck})^2},\\
H &= \frac{\partial}{\partial s}\ln\frac{r^2}{J} + \frac{2\psi_s s}{r B_{0\mathrm{p}}^2} j_{0\phi},\\
K &= \frac{2\psi}{q_0}\left(\frac{j_{0\phi}^2}{r^2 B_{0\mathrm{p}}^2} + \frac{j_{0\phi}}{2r}\frac{\partial}{\partial\psi}\ln r^2 B_{0\mathrm{p}}^2\right),\\
j_{0\phi} &= \boldsymbol{j}_0 \cdot \nabla\phi/|\nabla\phi|,
\end{aligned}
\tag{3.19d}
$$

$$S = -\mathrm{i}\omega \int_{\partial\Omega} \mathrm{d}\sigma \cdot (\tilde{\boldsymbol{E}} \times \boldsymbol{B}). \tag{3.19e}$$

This section may appear unnecessarily complicated to the reader who is unfamiliar with toroidal geometry. For example, one may think that it is much simpler for the algebra to take r, z, ϕ as coordinates. In this case both variables have derivatives with respect to r and z, making the differential system appear as a fourth-order system. The great advantage of using magnetic coordinates is that one variable, V, has no derivative in the ψ direction, thus lowering the order of the differential operator. This has many advantages for the numerical resolution. Moreover, we have the same differential structure as for the ideal MHD stability problem. It is then natural to take advantage of the existence of the numerical code ERATO [29] by using the same coordinate system.

3.3.5. Regularity, boundary and matching conditions. Vacuum solution

The regularity on the magnetic axis ($s = 0$) imposes the fields to remain finite. Since $\lim_{s\to 0} |\nabla\psi| = 0$ and $\lim_{s\to 0} |\nabla\psi|/s = \text{const}$, from (3.16) we conclude

$$\lim_{s\to 0} X = 0. \tag{3.20}$$

The surface term S in (3.19) has to be connected to the vacuum solution via boundary conditions. Here we require the fields be continuous across the plasma–vacuum interface.

Our model of antenna is a current-carrying sheet surrounding the plasma (fig. 6). As in the 1-D case, we shall neglect the displacement current. The antenna surface is defined by

$$D(\boldsymbol{r}) = 0 \tag{3.21}$$

and its current j_a, satisfying automatically $\nabla \cdot j_a = 0$, is

$$j_a = \delta(D)\nabla D \times \nabla\beta \exp(\mathrm{i}(n\phi - \omega t)), \tag{3.22}$$

where β is the "current potential". For the sake of simplicity we assume β to be a function of θ

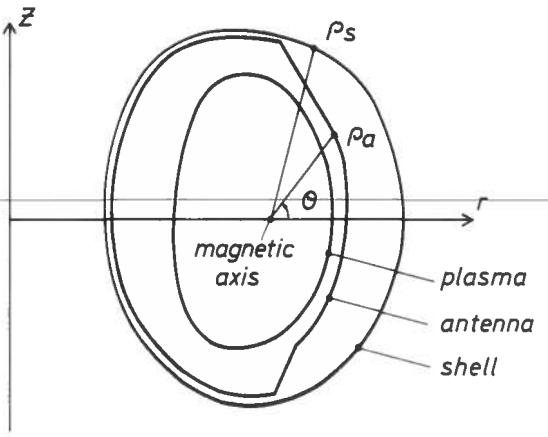

Fig. 6. Poloidal cross sections of the plasma, antenna and shell surfaces.

only where θ is the poloidal angle (see fig. 6). Then β determines the current in the poloidal direction, and $\mathrm{d}\beta/\mathrm{d}\theta$ is related to the current in the toroidal direction [9].

The matching conditions at the antenna are

$$\begin{aligned} &\boldsymbol{n}_a \times [\![\boldsymbol{B}]\!] = \boldsymbol{n}_a \times \nabla\beta, \\ &\boldsymbol{n}_a \cdot [\![\boldsymbol{B}]\!] = 0, \end{aligned} \tag{3.23}$$

where $\boldsymbol{n}_a$ is the outer normal to the antenna; the double bracket indicates a jump across the antenna from the inside to the outside.

The vacuum region is surrounded by a perfectly conducting shell where we have

$$\boldsymbol{n}_s \cdot \boldsymbol{B} = 0, \tag{3.24}$$

where $\boldsymbol{n}_s$ is the outer normal to the shell.

The vacuum equations are

$$\begin{aligned} &\boldsymbol{B} = \nabla\Phi, \\ &\nabla^2\Phi = 0. \end{aligned} \tag{3.25}$$

We are now ready to express the surface term S (3.19e) in terms of the vacuum solution. S can be written, using $E_\parallel = 0$ in the plasma, as

$$S = -\mathrm{i}\omega \int_{\partial\Omega} \tilde{E}_\perp B_\parallel \mathrm{d}\sigma. \tag{3.26}$$

Using the vacuum equations (3.25) and the identity

$$\mathrm{rot}_N(\Phi\tilde{\boldsymbol{E}}) = \mathrm{i}\omega\Phi\tilde{B}_N + \tilde{E}_\perp B_\parallel, \tag{3.27}$$

we have

$$S = \omega^2 \int_{\partial\Omega} \Phi\tilde{B}_N \mathrm{d}\sigma, \tag{3.28}$$

or, with $\mathrm{i}\omega B_N = -\nabla_\parallel E_\perp$,

$$S = \mathrm{i}\omega \int_{\partial\Omega} \Phi\nabla_\parallel \tilde{E}_\perp \mathrm{d}\sigma. \tag{3.29}$$

The potential Φ is functionally related to its normal derivative on the boundaries of the vacuum region (the plasma boundary, antenna and shell) via Green's theorem. Using the boundary and matching conditions (3.23) and (3.24) one can write Φ on the plasma boundary as

$$\Phi(\boldsymbol{r}) = \int_{\partial\Omega} Q(\boldsymbol{r}, \boldsymbol{r}')\nabla\Phi(\boldsymbol{r}') \cdot d\boldsymbol{\sigma}' + \Phi_E(\boldsymbol{r}), \tag{3.30}$$

where Φ_E is the source term due to the antenna. The derivation of the full expressions for Q and Φ_E has been given in ref. [9].

Introducing (3.30) into (3.29), we obtain

$$S = -\int_{\partial\Omega}\int_{\partial\Omega} Q(r, r')\big(\nabla_\parallel \tilde{E}_\perp(r')\big)\big(\nabla_\parallel E_\perp(r)\big)\mathrm{d}\sigma\mathrm{d}\sigma'$$

$$+\mathrm{i}\omega\int_{\partial\Omega}\Phi_E(r')\big(\nabla_\parallel \tilde{E}_\perp(r')\big)\mathrm{d}\sigma', \tag{3.31a}$$

with

$$\begin{aligned}
&Q = M_{pp}^{-1}\big(E_{pp} - (D_{ps} - 2I)D_{ss}^{-1}E_{sp}\big),\\
&\Phi_E = M_{pp}^{-1}\big((D_{ps} - 2I)D_{ss}^{-1}D_{sa} + 2I - D_{pa}\big)\beta,\\
&M_{pp} = D_{pp} - 2I - (D_{ps} - 2I)D_{ss}^{-1}D_{sp},\\
&D_{\mu\nu}f(r) = \frac{1}{2\pi}\int_\nu (f(r') - f(r))\nabla' G(r_\mu, r'_\nu)\cdot \mathrm{d}\sigma',\\
&E_{\mu\nu}f(r) = \frac{1}{2\pi}\int_\nu G(r_\mu, r'_\nu)\nabla' f(r')\cdot \mathrm{d}\sigma',\\
&G(r_\mu, \nu) = 1/|r_\mu - r_\nu|,
\end{aligned} \tag{3.31b}$$

μ, ν = p (plasma), a (antenna) or s (shell).

An alternative to the Green's function technique is the numerical integration of vacuum equations, e.g. using finite elements [32].

Once the antenna current (3.22) is specified, the solution of the variational form (3.19), with its vacuum contribution (3.31a) and the regularity condition (3.20), is uniquely determined. Before explaining the numerical construction of this solution, we shall derive a few expressions which are interesting from the physical point of view.

3.3.6. Power, Poynting flux and power balance

The total power delivered by the antenna is

$$P_a = \tfrac{1}{2}\int_V \mathrm{d}V\, j_a\cdot E^*, \quad V = \text{vacuum region}. \tag{3.32}$$

It can be written, using the definition of the antenna current (3.22), after partial integration and use of Maxwell's equations as

$$P_a = -\frac{\mathrm{i}\omega}{2}\int_a \beta B^*\cdot \mathrm{d}\sigma_a. \tag{3.33}$$

The integral is a surface integral along the antenna. With the same Green's function technique as

described above, $\boldsymbol{B}^* \cdot \mathrm{d}\boldsymbol{\sigma}_a$ can be expressed as a surface integral along the plasma–vacuum interface

$$\boldsymbol{B}^* \cdot \mathrm{d}\boldsymbol{\sigma}_a = \int_p Z(r_a, r_p)\left(\nabla_\parallel E_\perp^*(r_p)\right)\mathrm{d}\sigma_p + \Psi_E(r_a), \tag{3.34}$$

and

$$P_a = -\frac{i\omega}{2}\left(\int_a \beta(r_a)\int_p Z(r_a, r_p)\left(\nabla_\parallel E_\perp^*(r_p)\right)\mathrm{d}\sigma_p \mathrm{d}\sigma_a + \int_a \beta(r_a)\Psi_E(r_a)\mathrm{d}\sigma_a\right), \tag{3.35a}$$

with

$$\begin{aligned} Z &= T_{pa}^{-1}(V_{pp} - U_{pp}Q), \\ \beta\Psi_E &= T_{pa}^{-1}U_{pp}\Phi_E, \\ T_{pa} &= E_{pa} - (D_{pa} - 2I)D_{aa}^{-1}E_{aa}, \\ U_{pp} &= D_{pp} - 2I - (D_{pa} - 2I)D_{aa}^{-1}D_{ap}, \\ V_{pp} &= E_{pp} - (D_{pa} - 2I)D_{aa}^{-1}E_{ap}. \end{aligned} \tag{3.35b}$$

Another interesting quantity is the total power transmitted through the plasma surface

$$P_p = \tfrac{1}{2}\int_{\partial\Omega} (\boldsymbol{E}^* \times \boldsymbol{B}) \cdot \mathrm{d}\boldsymbol{\sigma}_p. \tag{3.36}$$

It can be evaluated either from the explicit calculation of the Poynting vector $\boldsymbol{S}$, or directly from the variational form (see (3.7)).

The global power balance is

$$\mathrm{Re}\ P_a = \mathrm{Re}\ P_p. \tag{3.37}$$

The local power absorption density div $\frac{1}{2}\mathrm{Re}\,(\boldsymbol{E}^* \times \boldsymbol{B})$ can be written as

$$P_d(r) = \frac{1}{2\omega}\left(\mathrm{Im}\ \epsilon_{NN}|E_+|^2 + 2\mathrm{Im}(\epsilon_{NN} + i\epsilon_{N\perp})\mathrm{Im}(E_N^* E_\perp)\right). \tag{3.38}$$

In our case we have an imaginary part only in ϵ_{NN} (see (3.8)); thus this relation reduces to

$$P_d(r) = \frac{1}{2\omega}\mathrm{Im}\ \epsilon_{NN}|\boldsymbol{E}|^2. \tag{3.39}$$

To check the validity of the solution, we compare the power absorbed in a given volume with the Poynting flux across the surface of this volume. Let Ω_ψ be a torus defined by a ψ = const surface, and let us define the Poynting flux P_s as

$$P_s(\psi) = \tfrac{1}{2}\int_{\partial\Omega_\psi} \mathrm{Re}(\boldsymbol{E} \times \boldsymbol{B}) \cdot \mathrm{d}\boldsymbol{\sigma}_\psi \tag{3.40}$$

and the power flux P_e as

$$P_e(\psi) = \int_{\Omega_\psi} P_d(\boldsymbol{r}) \mathrm{d}V. \tag{3.41}$$

The local power balance is evidently

$$P_s(\psi) = P_e(\psi), \quad \forall\psi. \tag{3.42a}$$

One can also compare $\mathrm{d}P_s/\mathrm{d}\psi$ with $\int_{\partial\Omega_\psi} P_d(\boldsymbol{r})\mathrm{d}\sigma_\psi$. (3.42b)

Finally, we must have

$$\mathrm{Re}\ P_a = \mathrm{Re}\ P_p = P_s(\psi_s) = P_e(\psi_s), \tag{3.43}$$

where ψ_s is the magnetic flux at the plasma–vacuum interface. The Poynting vector $\boldsymbol{S} = \boldsymbol{E}^* \times \boldsymbol{B}$ can be evaluated using $\boldsymbol{B} = (1/\mathrm{i}\omega)\ \mathrm{rot}\ \boldsymbol{E}$ and the expression (3.18) for rot $\boldsymbol{E}$.

3.4. Numerical solution of the variational form

We now have all the material necessary to describe the numerical scheme used in the LION code. It consists of five distinct parts.

3.4.1. Equilibrium

The equilibrium can be computed either in a separate code or by using the Solovev analytical model [33]. In both cases one obtains the values of ψ, solution of the Grad–Shafranov equation, on a rectangular mesh in (r, z): $\{\psi_{ij} = \psi(r_i, z_j),\ i = 1, \ldots, N_r,\ j = 1, \ldots, N_z\}$. In the actual version of the code the equilibrium is assumed to be symmetric in z is determined only in the upper half-plane. The plasma domain is covered with a rectangular non-uniform mesh in (s, χ): $\{(s_i, \chi_j),\ i = 1, \ldots, N_\psi,\ j = 1, \ldots, N_{\mathrm{pol}}\}$ (s is defined in eq. (3.11)). The information has to be inverted, i.e. for a given (s_i, ψ_j) we have to find the corresponding r and z coordinates and all the equilibrium quantities needed for the calculation of the coefficients of the variational form (3.19). The code works in dimensionless units such that the major radius R_0, the equilibrium magnetic field B_0, the mass density ρ_0 and the Alfvén transit-time R_0/C_A are normalised to their values on the magnetic axis.

3.4.2. Vacuum

The vacuum region contains the antenna and shell surfaces. These are given by arbitrary functions $\rho_a(\theta)$ and $\rho_s(\theta)$ (fig. 6). The antenna current is specified by the function $\beta(\theta)$ in eq. (3.22). Different forms of $\rho_a(\theta)$ and $\beta(\theta)$ will define various antenna models: helical, low field side, high field side, both high and low field sides, or top–bottom.

The vacuum contribution (3.31) to the variational form is represented by a matrix and a source vector. These are obtained by calculating Q and Φ_E according to the relations (3.31b).

Notice that the boundary and matching conditions are included in these expressions. Everything is then prepared for the calculation of the power delivered by the antenna (3.35): we evaluate Z and $\beta\Psi_E$ according to (3.35b).

3.4.3. Plasma

We have chosen to use finite hybrid elements for the following reasons. Firstly, we want our code to be valid for any aspect ratio, in particular in the cylindrical limit, where we know that regular finite elements may cause trouble due to the spectral pollution (fig. 3). Secondly, the hybrid elements lead to simpler integration formulas than the regular ones. Nevertheless, they have the same convergence laws. Thirdly, the LION code has been developed from the ERATO stability code which uses finite hybrid elements of first order and it was most convenient to retain the same elements.

Let us now describe the principle of the method. Instead of solving the variational form (3.19) as

$$\mathscr{L}(X, V) = 0, \tag{3.44}$$

we consider

$$\mathscr{L}\left(\frac{\partial X^{(1)}}{\partial \chi}, X^{(2)}, \frac{\partial X^{(3)}}{\partial s}, \frac{\partial V^{(1)}}{\partial \chi}, V^{(2)}\right) = 0, \tag{3.45}$$

with the evident relations

$$X^{(1)} = X^{(2)} = X^{(3)}, \quad V^{(1)} = V^{(2)}, \tag{3.46}$$

An equivalent way to write (3.46) is

$$\lim_{\Delta \to 0} \frac{1}{\Delta} \int_{\Delta} (X^{(1)} - X^{(2)}) \mathrm{d}V = 0, \quad \forall \Delta \subset \Omega, \tag{3.47}$$

and the same for the other relations. After discretization we restrict the conditions (3.47) by identifying Δ with a mesh cell. When the number of these cells tends to infinity we recover the initial problem (3.44).

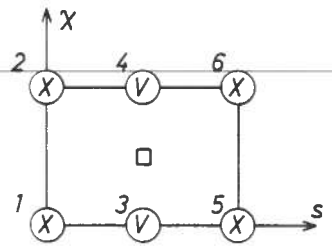

Fig. 7. A mesh with its 6 nodal points and their local numbering. The small square in the centre is the point where the relations (3.48) are defined.

We expand $X^{(1)}$, $X^{(2)}$, $X^{(3)}$, $V^{(1)}$ and $V^{(2)}$ in a set of basis functions. The simplest choice is made, i.e. we require each term in the variational form (3.19) be constant on each mesh cell. The shape of these basis functions is given in ref. [29]. The integration reduces to a multiplication of the value of the integrand at the centre of a cell by the volume of this cell. We define x_j as the values of X and V on the nodal points. Fig. 7 shows their positions in a mesh cell and their local numbering, $j = 1$ to 6. At the centre of the cell we have

$$\begin{aligned}
\frac{\partial X^{(1)}}{\partial \chi} &= \frac{x_2 + x_6 - x_1 - x_5}{2\Delta\chi}, \\
X^{(2)} &= \frac{x_1 + x_2 + x_5 + x_6}{4}, \\
\frac{\partial X^{(3)}}{\partial s} &= \frac{x_5 + x_6 - x_1 - x_2}{2\Delta s}, \\
\frac{\partial V^{(1)}}{\partial \chi} &= \frac{x_4 - x_3}{\Delta\chi}, \\
V^{(2)} &= \frac{x_3 + x_4}{2}.
\end{aligned} \tag{3.48}$$

For each mesh cell we calculate the contribution to the variational form (3.19) using the formulas (3.48). This yields 6×6 "local matrices" which have to be added in the proper way to the total matrix **A** of the discretized form. This is done by choosing a global numbering of the nodal points. The matrix **A** is constructed by blocks of contributions of $s = \text{const}$ cells (fig. 8). The numbering is non-monotonic in χ and the periodicity in χ is automatically satisfied. The matrix obtained has the structure shown in fig. 9. It consists of N_ψ blocks which partly overlap; each block is subdivided in 9 subblocks of dimensions $N_{\text{pol}} \times N_{\text{pol}}$, each subblock is a band matrix of bandwidth 5. We introduce the regularity condition (3.20) on the first block. The

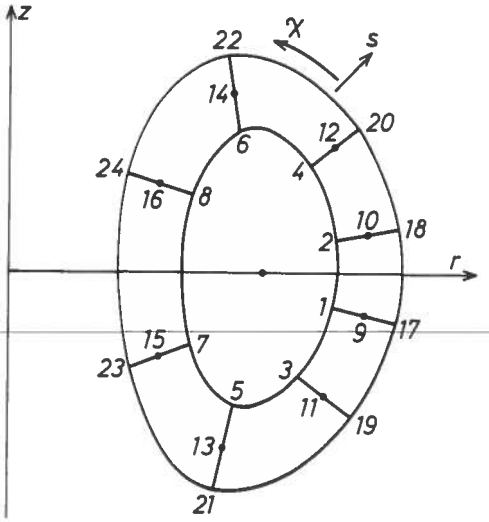

Fig. 8. A set of $s = \text{const}$ cells with the global numering of the nodal points for $N_{\text{pol}} = 8$.

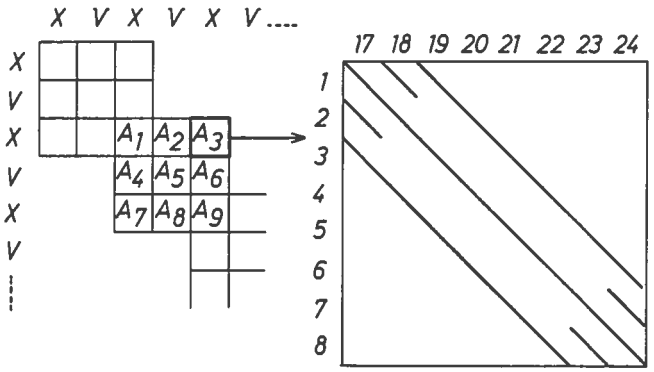

Fig. 9. Block and subblock structure of the matrix **A** for the numbering shown in fig. 8. The subblock $\mathbf{A}_9$ is the subblock $\mathbf{A}_1$ of the next block.

vacuum contribution (3.31) is added to the last block. The matrix **A** is complex and non-Hermitian. In the actual version of the code we store the full blocks, not profiting from the many zeros they contain. However, it is possible to gain a substantial amount of storage by using sparse matrix techniques. We shall discuss this point later.

3.4.4. Algebra

The problem has been reduced to the determination of the solution of the linear system of algebraic equations

$$\mathbf{A}x = b, \tag{3.49}$$

where b is the source vector due to the antenna (see(3.31)). We decompose **A** into **LDU** where **L** and **U** are lower and upper triangular matrices and **D** is a diagonal matrix. The solution x is then obtained in two steps

$$\begin{aligned} y &= \mathbf{L}^{-1}b, \\ x &= \mathbf{U}^{-1}\mathbf{D}^{-1}y. \end{aligned} \tag{3.50}$$

The matrices are treated block by block with subsequent input/output operations.

We check the validity of the solution x by substituating it into eqs. (3.49) and comparing the norm of $\mathbf{A}x$ with the norm of b. In all cases the results agree to 13 digits, hence the matrix **A** is well conditionned for this elimination procedure. Since the variational form itself can be considered as a power balance relation (see (3.7)), and since we solve it exactly, we have found a formulation in which the power balance is exactly satisfied.

3.4.5. Diagnostics

The total power delivered by the antenna, P_a, is evaluated according to (3.35). The total power transmitted through the plasma surface, P_p (3.36), is calculated directly from the source vector and the solution at plasma–vacuum interface

$$P_p = \frac{-1}{i\omega} x^* \cdot b. \tag{3.51}$$

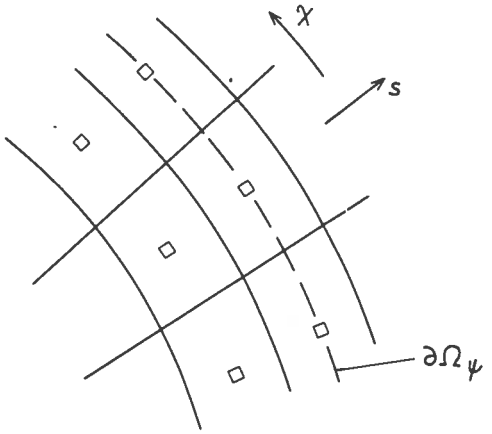

Fig. 10. Surface $\partial\Omega_\psi$ passing through the centres of the mesh cells where the Poynting and power fluxes, $P_s(\psi)$ and $P_e(\psi)$, defined by eqs. (3.40) and (3.41), are compared.

From the solution x we reconstruct the variables X and V as well as their derivaties $\partial X/\partial\chi$, $\partial X/\partial s$ and $\partial V/\partial\chi$ according to (3.48). We use the definition of X and V (3.16b) to obtain the components of the wave electric field E_N and $E_\perp$, the expression (3.18) for rot E to calculate the wave magnetic field B_N, $B_\perp$ and $B_\parallel$ and the Poynting vector S_N, $S_\perp$ and $S_\parallel$. The polarizations of the electric field $E_\pm = E_N \pm iE_\perp$ and the Fourier decomposition of the solution in the poloidal angle χ are also computed. The power absorption density P_d (3.38), the Poynting flux $P_s(\psi)$ (3.40) and the power flux $P_e(\psi)$ (3.41) are constructed, and the related power balances (3.42) (3.43) are checked.

We have to be careful in comparing $P_s(\psi)$ with $P_e(\psi)$. According to the finite hybrid elements (3.48), the fields $\boldsymbol{E}$, $\boldsymbol{B}$ and $\boldsymbol{S}$ associated with the wave are defined at the centre of each mesh cell. The comparison between $P_s(\psi)$ and $P_e(\psi)$ has to be done on a surface $\partial\Omega_\psi$ passing through the centres of the cells (fig. 10). Therefore we have to take into account only one half of the volume of the exterior cells when integrating $P_e(\psi)$.

The real antenna structure can be decomposed in Fourier series in the toroidal angle. For each Fourier component we repeat the calculation presented in sections 3.4.1 to 3.4.5. The total power is simply the sum of the powers of all components.

3.4.6. An application of the LION code to JET

As an illustrative case we show an example of the mode conversion scenario at the ion–ion hybrid resonance in JET. The plasma contains a mixture of deuterium (96.6%) and helium-3 (3.4%). The antenna is on the low field side. The antenna current, given by the function $\beta(\theta)$ in eq. (3.22), has been chosen to be constant and purely poloidal. Its excitation frequency is such that it matches the cyclotron frequency of helium-3 32 cm from the magnetic axis towards the high field side. We show here only one toroidal Fourier component ($n = 3$). The equilibrium is of the Solovev type with an expect ratio of 3, an ellipticity of 1.3 and a safety factor on axis of 1.11. The other parameters are $n_e = 3 \times 10^{19}$ m^{-3}, $B_0 = 3.5$ T, $R_0 = 3$ m, the frequency $\omega/2\pi = 35$ MHz, $\nu = 10^{-2}$. The mesh used in this computation is 100 intervals in the radial direction

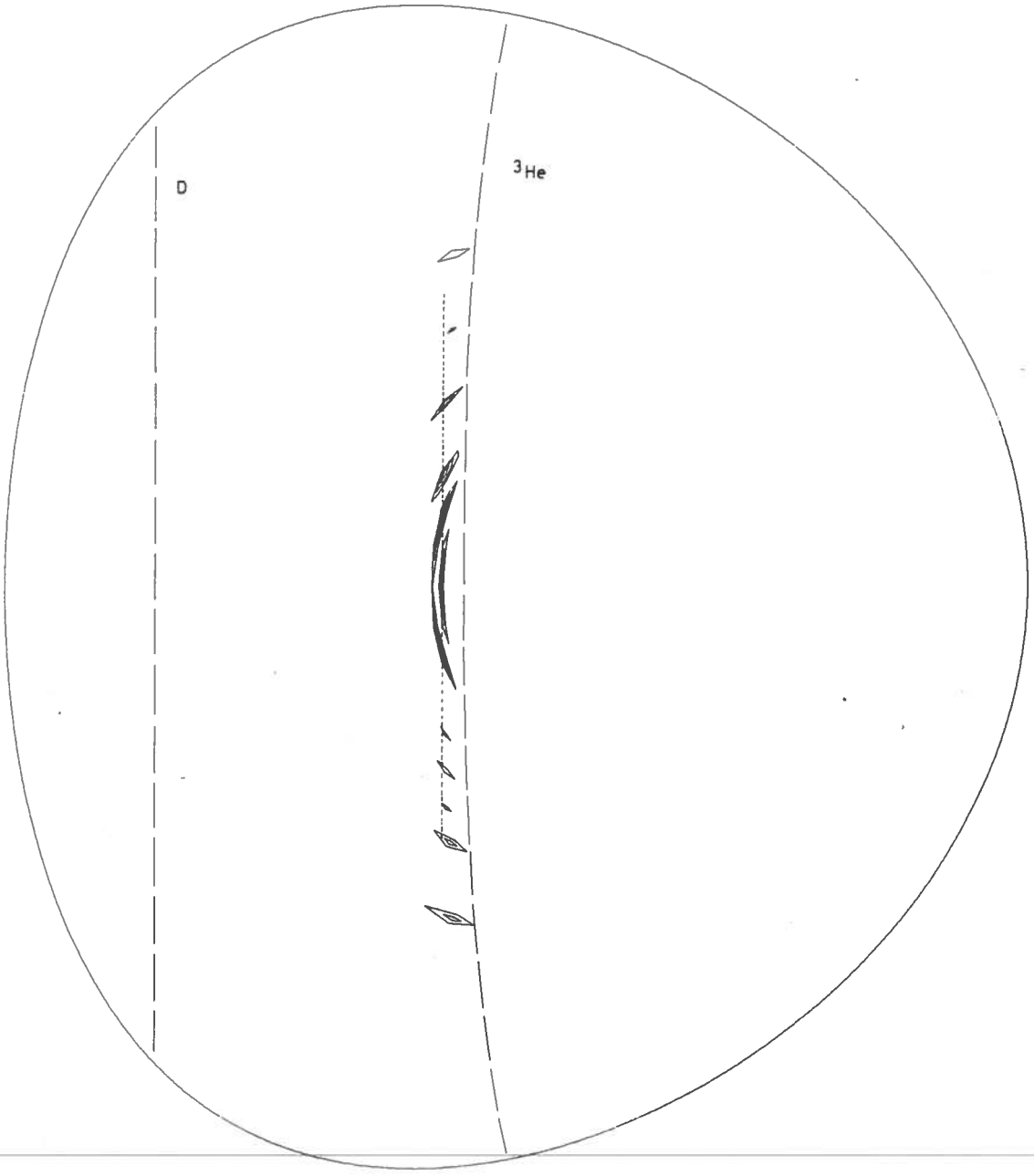

Fig. 11. Contour lines of the power absorption density for a mode conversion scenario in JET in a deuterium plasma with 3.4% helium-3. The parameters are: $n_e = 3\times10^{19}$ m^{-3}, $B_0 = 3.5$ T, $R_0 = 3$ m, aspect ratio = 3, frequency = 35 MHz, low field side antenna, $n = 3$, $\nu = 10^{-2}$. The dashed lines indicate where the frequency matches the cyclotron frequencies of deuterium and helium-3. The dotted line is the approximate resonance condition $\epsilon_{NN} - n^2/r^2 = 0$.

($N_\psi = 100$) and 50 intervals in the poloidal direction ($N_{pol} = 50$). This mesh size (5000 cells) is approximately the maximum of what can be handled on a CDC-Cyber 855. It requires 500 s of central processor time and 89000 words of central memory. The turn-around time is long due to the many input/output operations.

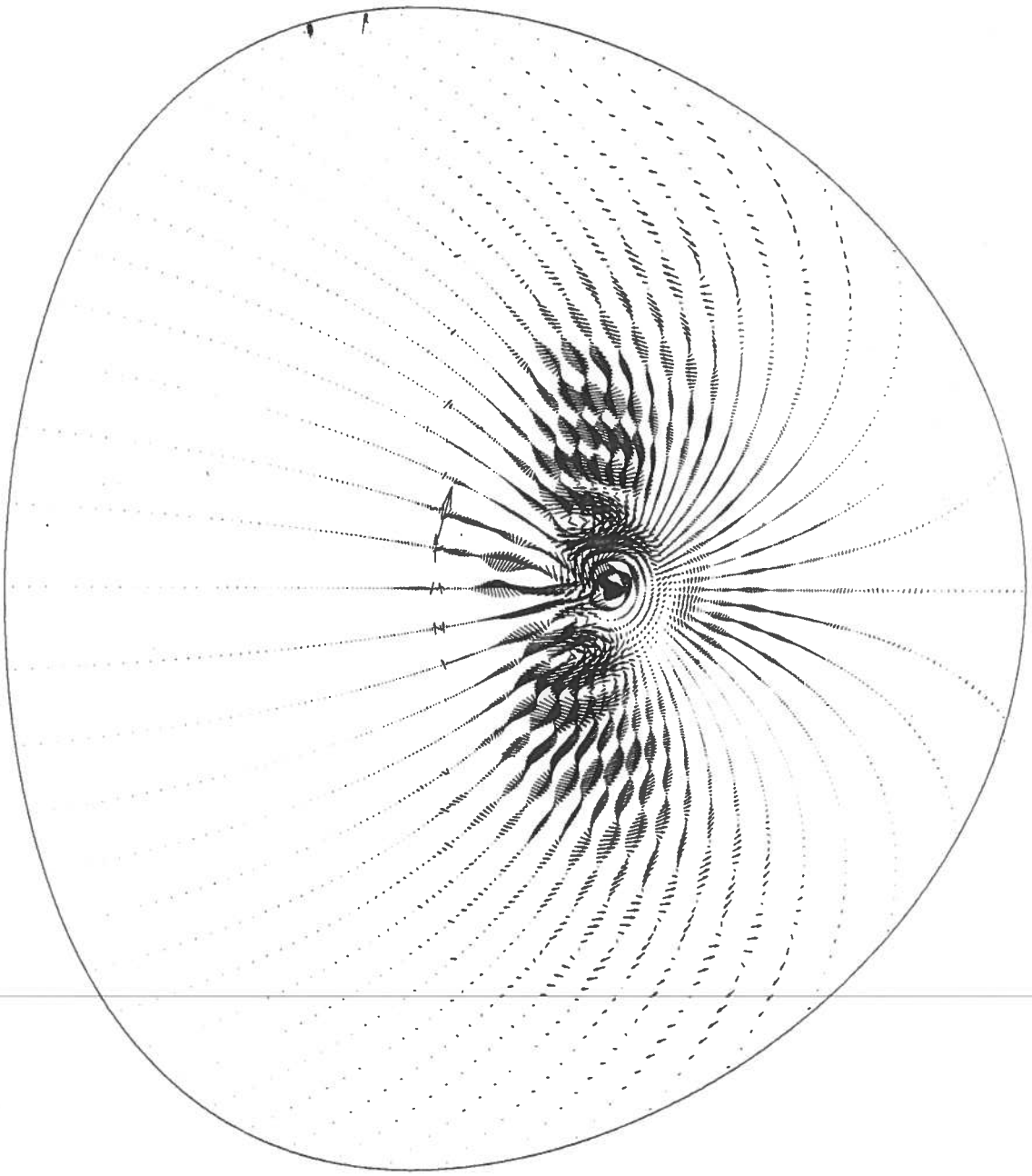

Fig. 12. Poynting vector for the case shown in fig. 11. The parallel component is not represented.

The contours of the power absorption density are plotted in fig. 11. Notice that the resonances are located on pieces of magnetic surfaces at specific places along the line $\epsilon_{NN} - n^2/r^2 = 0$ (dotted line) which usually defines the resonance condition in the WKB approximation. The

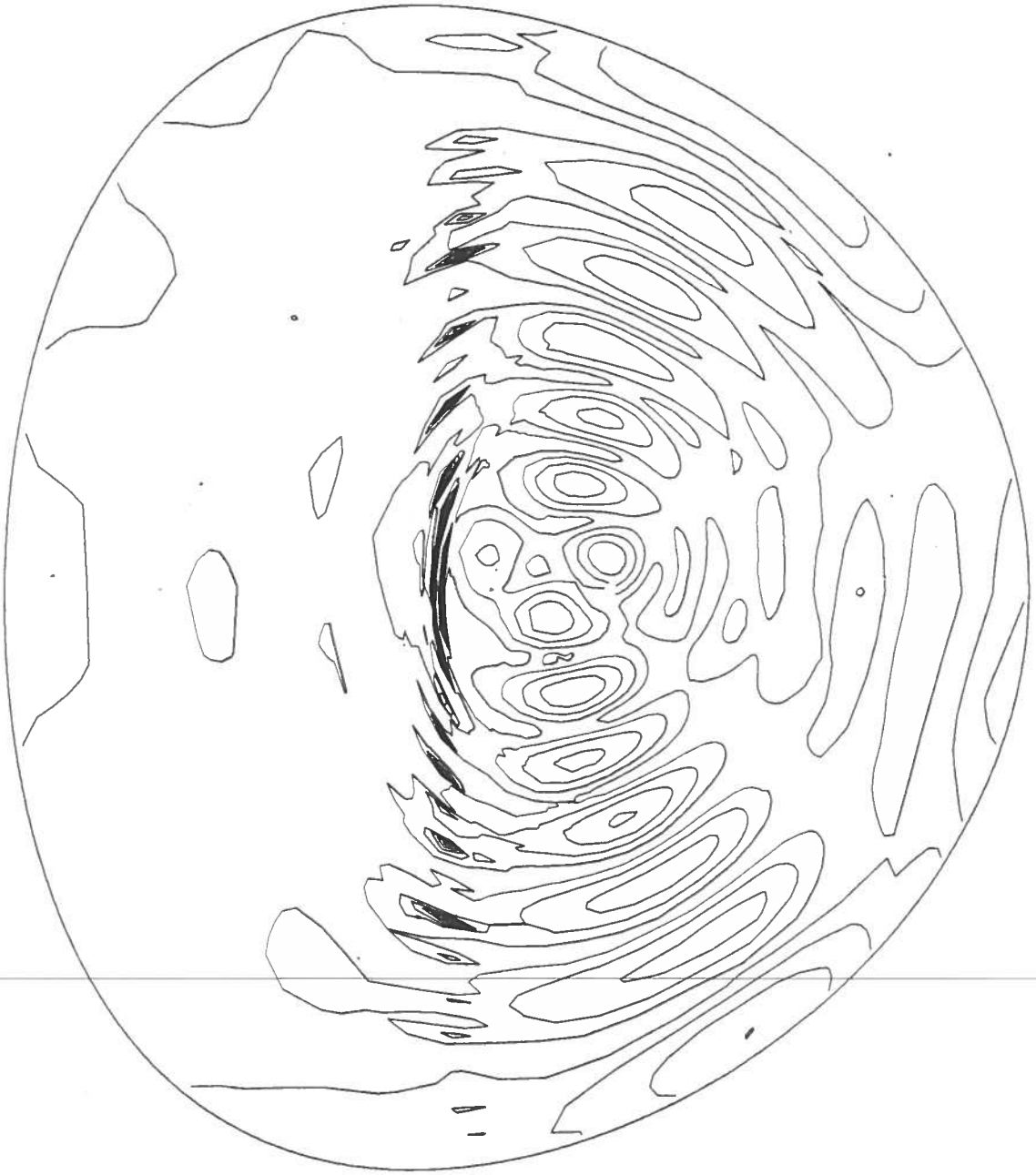

Fig. 13. Contour lines of the circular left-hand polarization of the electric field, $|E_+| = |E_N + iE_\perp|$, for the case shown in fig. 11.

Poynting vector (fig. 12) shows a complicated fine structure which results from the superposition of the "incoming" and "partly reflected" waves. The contour plot of the absolute value of one circular component of the polarization of the wave electric field, $|E_+| = |E_N + iE_\perp|$, is shown in fig. 13. Notice the focalization of the fast wave towards the central regions.

Let us now turn to the various checks of this calculation. Firstly, we have $\mathbf{A}x = b$ to all digits (10^{-14}) which means that the solution of the discretized problem is exact. Secondly, the total powers, P_a (3.35) and P_p (3.36), are equal with an accuracy of 3%. Thirdly, the comparison of the Poynting and power fluxes, $P_s(\psi)$ (3.40) and $P_e(\psi)$ (3.41), is good within 1.5%. This does not mean, however, that we have solved the problem with such an accuracy but merely that we did not make gross errors when programming. There remain errors due to the discretization which can be assessed by convergence studies. This is discussed in the next section.

3.5. Properties of the computational model

3.5.1. Preliminary remarks

It is nice to show a result of a numerical code. However, we may address the question of its credibility. In other words, we would like to know – and if possible to measure – to which extent we can be confident in the numerical solution. We have shown in the preceding part that the equations are solved exactly on a given finite number of mesh points. We now have to show what happens to the solution when the number of mesh points is increased, whether the results converge and how. This is done in section 3.5.2.

The other parameter which is still free is ν (see (3.8)). In section 3.5.3 we discuss how the solution behaves with respect to the value of ν and how this behaviour can be interpreted.

From a more physical point of view it is important to determine how the numerical code compares with other models and whether it is able to describe correctly the experiment. These points are discussed in section 3.5.4.

3.5.2. Convergence properties

We shall examine the convergence properties in three different cases. We consider first a single species plasma with no resonant layer inside. The frequency is such that $\omega/\omega_{ci} = 1.5$ on the magnetic axis. We introduce a rather strong damping: $\nu = 0.4$. The equilibrium is of the Solovev type, with an aspect ratio of 10, a circular cross section and a safety factor on axis of 1. The antenna is located both on the high and low field sides, with currents given by $\beta(\theta) = \cos\theta$ in eq. (3.22), and we consider only one toroidal Fourier component: $n = -4$. The problem is solved on various meshes. We define

$$N_{cell} = N_\psi N_{pol}, \qquad h^2 = 1/N_{cell}. \tag{3.52}$$

We let N_ψ and N_{pol} vary simultaneously with $N_\psi = 2N_{pol}$ and examine the numerical results as a function of h.

For non-Hermitian problems solved using finite elements of first order the theoretical convergence law of the solution is linear in h. In our case we have found a mixture of quadratic

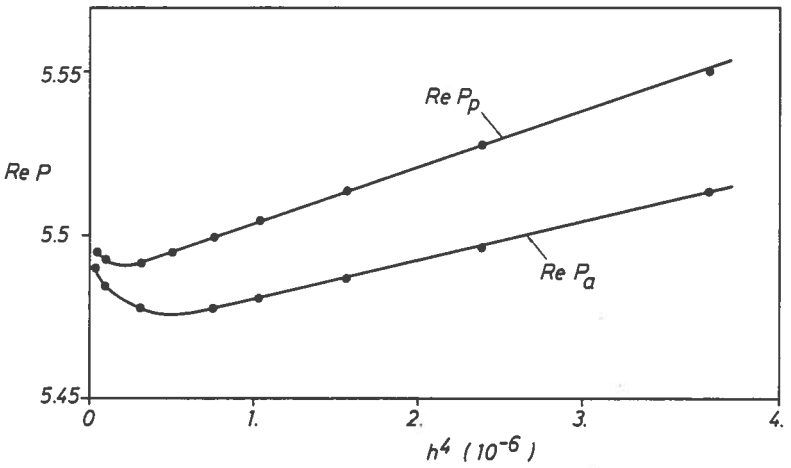

Fig. 14. Convergence study of the total resistive power versus $h^4 = 1/N_{\text{cell}}^2$ for a strong damping case with no resonance inside the plasma ($\omega/\omega_{ci} = 1.5$ on the magnetic axis, $\nu = 0.4$). P_a denotes the power delivered by the antenna (3.35) and P_p the power transmitted through the plasma surface (3.36) and (3.51).

and quartic dependencies. In fig. 14 the quantities Re P_a (3.35) and Re P_p (3.51) are plotted versus h^4. We see that the convergence is quartic, mixed with a small quadratic dependence which shows up only for very fine meshes. Let us write

$$\begin{aligned} \text{Re } P_p &= P_{p\infty} + f_p h^2 + g_p h^4 + \mathcal{O}(h^5), \\ \text{Re } P_a &= P_{a\infty} + f_a h^2 + g_a h^4 + \mathcal{O}(h^5). \end{aligned} \tag{3.53}$$

From fig. 14 we deduce $g_p = 17\,330$ and $g_a = 11\,500$. A plot of Re $P_p - g_p h^4$ and of Re $P_a - g_a h^4$ versus h^2 (not shown) yields the converged values $P_{p\infty} = 5.500 \pm 0.001$ and $P_{a\infty} = 5.500 \pm 0.001$. Notice that even for rather coarse meshes the result is within 1% of the converged value. In fig. 15 the power balance relation $(P_e(\psi) - P_s(\psi))/P_e(\psi)$ evaluated on the outermost cells is plotted versus h^2. A quadratic convergence is observed. We are very pleased to see that the converged value is zero and that even for coarse meshes the balance is satisfied with an accuracy of 0.02%. Other quantities such as the reactive power, the maximum value of the power absorption density, the Poynting vector or the electric field converge quadratically in h (not shown).

We now consider the same plasma as before but lower the excitation frequency so that $\omega/\omega_{ci} = 0.375$ on the magnetic axis. This is in the Alfvén wave heating domain. The antenna is helical: the currents are given by $\beta(\theta) = \exp(im\theta)$ in eq. (3.22), with $n = -6$ and $m = -1$. A small damping $\nu = 2 \times 10^{-2}$ is introduced. As shown in fig. 16a the quantity Re P_p converges in $\mathcal{O}(h^4)$. The quantity Re P_a still exhibits a mixture of quadratic and quartic convergences. In this sense Re P_p (see (3.51)) is a better evaluation of the resistive power than Re P_a (3.53). Nevertheless, both quantities differ only by 2% even for coarse meshes and they converge to the same value Re $P_{p\infty}$ = Re $P_{a\infty} = 3.107 \pm 0.001$. The reactive power inside the plasma shows the same behaviour (fig. 16b): Im P_p converges quartically to 8.515 ± 0.002 and Im P_a^{plasma} converges to the same value with a mixture of quadratic and quartic laws. The vacuum power Im P_a^{vacuum}

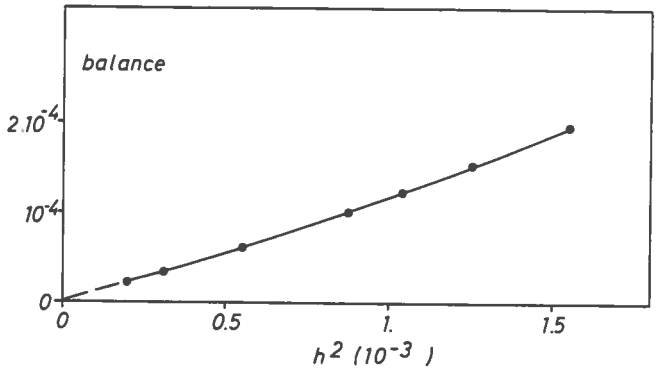

Fig. 15. Convergence study of the power balance $(P_e(\psi)-P_s(\psi))/P_e(\psi)$ versus $h^2=1/N_{cell}$ for the same case as in fig. 14.

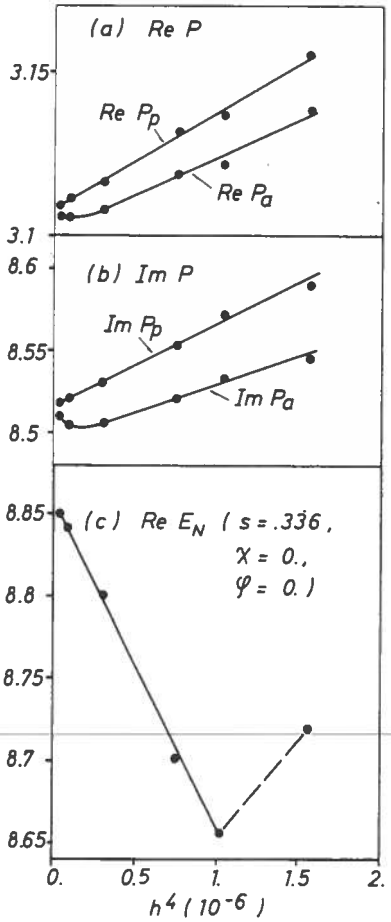

Fig. 16. Convergency study of (a) the total resistive power, (b) the reactive power inside the plasma and (c) the electric field at a given point versus h^4, for an Alfvén wave heating case ($\omega/\omega_{ci}=0.375$ on the magnetic axis, $\nu=2\times10^{-2}$).

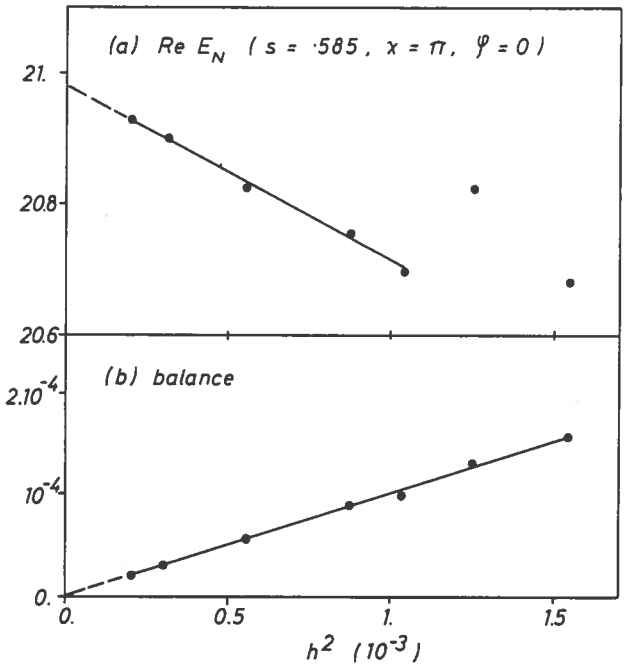

Fig. 17. Convergence study of (a) the electric field at a given point and (b) the power balance $(P_e(\psi)-P_s(\psi))/P_e(\psi)$ versus h^2, for the same case as in fig. 16.

converges quadratically to 1.936 ± 0.005. At certain points the value of the wave field converges quartically. An example is given in fig. 16c where Re E_N ($s = 0.336$, $\chi = 0$, $\phi = 0$) is plotted versus h^4. In general, however, it converges quadratically as shown in fig. 17a where Re E_N ($s = 0.585$, $\chi = \pi$, $= 0$) is plotted versus h^2. The power balance $(P_e(\psi) - P_s(\psi))/P_e(\psi)$ converges quadratically to zero (fig. 17b)). As in the previous case we have an accuracy of 0.02% even with rather coarse meshes.

In some cases the solution shows a complicated structure, so that the maximum mesh size available is insufficient to demonstrate the convergence properties of the numerical code. There is also the problem of the strong variation of ϵ_{NN} and $\epsilon_{N\perp}$ (3.5) around the line $\omega = \omega_{ci}$ specially if the concentration of the corresponding ion species is small. In such cases it is difficult to have enough spatial resolution for a good description of ϵ_{NN} and $\epsilon_{N\perp}$. Our choice of the coordinates ψ and χ is certainly not the best in this respect; however, since the solution often shows much structure in ψ our mesh will describe it advantageously. As an example we consider a large plasma (JET) containing a mixture of hydrogen (97.4%) and deuterium (2.6%). The equilibrium is of the Solovev type, with an aspect ratio of 3, an ellipticity of 1.3 and a safety factor on axis of 1.11. The magnetic field B_0 is 3.5 T and the density n_e is 4×10^{19} m^{-3}. The antenna is on the low field side. The antenna current, given by the function $\beta(\theta)$ in eq. (3.22), has been chosen to be constant and purely poloidal. The frequency, 27.2 MHz, is such that the cyclotron frequency of deuterium is matched at the centre of the plasma column. A small damping ($\nu = 2.5 \times 10^{-3}$) is introduced. The solution is shown in fig. 18 where the contour lines of the circular left polarization, $|E_+| = |E_N + iE_\perp|$, are plotted. Notice the importance of the magnetic structure.

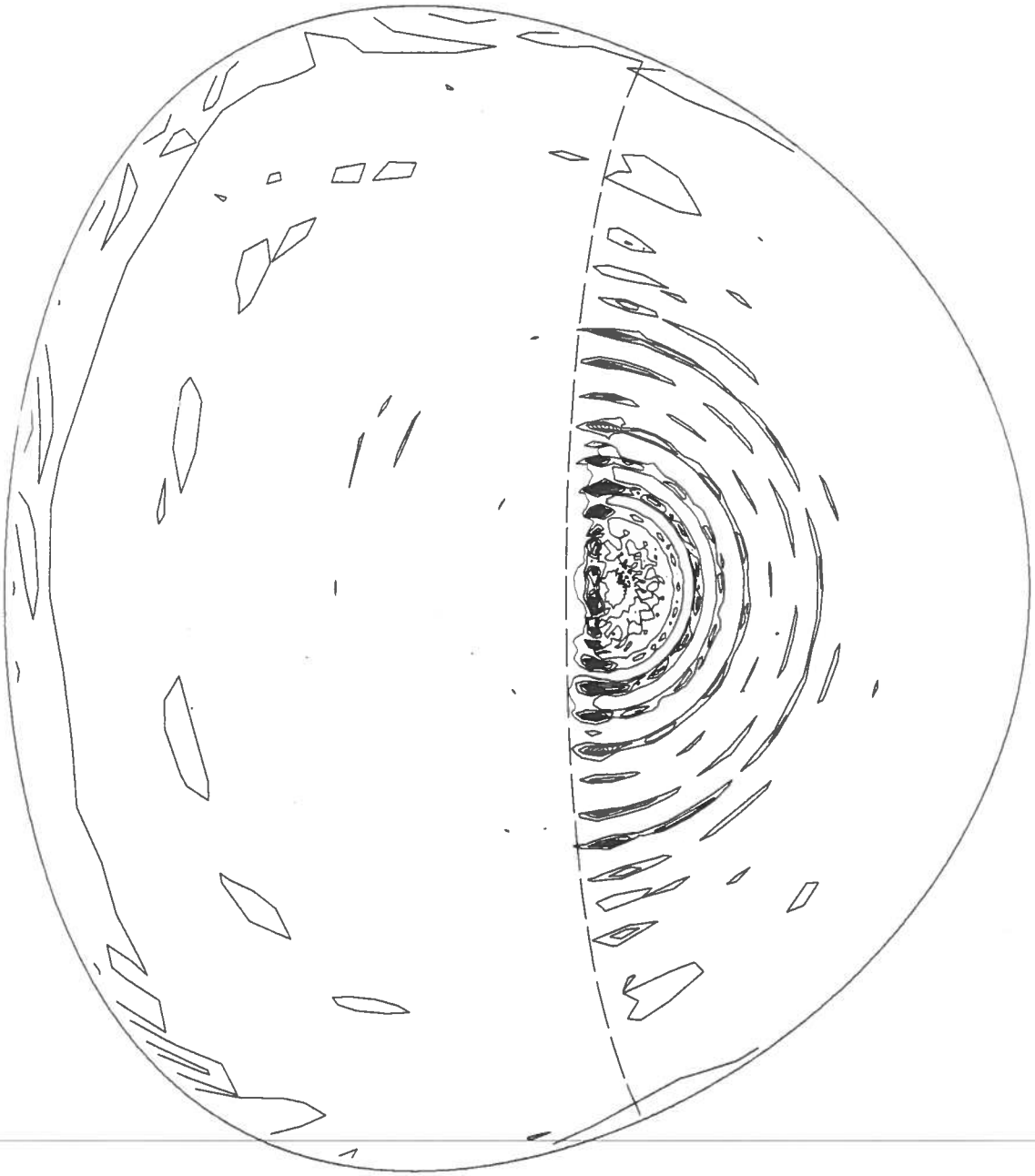

Fig. 18. Contour lines of the circular left-hand polarization of the electric field, $|E_+| = |E_N + iE_\perp|$, for a mode conversion scenario in JET in a hydrogen plasma with 2.6% deuterium. The parameters are: $n_e = 4\times10^{19}$ m^{-3}, $B_0 = 3.5$ T, $R_0 = 3$ m, aspect ratio = 3, frequency = 27.2 MHz, low field side antenna, $n = 3$, $\nu = 2.5\times10^{-3}$. The dashed line indicates $\omega = \omega_{CD}$.

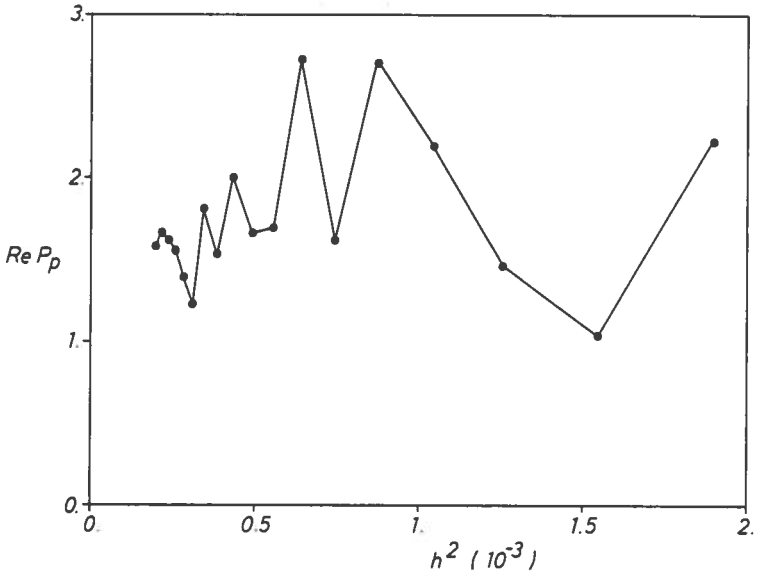

Fig. 19. Convergence study of the total resistive power versus h^2 for the same case as in fig. 18. For the maximum mesh size used ($N_\psi = 100$, $N_{pol} = 50$) the convergence is not reached.

The power absorption occurs predominantly on the intersections of the resonant ψ-surfaces with the line $\epsilon_{NN} - n^2/r^2 = 0$ which is the resonance in the WKB approximation (not shown). The mesh used in the calculation is $N_\psi = 100$ and $N_{pol} = 50$ and, as we shall see, is not sufficient to get close to convergence. In fig. 19 the quantity Re P_p is plotted versus various mesh sizes. Large oscillations occur with an amplitude which decreases with the number of mesh cells. We cannot state an accuracy of better than 30%. Therefore we have to be careful in presenting numerical results such as fig. 18: they can give a good insight into what happens physically but cannot be regarded as the final (converged) result. An indication that the solution shown may be not so bad is given by the power balance relations. The comparison between the quantities P_a (3.35) and P_p (3.51) gives Re P_a = Re P_p with an accuracy of 0.6%. The agreement between the Poynting and power fluxes, $P_s(\psi)$ (3.40) and $P_p(\psi)$ (3.41), is within 0.5% on the outermost cells and better than 2% elsewhere. However, this does not mean that the solution is so close to the converged result. Satisfying a power balance relation is not sufficient to validate a solution. Let us consider for example the mesh $N_\psi = 48$, $N_{pol} = 24$. We have Re P_a = Re P_p within 1% and $P_s(\psi) = P_e(\psi)$ within 3% on the outermost cells. But the solution is manifestly not correct with such an accuracy (see fig. 19)!

It can be a fastidious task to make such convergence studies for each case. A possibility of getting an idea of the accuracy of a result is to vary the distribution of the mesh cells and look how the different quantities depend on this variation. In cases like in fig. 18 the number of resonant magnetic surfaces is so large that the number of cells is not sufficient to describe all of them. By changing the distribution of the mesh cells, new resonances may show up while others may vanish. This can give an idea of the size of the mesh required for convergence.

The results of the above convergence studies can be summarized as follows: either the mesh is insufficient due to the intrinsic complexity of the solution and no convergence law can be

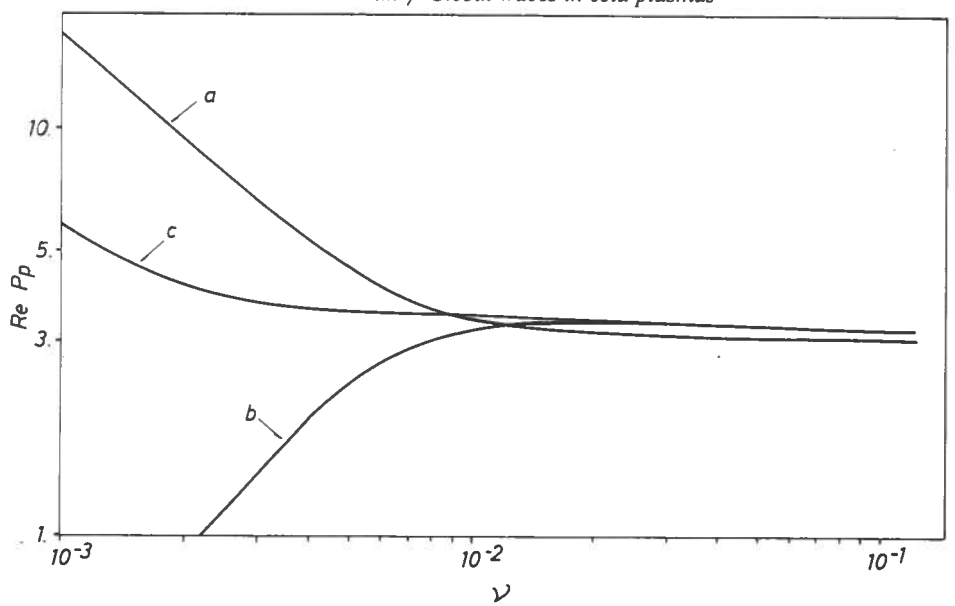

Fig. 20. Behaviour of the total resistive power with respect to ν for the resonance absorption case. The frequency used for the curves (b) and (c) is slightly different from that used for the curve (a). For the curve (c) the mesh points are accumulated around the main resonant surface.

evidenced, or the mesh is fine enough and a convergence or even super-convergence is observed, leading to very accurate results. No mathematical explanation of this super-convergence has been found as yet.

3.5.3. Behaviour with respect to ν

Four different types of behaviour of the solution with respect to ν may occur. They can be related to four different physical situations: excitation of a global mode, resonance absorption, both these phenomena occur simultaneously, none of them occurs.

In the case of a pure global mode, the role of ν is the same as that of the electric resistance in an LCR circuit: the power absorption is inversely proportional to ν. If we trace the power as a function of the frequency, a global mode will show up as a peak whose width is proportional to ν and height inversely proportional to ν. The structure of the power deposition is global and does not depend on ν. This is not the case when a resonant surface is present inside the plasma.

In the case of resonance absorption, the role of ν (eq. (3.8)) is to turn around the singularities. The power is then independent of ν for sufficiently small ν. For a given mesh, however, there is a minimum value of ν below which the effects of the discretization show up. We have to remember that resonance absorption means the excitation of a mode belonging to a continuum, and that this continuum is numerically represented by a finite set of modes (see fig. 3). The value of ν must be such that at least two discretized modes are simultaneously excited. To illustrate this important feature we consider an Alfvén wave heating scenario with the same parameters as in fig. 14. We solve the problem on a mesh with $N_\psi = 40$ and $N_{\mathrm{pol}} = 20$. The curve (a) in fig. 20 shows the total resistive power Re P_p as a function of ν. We see that Re P_p is independent of ν for values down to $\nu_{\mathrm{lim}} = 10^{-2}$. Below this value the power varies as $1/\nu$, but this does not mean

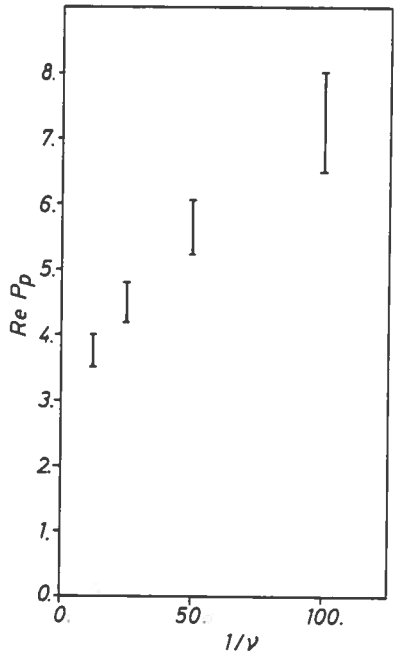

Fig. 21. Behaviour of the total resistive power with respect to ν for the case of simultaneous excitation of a continuum and of a global mode. The parameters are the same as in fig. 11 except the frequency = 32.1 MHz.

that a global mode is excited. It merely means that the frequency is equal to the frequency of one of the discretized modes of the continuum; below ν_{lim} we excite only this one. The mode is not physical since it depends on the mesh. Therefore one has to be careful before identifying every feature which varies proportionally to $1/\nu$ as a global mode! By varying the mesh it is nevertheless possible to eliminate the ambiguity. An example is shown in fig. 20 where the curves (b) and (c) represent the total resistive power, Re P_{p}, corresponding to the same case but solved on different meshes. A mesh with $N_\psi = 40$ and $N_{\text{pol}} = 20$ is used; for the curve (c) we accumulate the mesh points around the main resonant surface. For the curve (b) the excitation frequency is situated between two discretized frequencies, so that below $\nu_{\text{lim}} = 10^{-2}$ the power drops proportionally to ν. For the curve (c) we excite a discretized mode (as for curve (a)) but the mesh accumulation allows us to lower ν_{lim} down to 3×10^{-3}.

In the case of the excitation of a global mode in the presence of resonance absorption, ν plays both roles described above. This situation is delicate since we have to be sure that the mode observed is physical and not due to the discretization. The presence of a global mode inside a continuum enhances the power absorption. Let us consider a mode conversion scenario in JET with the same parameters as in fig. 11: a minority of helium-3 in a deuterium plasma. We only change slightly the frequency (32.1 MHz instead of 35 MHz). The total resistive power Re P_{p} as a function of $1/\nu$ is plotted in fig. 21. The error bars are due to the lack of mesh resolution ($N_\psi = 100$, $N_{\text{pol}} = 50$). Therefore we must consider this result as preliminary. For ν down to 10^{-2} we have

$$\text{Re } P_{\text{p}} = P_{\text{cont}} + P_{\text{global}}/\nu. \tag{3.54}$$

For values of ν smaller than 10^{-2} we deviate from this dependency because we start to lose the contribution from resonance absorption. It is therefore not possible to know whether or not, for smaller values of ν, the power is independent of ν (which means that the power due to the presence of the global mode is also resonantly absorbed). The indication of the presence of a global mode when a continuum is also excited is delicate and needs still further investigations. For example, we can calculate the power as a function of the frequency (or the plasma density). A global mode manifests itself as a peak. The width of the peak is proportional to ν and its height above the continuum is inversely proportional to ν, as (3.54) suggests. This kind of study has been applied to the tokamak TCA where such peaks superposed on a continuum have been found experimentally [34]. This point is discussed in the next section.

In the case where neither a global mode is excited nor resonance absorption occurs, the only absorption arises from the damping ν so that the total power is just proportional to ν.

3.5.4. Comparison with other models and with experiment

A very important check of the validity of the numerical scheme is to examine its ability to reproduce the results of other models. We mention here two limiting cases: the cylindrical limit with finite ω/ω_{ci} and the ideal MHD limit ($\omega/\omega_{ci} = 0$) with finite aspect ratio.

For homogeneous plasmas in cylindrical geometry an analytic dispersion relation can be derived, giving the eigenmodes of the fast magnetosonic wave and of the Alfvén wave. A study of the spectrum of these modes for the case $m = \pm 1$ can be found in ref. [20]. On using the LION code in this large aspect ratio limit we have found the same spectrum as the analytical one.

In the ideal MHD in toroidal geometry we compare the results of our numerical scheme with those of the ERATO code in its version used for the study of Alfvén wave heating [9]. Since our model does not include finite β effects but ERATO does, both calculations yield the same results with a discrepancy of the order of β.

These two checks demonstrate the ability of the LION code to treat both the physics related to finite ω/ω_{ci} and the toroidal geometry.

The final criterion of the validity of a theoretical model is the comparison with experiment. The studies of Alfvén wave heating in the TCA tokamak provide us with a possibility to perform such a check, and even to show a case where the combined effects of the finite ω/ω_{ci} and toroidal geometry are necessary to explain the phenomenon. The experiments have shown the existence of modes, both global Alfvén and subsequent continuum, in a region of the spectrum where none was expected from a cylindrical model. The interpretation of this fact is the toroidal coupling from the antenna excitation structure (here $n = 2$, $m = 1$) to the mode ($n = 2$, $m = 0$). The ideal MHD toroidal model (ERATO) was able to show the existence of the continuum, while the global mode was still absent in the calculations. With our present model which includes also the effects of finite ion cyclotron frequency (here $\omega/\omega_{ci} = 0.22$) we have found a global mode at the same place in the spectrum as the experiment [21].

4. Limitations and further improvements of global wave codes

The essential limitation of global wave codes is the maximum mesh size which can be treated due to the large memory storage, input/output operations and central processor time required.

We have seen that in some cases this maximum is insufficient to allow us to demonstrate convergence. Therefore we have to develop new algorithms having a better efficiency.

In the LION code the full blocks of the matrix **A** are stored though they are sparse (fig. 9). This is due to the fact that the decomposition of **A** into **LDU** fills the blocks. There is clearly a need to overcome this handicap. A possibility is to take advantage of the particular structure of the matrix **A**: the blocks overlap only for the variable X (see fig. 9). This arises from the fact that V has no derivative in the ψ direction and from the choice of the finite hybrid elements of first order. The variable V appears therefore as "one-dimensional". It is then possible to eliminate it, so that the only subblocks of the matrix **A** which must still be stored as full matrices are the overlaps ($\mathbf{A}_1$ in fig. 9). All the others can be stored as band matrices. The **LDU** decomposition is only applied to the subblocks $\mathbf{A}_1$ and $\mathbf{A}_5$. All the other operations are resolutions of linear triangular or banded systems of equations. This technique has been successfully applied to the ERATO stability code [35]. It led to a gain in CPU time and memory storage of the order of 4 and to a gain in disk storage and input/output operations of the order of 10, thus reducing dramatically the turn-around time. For the LION code the expected gains are comparable.

Another class of algorithms, the iterative methods, keep the sparseness of the matrix **A** untouched. These algorithms are easily vectorizable. Unfortunately, in our case **A** is neither symmetric nor positive definite. When applying a Gauss–Seidel scheme to our problem, the solution diverges after 4 or 5 iteration steps even on a mesh as small as 4×4! A possibility is to solve

$$\mathbf{A}^{\mathrm{T}}\mathbf{A}x = \mathbf{A}^{\mathrm{T}}b \tag{4.1}$$

instead of $\mathbf{A}x = b$(3.51). The matrix $\mathbf{A}^{\mathrm{T}}\mathbf{A}$ is symmetric and positive definite but its condition, defined as the ratio of the largest to the smallest eigenvalue, is usually very bad. A very promising scheme is the "incomplete Cholesky-conjugate gradient" method (ICCG) [36] in which incomplete **LDU** decomposition of the matrix is performed, thus retaining its sparseness and greatly accelerating the conjugate gradient iteration.

An alternative to the finite element and finite difference schemes is to expand the fields in Fourier series in the poloidal direction [37]. Unlike the toroidal decomposition, the poloidal Fourier components are not independent from each other. Practically, one has to truncate the series to a finite number of terms. Whether or not such a method is competitive depends on the rapidity of convergence with respect to the number of terms in the Fourier series.

In this paper we discussed the toroidal geometry in particular. It is clear that the numerical methods presented here are not restricted to this geometry but in principle can be applied to other two-dimensional configurations such as axisymmetric mirrors [38,39] or straight stellerators [32,40], for example.

We have restricted ourselves to the cold plasma model. There remains the question of introducing more physics into the numerics. For example, without touching the differential structure of the equations we can model the collisional or ion-cyclotron damping of the fast wave. However, as soon as more effects of finite temperature are taken into account, the differential structure of the equations is altered and thus the code needs more profound modifications. First of all, one would have to derive the pertinent equation in two-dimensional geometry, a task which is not easy at all. Moreover, since we met spatial resolution problems

already with the cold plasma model, one can expect these problems to be even tougher when "kinetic" short-wavelength waves are present. For more details concerning the global wave solution in warm plasmas see refs. [22,41].

5. Conclusion

In this paper we have presented and discussed some of the methods which are used for the numerical determination of the global solution in cold plasmas. We hope we have demonstrated that the global wave codes can be a powerful and reliable tool for the study of rf wave heating. A great advantage of these methods is that the accuracy of the results can be checked and measured by doing convergence studies.

As an example we have shown in detail the numerical code LION which solves the pertinent partial differential equations in exact toroidal geometry using a finite element method. The model is valid for any aspect ratio and any shape of plasma cross section. It provides a description of both the Alfvén and ion–ion hybrid resonances. Its compatibility with the ideal MHD and with an analytic dispersion relation for homogeneous plasma cylinder has been checked. By means of this code we were able to find global modes and to study the toroidal coupling. A successful comparison with the experiment in the TCA tokamak has been made in this context.

The work on global wave codes is still in progress. The efficiency of the methods needs to be improved by adapting modern and if possible vectorizable algorithms to our particular problem in order to increase the maximum mesh size available.

Acknowledgements

The authors wish to thank Drs. T. Hellsten and M. Brambilla for stimulating discussions. This work has been performed under JET article 14 contract No. JT4/9007 and was partly supported by the Swiss National Science Foundation.

References

[1] K.G. Budden, Radio Waves in the Ionosphere (Cambridge University Press, London, 1961).
[2] V.L. Ginzburg, Propagation of Electromagnetic Waves in Plasma (Gordon and Breach, New York, 1961).
[3] T.H. Stix, The Theory of Plasma Waves (McGraw-Hill, New York, 1962).
[4] F.W. Perkins, IEEE Trans. Plasma Science PS-12 (1984) 53.
[5] N.F. Cramer and I.J. Donnelly, Plasma Phys. Contr. Fusion 26 (1984) 1285.
[6] K. Itoh, S.I. Itoh and A. Fukuyama, Nucl. Fusion 24 (1984) 13.
[7] T. Hellsten and E. Tennfors, Physica Scripta 30 (1984) 341.
[8] D.L. Grekov, K.N. Stepanov and J.A. Tataronis, Sov. J. Plasma Phys. 7 (1981) 411.
[9] K. Appert, B. Balet, R. Gruber, F. Troyon, T. Tsunematsu and J. Vaclavik, Nucl. Fusion 22 (1982) 903.
[10] K. Appert, J. Vaclavik and L. Villard, Lecture Notes: An Introduction to the Theory of Alfvén Wave Heating, Lausanne Report LRP 238 (1984) CRPP, Lausanne, Switzerland.
[11] P.L. Colestock, IEEE Trans. Plasma Science, PS-12 (1984) 64.

[12] R. Behn et al., Plasma Phys. Contr. Fusion 26 No 1A (1984) 173.
[13] M. Brambilla, Comput. Phys. Rep. 4 (1986) 71.
[14] V.P. Bhatnagar, R. Koch, P. Geilfus, R. Kirkpatrick and R.R. Weynants, Nucl. Fusion 24 (1984) 955.
[15] M. Brambilla and A. Cardinali, Plasma Phys. 24 (1982) 1187.
[16] D.J. Gambier and D.G. Swanson, Phys. Fluids 28 (1985) 145.
[17] K. Appert, R. Gruber, F. Troyon and J. Vaclavik, Plasma Phys. 24 (1982) 1147.
[18] G. Strang and G.J. Fix, An Analysis of the Finite Element Method (Prentice-Hall, Engelwood Cliffs, 1973).
[19] R. Gruber and J. Rappaz, Finite Element Methods in Linear Ideal Magnetohydrodynamics (Springer-Verlag, Berlin, Heidelberg, 1985).
[20] K. Appert, J. Vaclavik and L. Villard, Phys. Fluids 27 (1984) 432.
[21] K. Appert et al., Phys. Rev. Lett. 54 (1985) 1671.
[22] K. Appert, T. Hellsten, J. Vaclavik and L. Villard, Comput. Phys. Commun. 40 (1986) 73.
[23] F. Hofmann, K. Appert and L. Villard, Nucl. Fusion 24 (1984) 1679.
[24] K. Appert, B. Balet, R. Gruber, F. Troyon and J. Vaclavik, Comput. Phys. Commun. 24 (1981) 329.
[25] R. Gruber, J. Comput. Phys. 26 (1978) 379.
[26] K. Itoh, A. Fukuyama and S.I. Itoh, Comput. Phys. Commun. 32 (1984) 35.
[27] P.L. Colestock and R.F. Kluge, Bull. Amer. Phys. Soc. 27 (1982) 8.
[28] K. Appert, B. Balet, R. Gruber, F. Troyon, T. Tsunematsu and J. Vaclavik, Proc. of the 2nd Joint Grenoble–Varenna Intern Symposium, Como, Italy (1980) 643.
[29] R. Gruber et al., Comput. Phys. Commun. 21 (1981) 323.
[30] K. Appert, G. Collins, T. Hellsten, J. Vaclavik and L. Villard, Proc. of the 12th EPS Conference on Contr. Fusion and Plasma Phys., Budapest (1985).
[31] K. Appert, B. Balet and J. Vaclavik, Phys. Lett. 87A (1982) 233.
[32] R. Gruber et al., Comput. Phys. Commun. 24 (1981) 363.
[33] L.S. Solovev, JETP 26 (1968) 400.
[34] A. de Chambrier et al., Plasma Phys. 24 (1982) 893.
[35] D.S. Scott and R. Gruber, Comput. Phys. Commun. 23 (1981) 115.
[36] D.S. Kershaw, J. Comput. Phys. 26 (1978) 43.
[37] P.L. Colestock, private communication (1985).
[38] A. Goto, A. Fukuyama and Y. Furutani, Proc. of the 12th EPS Conference on Contr. Fus. and Plasma Phys., Budapest (1985).
[39] M.W. Phillips and A.M.M. Todd, Comput. Phys. Commun. 40 (1986) 65.
[40] A. Fukuyama, N. Okazaki, A. Goto, S.I. Itoh and K. Itoh, Proc. of the 12th EPS Conference on Contr. Fus. and Plasma Phys., Budapest (1985).
[41] A. Fukuyama, K. Itoh and S.-I. Itoh, Comput. Phys. Rep. 4 (1986) 137.

APPENDIX II :

User Manual : Description of Input, Output and Plot.

Index of Subprogrammes and Common Variables

TECHNICAL INFORMATION ABOUT

```
**********************
*                    *
*    L I O N - 8 6   *
*                    *
**********************
```

2-D GLOBAL WAVE CODE FOR ALFVEN AND ICRF

WRITTEN BY

L. VILLARD, K. APPERT AND R. GRUBER

CRPP-EPFL
AV. DES BAINS 21
CH-1007 LAUSANNE
SWITZERLAND

FIRST VERSION FOR JET
CONTRACT ARTICLE 14 NO. JT4/9007

VERSION 10 LDV MARCH 1986 CRPP LAUSANNE

****
********** USER MANUAL **********
****

REFERENCES :

(1) L.VILLARD, K.APPERT, R.GRUBER AND J.VACLAVIK, 'GLOBAL WAVES IN COLD PLASMAS',LAUSANNE REPORT LRP 275/85 (1985) CRPP, LAUSANNE, SWITZERLAND. COMPUT. PHYS. REPORTS 4 (1986) 95.

(2) R.GRUBER ET AL., COMPUT. PHYS. COMMUN. 24 (1981) 323.

(3) K.APPERT ET AL., NUCL.FUS. 22 (1982) 903.

COMPLEMENTARY INFORMATION ABOUT INPUT VARIABLES

---

1. PLASMA PHYSICS

THE EQUILIBRIUM CAN BE GIVEN IN TWO DIFFERENT WAYS, DEPENDING

ON THE VALUE OF 'NTCASE'.

NTCASE = 2 ====> SOLOVEV EQUILIBRIUM, DEFINED BY THE VARIABLES :

'ASPCT' (INVERSE ASPECT RATIO)
'B2R2' (B2)
'ELLIPT'(ELLIPTICITY SQUARED)
'QIAXE' (1/Q(AXIS))

SEE REF.(2), EQS (2.7) (2.8).

NTCASE = 3 ====> NUMERICAL EQUILIBRIUM, OBTAINED FROM AN OTHER CODE. THE VALUES OF PSI ON A (R,Z) MESH ARE READ FROM A FILE 'DORY' (TAPE NR. 'NDORY', DEFAULT SETTING 'TAPE11'). IT IS CRUCIAL TO NOTE HOW THE TRANSFER OF DATA TAKES PLACE (SEE P1C3S02.34,36). IN PARTICULAR THE NUMBER OF MESH POINTS IN THE R AND Z DIRECTIONS MUST CORRESPOND TO THE ONES IN THE EQUILIBRIUM CODE + 1. THIS EQUILIBRIUM CAN BE SCALED BY USING THE PARAMETER 'SCALE' . DIFFERENT VALUES OF 'SCALE' WILL DEFINE DIFFERENT EQUILIBRIA. SEE REF.(2), EQ.(6.13).

NOTE THAT BY RUNNING LION1 WITH NLOTP1(1)=.TRUE., ONE OBTAINS INFORMATION ABOUT THE EQUILIBRIUM PROFILES. (Q,T,ETC.)

THE LOGICAL VARIABLE 'NLCOLD' SELECTS EITHER THE COLD OR LUKEWARM PLASMA MODEL. LUKEWARM MODEL INCLUDES CYCLOTRON DAMPING OF THE FAST WAVE BUT NOT THE ION BERNSTEIN WAVE, IN OTHER WORDS INCLUDES THE PARALLEL TEMPERATURE BUT NOT THE PERPENDICULAR. THE USER MUST BE AWARE THAT THIS MODEL CANNOT PREDICT WHICH FRACTION OF THE POWER IS DEPOSITED ON IONS.

'NRSPEC' IS THE NUMBER OF ION SPECIES. WE GIVE THEIR NUMBER DENSITIES ON MAGNETIC AXIS ('CENDEN()',M**-3) AND TEMPERATURES ('CENTI()', EV, DISCARDED IF NLCOLD=.TRUE.). THE VARIABLES 'EQDENS' AND 'EQKAPD' SPECIFY THE DENSITY PROFILE ACCORDING TO:

N-SUB-I = CENDEN(I) * (1.-EQDENS*S*S) **EQKAPD .

(SUBROUTINE DENSIT, 1.2.34).

IT IS ALSO POSSIBLE TO DEFINE RADIAL PROFILES OF THE MINORITY CONCENTRATIONS WITH 'FRCEN' (RADIAL POSITIONS OF THE CENTERS OF THE DISTRIBUTIONS, NORMALIZED TO THE MINOR RADIUS) AND 'FRDEL' (WIDTH OF THE DISTRIBUTIONS). THESE PROFILES HAVE NOT BEEN PROGRAMMED YET. SEE SUBROUTINES 'FRPROF' (3.2.15) AND 'SHAPE' (3.2.16).

THE TEMPERATURE PROFILES ARE GIVEN BY 'EQTI()' AND 'EQKAPT()' ACCORDING TO :

T-SUB-I = CENTI(I) * (1.-EQTI(I)*S*S) **EQKAPT(I)

(SUBROUTINE TEMPI, 3.2.18)

THE ION SPECIES ARE DEFINED BY THEIR ATOMIC CHARGE NUMBERS 'ACHARG()', AND ATOMIC MASS NUMBERS 'AMASS()'.

WE SPECIFY ALSO THE MAGNETIC FIELD ON MAGNETIC AXIS ('BNOT',TESLA) THE MAJOR RADIUS ('RMAJOR',M) AND THE WAVE CAUSAL DAMPING ('ANU'). NOTE THAT 'ANU' IS DIMENSIONLESS AND CORRESPONDS TO NU IN EQ.(3.8) OF REF.(1).

2. ANTENNA AND SHELL

THE VARIABLE 'NANTYP' SELECTS THE TYPE OF ANTENNA.

NANTYP = 1 ====> HELICAL ANTENNA. CURRENT SHEET AT A CONSTANT DISTANCE OF THE PLASMA SURFACE. THE CURRENTS ARE HARMONIC FUNCTIONS OF THE POLOIDAL ANGLE THETA, WITH A POLOIDAL WAVENUMBER GIVEN BY 'MPOLWN()':

BETA(THETA) = SUM(J=1 TO MANCMP) OF
CURSYM(J)*COS(MPOLWN(J)*THETA) +
I*CURASY(J)*SIN(MPOLWN(J)*THETA).

THERE ARE NO FEEDERS.

NANTYP = 2 ====> LFS OR HFS ANTENNA. CURRENT SHEET WHICH, BETWEEN THETA = ANTUP AND -ANTUP, IS AT A CONSTANT DISTANCE OF THE PLASMA SURFACE AND CARRIES CONSTANT PURE POLOIDAL CURRENTS :

BETA(THETA) = CURSYM(1)

BETWEEN THETA = ANTUP AND THETA = FEEDUP ARE THE FEEDERS, WHERE THE DISTANCE FROM THE PLASMA SURFACE INCREASES SMOOTHLY.
THE SELECTION OF EITHER LFS OR HFS ANTENNA AUTOMATIC :

ANTUP.LT.FEEDUP SELECTS LFS
ANTUP.GT.FEEDUP SELECTS HFS

IT IS NOT POSSIBLE TO HAVE ANTUP=FEEDUP.
THE ANGLES 'ANTUP' AND 'FEEDUP' ARE MEASURED IN DEGREES ABOVE THE EQUATORIAL PLANE FROM THE MAGNETIC AXIS.

'NLDIP' SELECTS MONOPOLE OR DIPOLE ANTENNA. THE DIPOLE OPTION HAS NOT BEEN PROGRAMMED YET.

'ANTRAD' AND 'REXT' SPECIFY THE DISTANCES OF ANTENNA AND SHELL FROM MAGNETIC AXIS IN UNITS OF THE MINOR RADIUS IN THE Z=0 PLANE.

'FREQCY' IS THE GENERATOR FREQUENCY IN HZ.

'WNTORE' IS THE TOROIDAL WAVE NUMBER.

3. OUTPUT AND PLOT

ALL OUTPUT IS IN CODE-NORMALIZED UNITS UNLESS SPECIFIED.

'NLOTP0' : GENERAL SWITCH FOR LINE-PRINTER OUTPUT AND GRAPHICS.

'NLOTP1()' : LINE-PRINTER OUTPUT FOR LION1.
(1) : (S,CHI) MESH AND EQUILIBRIUM PROFILES.
(2) : CYLINDRICAL MHD-ALFVEN FREQUENCIES.
(3) :
(4) :
(5) :

'NLOTP2()' : LINE-PRINTER OUTPUT FOR LION2.
(1) : QUANTITIES AT PLASMA SURFACE
(2) : POSITION OF PLASMA SURFACE, ANTENNA AND SHELL.
(3) : ANTENNA CURRENT.
(4) :
(5) :

'NLOTP3()' : LINE-PRINTER OUTPUT FOR LION3.
(1) :
(2) :

'NLOTP4()' : LINE-PRINTER OUTPUT FOR LION4.
(1) : NAMELIST
(2) : OHM-VECTOR
(3) : SOLUTION AT PLASMA BOUNDARY
(4) :

(5) :
THE TOTAL POWER IS PERMANENT OUTPUT.

'NLOTP5()' : LINE-PRINTER OUTPUT FOR LION5.
(1) : NAMELIST
(2) : RADIAL POWER ABSORPTION
(3) : POLOIDAL POWER ABSORPTION
(4) : 2-D POWER ABSORPTION DENSITY
(5) : 2-D POWER ABSORBED IN EACH CELL
(6) : 2-D NORMAL COMPONENT OF POYNTING
(7) : 2-D PERP COMPONENT OF POYNTING
(8) : 2-D PARALLEL COMPONENT OF POYNTING
(9) :
(10) : 2-D REAL PART OF E-NORMAL
(11) : 2-D REAL PART OF E-PERP
(12) : 2-D IMAGINARY PART OF E-NORMAL
(13) : 2-D IMAGINARY PART OF E-PERP
(14) : 2-D POLARAZATION NORM OF E-PLUS SQUARED
(15) : 2-D POLARIZATION NORM OF E-MINUS SQUARED

```
        (16) :
        (17) :
        (18) :
        (19) :
        (20) : NORM OF POLOIDAL FOURIER COMPONENTS OF E-NORMAL
        (21) :                 #                        E-PERP
        (22) : 2-D EPSILON SUB-N-N - N**2 / R**2
        (23) : 2-D IMAGINARY PART OF EPSILON SUB N-N
        (24) : 2-D OMEGA - OMEGACI
        (25) :
```

THE 2-D TABLES GIVE THE VALUES ON THE CENTERS OF THE CELLS OF THE (S,CHI) MESH. A LINE IN THE TABLE CORRESPONDS TO A PSI = CONST SURFACE. IT GOES FROM CHI=0 TO CHI=PI IN THE UPPER HALF-PLANE AND FROM CHI=PI TO CHI=2*PI IN THE LOWER HALF-PLANE. THE VALUES ARE NORMALIZED TO THEIR MAXIMUM VALUE. THE FIRST AND THE LAST LINES OF THE TABLES GIVE THE POLOIDAL NUMBERING OF THE CELLS. THE FIRST COLUMN GIVES THE RADIAL NUMBERING OF THE CELLS.

```
'NLPL05()' : GRAPHICAL OUTPUT FOR LION5
        (1) : GENERAL SWITCH FOR GRAPHICAL PLOTS
        (2) : RADIAL POWER ABSORPTION AND FLUX
        (3) : POLOIDAL POWER ABSORPTION
        (4) : 2-D CONTOURS OF POWER ABSORPTION DENSITY
        (5) : 2-D SYMBOLIC OF POWER ABSORBED IN EACH CELL
        (6) : 2-D ARROWS OF POYNTING VECTOR (NORMAL,PERP)
        (7) : 2-D ARROWS OF REAL (E-NORMAL,E-PERP) AT VARIOUS
              TOROIDAL ANGLES ('ANGLE(J)' J=1 TO 'NFIG')
        (8) : 2-D CONTOURS OF NORM OF E-PLUS
        (9) :
       (10) :
       (11) : 2-D CONTOURS OF POYNTING VECTOR (PARALLEL)
       (12) : 2-D LINE EPSILON SUB (N,N) - N**2/R**2 = 0
       (13) : 2-D CONTOURS OF IMAGINARY PART OF EPSILON (N,N)
       (14) : 2-D LINE(S) OMEGA=OMEGACI
       (15) TO (25) : FREE
```

THE DIMENSION OF THE 2-D PLOTS IS SPECIFIED BY 'ALARG' AND 'AHEIGT'. THE NUMBER OF CONTOUR LINES IS GIVEN BY 'NCONTR'. THE ARROWS HAVE A SIZE NORMALIZED TO THEIR MAXIMUM VALUE. THIS SIZE IS CONTROLLED BY THE VARIABLE 'ARSIZE'.

INDEX OF SUBPROGRAMS

VERSION 10 LDV MARCH 1986 CRPP LAUSANNE

********** LION1 **********

DATA	DEFINE DATA SPECIFIC TO RUN	1.1.04
AUXVAL	SET AUXILIARY VALUES	1.1.05
STEPON	STEP ON CALCULATION	1.2.01
FORMEQ	ORGANIZE EQUILIBRIUM CALCULATIONS	1.2.02
MESH(1)	SET UP PSI-CHI MESH	1.2.03
KERTP	PREPARES NTCASE=1	1.2.04
KERTES	PREPARES NTCASE=2	1.2.05
SCALES	SCALES NUMERICAL EQUILIBRIUM	1.2.06
FITAXE	FITS EQUILIBRIUM AROUND AXIS	1.2.07
NOREPT	NORMALIZES TO ERATO STANDARD	1.2.08
TANDP	SETS T , P AND RHO	1.2.09
SELECT(1)	SELECTS ANALYTICAL OR NUMERICAL EQUILIBRIUM	1.2.10
ISTPSI(2)	RADIAL COUNTER AT Z=0	1.2.11
EQANAL(1)	ANALYTIC SOLOVEV EQUILIBRIUM	1.2.12
ALPHA(2)	CALCULATES Q AND NON ORTHOGONALITY	1.2.13
PSRHO(5)	GIVES R,Z(PSI)	1.2.14
PSIRZ(2)	PSI(R,Z) BY FIT	1.2.15
DERIVE(2)	DERIVATIVES OF PSI(R,Z)	1.2.16
INTFAC(1)	INTERFACE NUMERICAL EQUILIBRIUM - ERATO	1.2.17
ADVANC(5)	ADVANCES ON PSI=CONSTANT LINE	1.2.18
INTPOL(5)	INTERPOLATES ON CHI=CONSTANT	1.2.19
NUMEQU(1)	NUMERICAL EQUILIBRIUM	1.2.20
SURFIT	ORGANIZES NTCASE=4	1.2.21
FITSUR(3)	FITS PLASMA SURFACE	1.2.22
TRIBAC(6)	SOLVES SYSTEM OF LINEAR EQUATIONS	1.2.23
MERCIR	MERCIER CRITERION	1.2.24
BALOON	BALLOONING MODE CRITERION	1.2.25
ALDLT(5)	DECOMPOSES A=LDLT	1.2.26
BETAST(1)	CALCULATES BETA VALUES	1.2.27
DOMAIN	DOMAIN FOR ANALYTIC FIT	1.2.28
SMLEQU	ANALYTIC EQUILIBRIUM IN DOMAIN	1.2.29
YYP(7)	PARABOLIC FIT	1.2.30
BNDRY	BOUNDARY FOR HELICAL GEOMETRY	1.2.31
OUTEQU(1)	PRINT OUT EQUILIBRIUM QUANTITIES	1.3.01
IODSK1(1)	DISK OPERATIONS FOR ERATO1	1.3.02

********** LION2 **********

VACUUM	ORGANIZE VACUUM	2.2.01
TETMSH	THETA MESH IN VACUUM	2.2.02
ABCDEF	MATRICES A , B , C , D , E , F	2.2.03
ROTETA(3)	RO , TETA AT INTEGRATION POINTS	2.2.04
SHELL(5)	POSITION OF THE SHELL	2.2.05
CONCEL(3)	CONTRIBUTION PER CELL	2.2.06
QCON	MATRIX Q	2.2.07
ZERO(1)	REDUCES FOR N=0	2.2.08
WCON	VACUUM MATRIX	2.2.09
SYMETR	SYMMETRICITY CONDITION	2.2.10
MULT(4)	MULTIPLIES TWO MATRICES	2.2.11
EKN(4)	ELLIPTIC INTEGRALS	2.2.12
EK(3)	COMPLETE ELLIPTIC INTEGRALS	2.2.13

IMGC(4)	MATRIX INVERSION	2.2.14
CURRENT	ANTENNA CURRENT.JUMP OF POTENTIAL	2.2.15
MATVEC	REAL MATRIX * COMPLEX VECTOR	2.2.16
RALD	LDU DECOMPOSITION OF A REAL MATRIX	2.2.17
MOPPOW	MATRIX OPERATIONS FOR POWER AT ANTENNA	2.2.18
EKN	ELLIPTICAL INTEGRAL KN AND DKN/DPETA	2.2.19
EKNSIE	ELLIPTICAL INTEGRAL WITH SERIES	2.2.20
EKNLIM	ELLIPTICAL INTEGRAL WITH BESSEL	2.2.21
BESMDI	MODIFIED BESSEL FUNCTION I	2.2.22
BESMDK	MODIFIED BESSEL FUNCTION K	2.2.23
NUM	UP/DOWN/UP/DOWN NUMBERING	2.2.24
IODSK2	DISK I/O OPERATIONS FOR LION2	2.3.01

********** LION3 **********

AANDB	ORGANIZE MATRIX CONSTRUCTION	3.2.01
CONMAT	CONSTRUCT MATRIX A	3.2.02
INTEGR	CONTRIBUTION OF ONE CELL TO MATRIX A	3.2.03
AHYBRD	CONSTRUCTS LOCAL 6*6 MATRIX (HYBRID ELEM.)	3.2.04
STORE	ADD LOCAL CONTRIB. TO MATRIX BLOCK	3.2.06
CONDIT	BLOCK OVERLAP AND BOUNDARY CONDITIONS	3.2.07
ADDVAC	ADD VACUUM CONTRIBUTION	3.2.09
AWAY	REMOVE A COLUMN AND A ROW OF LOCAL MATRIX	3.2.10
DEC	GLOBAL NUMBERING OF UNKNOWNS IN A CELL	3.2.11
BASIS2	BASIS FUNCTIONS OF LINEAR HYBRID ELEMENTS	3.2.12
EQCHG	OBTAIN LOWER HALF-PLANE EQUILIBRIUM QUANT.	3.2.13
QUAEQU	PHYSICAL LOCAL QUANTITIES	3.2.14
FRPROF	PROFILES OF ION DENSITIES	3.2.15
SHAPE	SHAPE OF PROFILE	3.2.16
DAMPIN	WAVE PHENOMENOLOGICAL DAMPIN	3.2.17
TEMPI	TEMPERATURE OF ION SPECIES	3.2.18
DISPFN	FRIED-CONTE DISPESION FUNCTION	3.2.19
ERROR	ERROR FUNCTION	3.2.20
BESSEL	BESSEL ROUTINE FOR ERROR	3.2.21
CONST1	COEFFICIENTS C-J OF WEAK FORM TERMS	3.2.22
CONST2	COEFFICIENTS OF UNKNOWNS OF W.F. TERMS	3.2.23
VECT	MULTIPLY W.F.TERMS WITH BASIS FUNCTIONS	3.2.24
DIADIC	CONTRIBUTION OF ONE W.F.TERM TO MATRIX	3.2.25
ADD	ADD CONTRIB. OF ONE TERM TO LOCAL MATRIX	3.2.26
IODSK3	DISK I/O OPERATIONS FOR LION3	3.3.01

********** LION4 **********

ORGAN4	ORGANIZE ALGEBRAIC SYSTEM RESOLUTION	4.2.01
SET4	INITIALIZE LION4	4.2.02
POWER	COMPUTE TOTAL POWER	4.2.03
NOSYBL	SOLVE COMPLEX BLOCK NON-SYM LIN.SYSTEM	4.2.04
FXFU	PUT SOURCE VECTOR INTO XT	4.2.05
CONALR	DECOMPOSE A INTO LDU	4.2.06

CALD	DECOMPOSE A BLOCK OF A INTO LDU		4.2.07
CBXLU	SOLVE LOWER TRIANGULAR SYSTEM		4.2.08
CDLHXV	SOLVE UPPER TRIANGULAR SYSTEM		4.2.09
EIGEN	COMPUTE THE NORM OF A*XT		4.2.10
VAX	MULTIPLY A BLOCK OF A WITH SOLUTION VECTOR		4.2.11
ENDXUV	TERMINATE THE CALCULATION		4.2.12
GETRG	GET A SECTION OF VECTOR XT		4.2.13
PUTRG	PUT A VECTOR INTO XT		4.2.14
INFORM	DATE AND COMPUTER TIME		4.2.15
CVZERO	ZEROES A COMPLEX VECTOR		VS00
CAXPY	Y = Y + A * X (COMPLEX)	($SCILIB)	VS01
CCOPY	COPIES X ONTO Y	($SCILIB)	VS02
CDOTU	SCALAR PRODUCT X*Y	($SCILIB)	VS03
CSCAL	SCALES A VECTOR BY A CONSTANT	($SCILIB)	VS04
CDOTC	SCALAR PRODUCT CONJG(X)*Y	($SCILIB)	VS05
IODSK4	DISK I/O FOR LION4		4.3.01

********** LION5 **********

DIAGNO	ORGANIZE THE DIAGNOSTICS	5.1.01
INIT	INITIALIZE LION5	5.2.01
ENERGY	POWER AND ENERGY DIAGNOSTICS	5.2.02
FIELDS	FIELDS DIAGNOSTICS	5.2.03
FOURIE	COMPLEX FOURIER ANALYSIS IN CHI	5.2.04
EQUANT	EQUILIBRIUM QUANTITIES DIAGNOSTICS	5.2.05
THEEND	TERMINATE THE CALCULATION	5.2.99
CENTER	VALUE OF UNKNOWNS AT CENTER OF CELL	5.3.01
ELECTR	ELECTRIC FIELD,NORMAL AND PERP	5.3.02
LOCPOW	LOCAL POWER ABSORPTION	5.3.03
MAGNET	WAVE MAGNETIC FIELD	5.3.04
POYNTI	POYNTING VECTOR	5.3.05
SFLINT	CONTRIBUTION TO POYNTING FLUX	5.3.06
OUTP5	LINE-PRINTER OUTPUT	5.4.01
TABLE	2-D PRINTOUT	5.4.02
TABLEF	PRINTOUT OF POLOIDAL FOURIER COMPONENTS	5.4.03
PLOT5	GRAPHICAL OUTPUT	5.4.04
ARROW	2-D VECTOR FIELD PLOT	5.4.05
SCAPLO	2-D SCALAR FIELD PLOT	5.4.06
SURFPL	PLOT THE PLASMA SURFACE	5.4.07
LABPLO	PLOT THE LABELS	5.4.08
LEVEL	2-D SCALAR PLOT : CONTOUR LINES	5.4.10
LZERO	PLOT THE ZEROS OF VOUT1	5.4.11
CONTOR	PLOT THE LINE VOUT1=0.0	5.4.13
ACROSS	LINEAR INTERPOLATION	5.4.14
IODSK5	DISK I/O OPERATIONS FOR LION5	5.5.01

INDEX OF COMMON BLOCKS

VERSION 10 LDV MARCH 1986 CRPP LAUSANNE

ALPHABETIC INDEX OF COMMON VARIABLES

VERSION 10 LDV MARCH 1986 CRPP LAUSANNE

AJR	CURRENT DENSITY	R	3.2
ALARG	*WIDTH OF 2-D PLOTS	R	5.1
AMASS(MDSPEC)	*ATOMIC MASSES OF ION SPECIES	RA	2.1
ANGLE(16)	*TOROIDAL CUTS (DEGREES)	RA	5.1
ANTR(MDIN2)	ANTENNA VECTOR	CA	9.2
ANTRAD	*ANTRAD-1.=DISTANCE ANTENNA-PLASMA	R	2.1
ANTUP	*UPPER POSITION OF LFS/HFS ANTENNA (DEGREES)	R	2.1
ANU	*CAUSAL DAMPING ADDED TO DIELECTRIC TENSOR	R	2.1
APHI	TOROIDAL ANGLE PHI	R	9.5
APP(10)	PARAMETERS FOR ANALYTICALLY GIVEN DP/DPSI	RA	9.1
AR(201)	R DURING ANALYTICAL INTEGRATION	RA	3.2
ARSIZE	*SIZE OF ARROWS	R	5.1
ASPCT	*INVERSE ASPECT RATIO FOR SOLOVEV EQUILIBRIU	R	2.1
ASYMB	*SIZE OF SYMBOLS	R	5.1
ATTP(19)	PARAMETERS FOR T*DT/DPSI	RA	9.1
AZ(201)	Z DURING ANALYTICAL INTEGRATION	RA	3.2
B2R2	*CONSTANT B2 FOR SOLOVEV EQUILIBRIUM	R	2.1
BETA	BETA VALUE	R	2.1
BETAP	BETA POLOIDAL	R	2.1
BETAS	BETA STAR PRINCETON	R	2.1
BETRZ(MDRZ)	NON-ORTHOGONALITY IN CHI	RA	9.1
BNL	NORMAL COMPONENT OF WAVE MAGNETIC FIELD	C	9.5
BNOT	*MAGNETIC FIELD AT MAGNETIC AXIS (TESLA)	R	2.1
BP	POLOIDAL MAGNETIC FIELD	R	3.2
BPARL	PARALLEL COMP. OF WAVE MAGNETIC FIELD	C	9.5
BPL	PERP. COMP. OF WAVE MAGNETIC FIELD	C	9.5
CA	CONSTANT TO DEFINE SHELL	R	9.2
CA(MDOVL)	OVERLAP SUBBLOCK OF MATRIX A	CA	3.3
CB	#	R	9.2
CC	#	R	9.2
CCHI(MDIN2)	CHI VALUES AT CENTER OF CELLS	RA	9.5
CCR(MDPSI,MDCHI)	R AT CENTER OF CELLS	RA	9.5
CCS(MDPSI)	S VALUES AT CENTER OF CELLS	RA	9.5
CCZ(MDPSI,MDCHI)	Z AT CENTER OF CELLS	RA	9.5
CDEVIA	WIDTH OF POWER DISTRIBUTION IN CHI	R	9.5
CDQ(MDPSI1)	DQ/DPSI	RA	2.1
CELPOW(MDPSI,MDIN2)	POWER ARBSORBED IN THE CELLS	RA	9.5
CENDEN(MDSPEC)	*DENSITIES OF ION SPECIES AT MAGN.AXIS (M-3)	RA	2.1
CENTI(MDSPEC)	*ION TEMPERATURES AT MAGN.AXIS (EV)	RA	2.1
CEOMCI(MDSPEC)	*NORMALIZED ION CYCLOTRON FREQUENCIES	RA	2.1
CHI(MDCHI1)	CHI MESH VALUES	RA	3.1
CHIPOW(MDIN2)	POWER ABSORBED ON CHI=CONST.	RA	9.5
CHIRZ(MDRZ)	CHI(R,Z) AT CROSS POINTS WITH PSI=CONSTANT	RA	9.1
CIQ(MDPSI1)	1./Q	RA	2.1
CMEAN	CENTER OF POWER DISTRIBUTION IN CHI	R	9.5
CMERC(MDPSI1)	MERCIER CRITERION	RA	2.1
CNR(MDPSI,MDCHI)	NORMAL TO PSI=CONST., R COMPONENT	RA	9.5
CNZ(MDPSI,MDCHI)	NORMAL TO PSI=CONST., Z COMPONENT	RA	9.5
CONA(6,6)	LOCAL (CELL) CONTRIBUTION TO A	CA	3.3
CONMSH(3,5)	*COEFFICIENTS FOR IRREGULAR S-MESH	RA	3.1

CPI	3.141592653589793	R	3.2
CPL	POWER ABSORBED IN A CELL	R	9.5
CPLE	POWER IN A CELL DUE TO NU	R	9.5
CPPR(MDPSI1)	DP/DPSI	RA	2.1
CPR(MDPSI1)	-----	RA	2.1
CPSEQ(MDR,MDZ)	PSI(R,Z) FROM EQUILIBRIUM CODE	RA	9.1
CPSI(MDPSI1)	PSI MESH VALUES	RA	3.1
CPSRF	*PSI AT PLASMA SURFACE	R	2.1
CR(MDCHI)	R(CHI,PSI=CONSTANT)	RA	3.1
CS(MDPSI1)	S MESH VALUES	RA	3.1
CST	*1. / (Q(AXIS) * CPSRF)	R	2.1
CURASY(MDFOUR)	*AMPLITUDE OF SIN ANTENNA CURRENT (HELICAL)	RA	2.1
CURSYM(MDFOUR)	*AMPLITUDE OF ANTENNA CURRENT	RA	2.1
CZ(MDCHI)	Z(CHI,PSI=CONSTANT)	RA	3.1
D2ROP	D**2RHO/DTHETA**2 AT MID-POINT	R	9.2
DBP2	PSI DERIVATIVE OF BP**2	R	3.2
DC(MD2CP2)	DELTA-CHI	RA	9.2
DENPOW(MDPSI,MDIN2)	POWER ABSORPTION DENSITY	RA	9.5
DPDR(MDCHI)	DPSI/DR (CHI,PSI=CONSTANT)	RA	3.1
DPDZ(MDCHI)	DPSI/DZ (CHI PSI=CONSTANT)	RA	3.1
DPL	POWER ABSORPTION DENSITY AT CENTER OF CELL	R	9.5
DPLE	POWER ABSORPTION DENSITY DUE TO NU	R	9.5
DPR	DPSI/DR	R	3.2
DPZ	DPSI/DZ	R	3.2
DQ(3)	DQ/DPSI	RA	2.1
DRODT(4)	DRHO/DTHETA AT INTEGRATION POINTS	RA	9.2
DROPDT(4)	DRHOPRIME/DTHETA	RA	9.2
DVDC	DV/DCHI	C	9.5
DXDC	DX/DCHI	C	9.5
DXDS	DX/DS	C	9.5
ECHEL	SCALE FACTOR FOR 2-D PLOTS	R	9.5
ELEPOW	POWER DUE TO NU	R	9.5
ELLIPT	*ELLIPTICITY SQUARED FOR SOLOVEV EQUILIBRIUM	R	2.1
ENL	NORMAL COMPONENT OF WAVE ELECTRIC FIELD	C	9.5
EPL	PERP. COMP. OF WAVE ELECTRIC FIELD	C	9.5
EPSMAC	*ROUND-OFF ERROR OF COMPUTER	R	3.5
EQ(20,MDCHI)	EQUILIBRIUM QUANTITIES FOR PSI=CONSTANT	RA	2.2
EQDENS	*PROFILE PARAMETER OF TOTAL MASS DENSITY	R	2.1
EQKAPD	*PROFILE PARAMETER OF TOTAL MASS DENSITY	R	2.1
EQKAPT(MDSPEC)	*PROFILE OF ION TEMPERATURE	RA	2.1
EQPS(MDR)	DP/DPSI(R) GIVEN POINTWISE	RA	9.1
EQR(MDR)	R MESH FROM EQUILIBRIUM	RA	9.1
EQT(MDR)	T(R) GIVEN POINTWISE	RA	9.1
EQTI(MDSPEC)	*PROFILE OF ION TEMPERATURE	RA	2.1
EQZ(MDZ)	Z MESH FROM EQUILIBRIUM	RA	9.1
FEEDUP	*POSITION OF UPPER FEEDER OF LFS/HFS ANTENNA	R	2.1
FIT(16)	FIT PARAMETERS	RA	3.2
FLUPOW(MDPSI1)	POWER ABSORBED INSIDE PSI=CONST.	RA	9.5
FRAC(MDSPEC)	*MASS FRACTION OF ION SPECIES	RA	2.1
FRCEN(MDSPEC)	*CENTER OF ION DENSITY PROFILE	RA	2.1
FRDEL(MDSPEC)	*WIDTH OF ION DENSITY PROFILE	RA	2.1
FREN(13,MDPSI)	FOURIER DECOMPOSITION IN CHI OF E-N	CA	9.5
FREP(13,MDPSI)	FOURIER DECOMPOSITION IN CHI OF E-PERP	CA	9.5

FREQCY	*FREQUENCY OF GENERATOR (HZ)	R	2.1
FRINT(7,MDCHI)	INTEGRAL FOR FOURIER DECOMPOSITION	CA	9.5
G(MDIN2,MDIN2,13)	ALL MATRICES	RA	9.2
GAMMA	ADIABATICITY INDEX	R	2.1
ILOC(MDCHI)	COUNTER FOR POLYNOMIAL WICH CUTS CHI=CONST	IA	9.1
ITEST		I	5.2
LENGTH	*NB.OF ELEMENTS OF A MATRIX BLOCK	I	3.2
M1	RANK OF MATRIX OVERLAP SUBBLOCK	I	3.5
M11	M1+1	I	3.5
M12	M1+M2 = RANK OF MATRIX BLOCK	I	3.5
M2	RANK OF MATRIX BLOCK - M1	I	3.5
MANCMP	*NB.OF POLOIDAL WAVE NUMBERS (HELICAL ANT.)	I	2.1
MEQ	*EQUILIBIUM QUANTITIES	I	5.2
MPOLWN(MDFOUR)	*POLOIDAL WAVE NUMBERS (HELICAL ANT.)	IA	2.1
N	NB. OF MATRIX BLOCKS (=NPSI)	I	3.5
NAN	*NUMBER OF ANALYTIC PSI SURFACES	I	3.2
NANL	LEFT R COUNTER FOR ANALYTICAL FIT	I	3.2
NANR	RIGHT R COUNTER FOR ANALYTICAL FIT	I	3.2
NANTYP	*SELECTS 1:HELICAL OR 2:LFS/HFS ANTENNA	I	2.1
NANZ	UPPER Z COUNTER FOR ANALYTICAL FIT	I	3.2
NCHI	*NUMBER OF CHI INTERVALS IN UPPER HALF-PLANE	I	3.1
NCOLMN	*RANK OF A MATRIX BLOCK	I	3.2
NCOMP	NB. OF ELEMENTS OF SOLUTION VECTOR	I	3.5
NCONTR	*NUMBER OF CONTOUR LINES	I	5.1
NCONV		I	3.5
NDA	*MATRIX A	I	5.2
NDB		I	5.2
NDES	*R,Z COORDINATES AND NORMALS	I	5.2
NDIM	DIMENSION OF MATRICES	I	9.2
NDLT	*DECOMPOSED MATRIX L,D,U	I	5.2
NDORY	*NUMERICAL EQUILIBRIUM	I	5.2
NDS	*SOLUTION VECTOR	I	5.2
NDSCRC	*SCRATCH SPACE	I	5.2
NEG		I	3.5
NFIG	*NUMBER OF TOROIDAL CUTS	I	5.1
NIT		I	3.5
NITMAX		I	3.5
NLCOLD	*SELECTS COLD OR LUKEWARM PLASMA MODEL	L	2.1
NLDIP	*SELECTS MONO/DIPOLE ANTENNA FOR LFS OR HFS	L	2.1
NLONG	NB. OF ELEMENTS IN A MATRIX BLOCK	I	3.5
NLOTPo	*GENERAL LINE-PRINTER OUTPUT SWITCH	L	5.1
NLOTP1(4)	*OUTPUT SWITCHES FOR LION1	LA	5.1
NLOTP2(5)	*OUTPUT SWITCHES FOR LION2	LA	5.1
NLOTP3(2)	*OUTPUT SWITCHES FOR LION3	LA	5.1
NLOTP4(5)	*OUTPUT SWITCHES FOR LION4	LA	5.1
NLOTP5(25)	*OUTPUT SWITCHES FOR LION5	LA	5.1
NLPLO5(25)	*PLOT SWITCHES FOR LION5	LA	5.1
NLQUAD	QUADRATIC TERM IN THE WEAK FORM	L	3.3
NLTORE	SELECTS THE TOROIDAL GEOMETRY	L	5.1
NLY		L	5.1
NMESH	AUTOMATIC IRREGULAR S-MESH	I	5.1
NPIN(14)	INPUT PARAMETERS FOR ALGEBRAIC SOLVER	IA	3.5
NPLAC(6)	GLOBAL NUMBERING OF CELL MESH POINTS	IA	3.3
NPOL	*TOTAL NUMBER OF CHI INTERVALS	I	3.1

NPOUT(14)	OUTPUT PARAMETERS FOR ALGEBRAIC SOLVER	IA	3.5
NPRNT	*LINE-PRINTER OUTPUT	I	5.2
NPSI	*NUMBER OF S INTERVALS	I	3.1
NR	*NUMBER OF EQUILIBRIUM MESH POINTS IN R	I	3.2
NRSPEC	*NUMBER OF ION SPECIES	I	2.1
NRZ	NUMBER OF R-Z CUTS WITH PSI=CONSTANT	I	9.1
NRZS	NRZ(PSI AT SURFACE)	I	9.1
NRZSUR	NUMBER OF POINTS FOR PLOTTING THE SURFACE	I	9.5
NSAVE	*NAMELIST LINK LION1 TO 5	I	5.2
NSCRTC	*SCRATCH SPACE	I	5.2
NSHIFT	PERFORM SHIFT IN NQ	I	3.1
NSING	SINGULARITY INDICATOR (=-1 IF A IS SING.)	I	3.5
NSUR	*PLASMA SURFACE	I	5.2
NTCASE	*=2:SOLOVEV, =3:NUMERICAL EQUILIBRIUM	I	5.1
NTURN	NUMBER OF TURNS FOR BALOONING CRITERION	I	3.2
NUM	MAX(NAN+1,SQRT(NPSI)+1)	I	3.2
NVAC	*VACUUM QUANTITIES	I	5.2
NZ	*NUMBER OF EQUILIBRIUM MESH POINTS IN Z	I	3.2
OHMR(MDIN2)	OHM VECTOR	CA	9.2
OMEGA	*NORMALIZED FREQUENCY (*RMAJOR/ALFV.SPEED)	R	2.1
PSILIM	PSI AT LIMITER	R	3.2
Q(3)	SAFETY FACTOR Q	RA	2.1
QB	SAFETY FACTOR AT PLASMA SURFACE	R	9.2
QIAXE	*1./Q(AXIS) FOR SOLOVEV EQUILIBRIUM	R	2.1
QPSI(MDPSI1)	SAFETY FACTOR Q	RA	2.1
RAXIS	POSITION OF MAGNETIC AXIS (IN EQU.UNITS)	R	9.1
REASCR	REACTANCE SCALAR	C	9.2
REXT	*1.-REXT = DISTANCE SHELL-PLASMA	R	2.1
RHO(MDPSI1)	TOTAL MASS DENSITY	RA	2.1
RMAG	POSITION OF MAGNETIC AXIS (IN ERATO=1)	R	9.1
RMAJOR	*MAJOR RADIUS (M)	R	2.1
RO(4)	RHO AT INTEGRATION POINTS	RA	9.2
RO2	RHO AT THE CENTER	R	9.2
RO2P	RHO PRIME AT THE CENTER	R	9.2
ROP(4)	RHO PRIME AT INTEGRATION POINTS	RA	9.2
RPSI1	PSI AT MAGNETIC AXIS (IN EQU. UNITS)	R	9.1
RRO(MDRZ)	RHO(PSI=CONSTANT)	RA	9.1
RRS(MDRZ)	R(PSI=CONSTANT)	RA	9.1
RSUR	OUTER RADIAL POSITION OF PSI=CPSRF	R	2.1
RZS(MDRZ)	Z(PSI=CONSTANT)	RA	9.1
SAUTR(MDIN2)	JUMP ACROSS ANTENNA SURFACE	CA	9.2
SAUTX(MDIN2)	TEMPORARY	CA	9.2
SB2	TOTAL MAGNETIC PRESSURE	R	2.1
SCALE	*SCALE FACTOR FOR NUMERICAL EQUILIBRIUM	R	2.1
SDEVIA	WIDTH OF POWER DISTRIBUTION IN S	R	9.5
SFLUX(MDPSI)	POYNTING FLUX ACROSS PSI=CONST.	RA	9.5
SI	TOTAL PLASMA CURRENT	R	2.1
SIGMA	*NORM FACTOR FOR V-THEMAL (IONS)	R	2.1
SMEAN	MINOR RADIUS OF HALF POWER ABSORPTION	R	9.5
SN(MDPSI,MDIN2)	NORMAL COMPONENT OF POYNTING	RA	9.5
SNL	NORMAL COMPONENT OF POYNTING	R	9.5
SOURCE(MDIN2)	SOURCE VECTOR	CA	9.2
SP	TOTAL PRESSURE	R	2.1
SP2	TOTAL PRESSURE SQUARED	R	2.1
SPAR(MDPSI,MDIN2)			

	PARALLEL COMPONENT OF POYNTING	RA	9.5
SPARL	PARALLEL COMPONENT OF POYNTING	R	9.5
SPERP(MDPSI,MDIN2)			
	PERP. COMPONENT OF POYNTING	RA	9.5
SPL	PERP. COMP. OF POYNTING	R	9.5
SR(MD2CP2)	R(CHI) DEFINING PLASMA SURFACE	RA	9.2
SV	TOTAL PLASMA VOLUME	R	2.1
SZ(MD2CP2)	Z(CHI) DEFINING PLASMA SURFACE	RA	9.2
T(MD2CP2)	THETA AT CHI MESH POINTS	RA	9.2
To	T(AXIS) IN EQUILIBRIUM UNITS	R	9.1
TB	TOROIDAL MAGNETIC FLUX AT PLASMA SURFACE	R	9.2
TETA(MDRZ)	THETA(PSI=CONSTANT)	RA	9.1
TH(MD2CP2)	THETA AT CENTER OF CHI MESH	RA	9.2
TLIM	ERATO T(AXIS)=1 FIXED WHILE SCALING	R	9.1
TMF(MDPSI1)	TOROIDAL MAGNETIC FLUX T	RA	2.1
TP(4)	THETA PRIME AT INTEGRATION POINTS	RA	9.2
TQP(MDPSI1)	D(T/Q) / DPSI	RA	2.1
TT(4)	THETA AT INTEGRATION POINTS	RA	9.2
TTP(MDPSI1)	T * DT/DPSI	RA	2.1
U(MDCOL)	VECTOR OF UNKNOWS FOR ONE BLOCK	CA	3.4
UT	TEMPORARY STORAGE	C	3.4
VA(MDCOL)	TEMPORARY STORAGE	CA	3.4
VC	V	C	9.5
VOUT1(MDPSI,MDIN2)			
	TEMPORARY STORAGE	RA	9.5
VOUT2(MDPSI,MDIN2)			
	TEMPORARY STORAGE	RA	9.5
WBETCH	NON-ORTHOGONALITY OF PSI,CHI (BETA-CHI)	R	2.2
WBPOL2	POLOIDAL FIELD SQUARED	R	2.2
WBTOR2	TOROIDAL FIELD SQUARED	R	2.2
WBTOT	TOTAL FIELD	R	2.2
WBTOT2	TOTAL FIELD SQUARED	R	2.2
WCHI	CHI AT CENTER OF THE CELL	R	2.2
WCOMEG	COMPLEX NORMALIZED FREQUENCY	C	2.2
WDCHI	CHI WIDTH OF CELL	R	2.2
WDS	S WIDTH OF CELL	R	2.2
WEPS	DIELECTRIC TENSOR COMPONENT EPSILON N-N	C	2.2
WFRAC(MDSPEC)	MASS FRACTION OF ION SPECIES	RA	2.2
WG	DIELECTRIC TENSOR COMPONENT EPSILON N-PERP	C	2.2
WGRPS2	GRADIENT OF PSI SQUARED	R	2.2
WH	COEFFICIENT H	R	2.2
WIDTH	WIDTH OF DISTRIBUTION OF CHI MESH POINTS	R	3.1
WJAC	JACOBIEN OF PSI,CHI COORDINATE SYSTEM	R	2.2
WK	COEFFICIENT K	R	2.2
WNL	HELICITY	R	2.1
WNTORE	*TOROIDAL WAVE NUMBER N	R	2.1
WNU	WAVE DAMPING	R	2.2
WOMCI(MDSPEC)	NORMALIZED ION-CYCLOTRON FREQUENCY	RA	2.2
WPSI	PSI	R	2.2
WQ	SAFETY FACTOR Q	R	2.2
WR2	R SQUARED	R	2.2
WRHO	MASS DENSITY	R	2.2
WS	S COORDINATE AT CENTER OF THE CELL	R	2.2
WT	TOROIDAL FLUX FUNCTION T	R	2.2
WTQ	T/Q	R	2.2

X(MDCOL)	VECTOR OF UNKNOWNS FOR ONE BLOCK	CA	3.4
XC	X	C	9.5
XC1(8)	CONSTANTS C-J OF WEAK FORM TERMS	CA	3.3
XDCHI(MDIN2)	DELTA-CHI AT PLASMA SURFACE	RA	3.4
XDTH(MDIN2)	DELTA-THETA AT PLASMA SURFACE	RA	3.4
XETA(5)	CONSTANTS OF TEST-FUNCTIONS	CA	3.3
XF(16)	BASIS FUNCTIONS AT MESH POINTS	RA	3.3
XINT(201)	INTEGRAL VALUES FOR Q AND CHI	RA	3.2
XINT2(201)	INTEGRAL VALUES FOR NON-ORTHOGONALITY	RA	3.2
XKSI(5)	CONSTANTS OF UNKNOWNS	CA	3.3
XM(6,6)	CONTRIBUTION OF ONE TERM OF THE WEAK FORM	CA	3.3
XNORM	VECTOR NORM SQUARED	R	3.5
XOHMR(MDIN2)	OHM VECTOR FOR POWER AT ANTENNA	CA	3.4
XS(MDRZ)	R COORDINATES OF PLASMA SURFACE	RA	9.5
XT(MDCOMP)	TOTAL VECTOR OF UNKNOWNS	CA	3.4
XVETA(6)	VECTOR OF COEFFICIENTS FOR TEST-FUNCTIONS	CA	3.3
XVKSI(6)	VECTOR OF COEFFICIENTS FOR UNKNOWNS	CA	3.3
YS(MDRZ)	Z COORDINATES OF PLASMA SURFACE	RA	9.5

INDEX OF COMMON VARIABLES

VERSION 10 LDV MARCH 1986 CRPP LAUSANNE

C2.1 GENERAL PHYSICS VARIABLES

VERSION 10 LDV MARCH 1986 CRPP LAUSANNE

COMMON/COMPHY/

ACHARG(MDSPEC)	*ATOMIC CHARGES OF ION SPECIES	RA	2.1
AMASS(MDSPEC)	*ATOMIC MASSES OF ION SPECIES	RA	2.1
ANTRAD	*ANTRAD-1.=DISTANCE ANTENNA-PLASMA	R	2.1
ANTUP	*UPPER POSITION OF LFS/HFS ANTENNA (DEGREES)	R	2.1
ANU	*CAUSAL DAMPING ADDED TO DIELECTRIC TENSOR	R	2.1
ASPCT	*INVERSE ASPECT RATIO FOR SOLOVEV EQUILIBRIU	R	2.1
B2R2	*CONSTANT B2 FOR SOLOVEV EQUILIBRIUM	R	2.1
BETA	BETA VALUE	R	2.1
BETAP	BETA POLOIDAL	R	2.1
BETAS	BETA STAR PRINCETON	R	2.1
BNOT	*MAGNETIC FIELD AT MAGNETIC AXIS (TESLA)	R	2.1
CDQ(MDPSI1)	DQ/DPSI	RA	2.1
CENDEN(MDSPEC)	*DENSITIES OF ION SPECIES AT MAGN.AXIS (M-3)	RA	2.1
CENTI(MDSPEC)	*ION TEMPERATURES AT MAGN.AXIS (EV)	RA	2.1
CEOMCI(MDSPEC)	*NORMALIZED ION CYCLOTRON FREQUENCIES	RA	2.1
CIQ(MDPSI1)	1./Q	RA	2.1
CMERC(MDPSI1)	MERCIER CRITERION	RA	2.1
CPPR(MDPSI1)	DP/DPSI	RA	2.1
CPR(MDPSI1)	-----	RA	2.1
CPSRF	*PSI AT PLASMA SURFACE	R	2.1
CST	*1. / (Q(AXIS) * CPSRF)	R	2.1
CURASY(MDFOUR)	*AMPLITUDE OF SIN ANTENNA CURRENT (HELICAL)	RA	2.1
CURSYM(MDFOUR)	*AMPLITUDE OF ANTENNA CURRENT	RA	2.1

DQ(3)	DQ/DPSI	RA	2.1
ELLIPT	*ELLIPTICITY SQUARED FOR SOLOVEV EQUILIBRIUM	R	2.1
EQDENS	*PROFILE PARAMETER OF TOTAL MASS DENSITY	R	2.1
EQKAPD	*PROFILE PARAMETER OF TOTAL MASS DENSITY	R	2.1
EQKAPT(MDSPEC)	*PROFILE OF ION TEMPERATURE	RA	2.1
EQTI(MDSPEC)	*PROFILE OF ION TEMPERATURE	RA	2.1
FEEDUP	*POSITION OF UPPER FEEDER OF LFS/HFS ANTENNA	R	2.1
FRAC(MDSPEC)	*MASS FRACTION OF ION SPECIES	RA	2.1
FRCEN(MDSPEC)	*CENTER OF ION DENSITY PROFILE	RA	2.1
FRDEL(MDSPEC)	*WIDTH OF ION DENSITY PROFILE	RA	2.1
FREQCY	*FREQUENCY OF GENERATOR (HZ)	R	2.1
GAMMA	ADIABATICITY INDEX	R	2.1
OMEGA	*NORMALIZED FREQUENCY (*RMAJOR/ALFV.SPEED)	R	2.1
Q(3)	SAFETY FACTOR Q	RA	2.1
QIAXE	*1./Q(AXIS) FOR SOLOVEV EQUILIBRIUM	R	2.1
QPSI(MDPSI1)	SAFETY FACTOR Q	RA	2.1
REXT	*1.-REXT = DISTANCE SHELL-PLASMA	R	2.1
RHO(MDPSI1)	TOTAL MASS DENSITY	RA	2.1
RMAJOR	*MAJOR RADIUS (M)	R	2.1
RSUR	OUTER RADIAL POSITION OF PSI=CPSRF	R	2.1
SB2	TOTAL MAGNETIC PRESSURE	R	2.1
SCALE	*SCALE FACTOR FOR NUMERICAL EQUILIBRIUM	R	2.1
SI	TOTAL PLASMA CURRENT	R	2.1
SIGMA	*NORM FACTOR FOR V-THEMAL (IONS)	R	2.1
SP	TOTAL PRESSURE	R	2.1
SP2	TOTAL PRESSURE SQUARED	R	2.1
SV	TOTAL PLASMA VOLUME	R	2.1
TMF(MDPSI1)	TOROIDAL MAGNETIC FLUX T	RA	2.1
TQP(MDPSI1)	D(T/Q) / DPSI	RA	2.1
TTP(MDPSI1)	T * DT/DPSI	RA	2.1
WNL	HELICITY	R	2.1
WNTORE	*TOROIDAL WAVE NUMBER N	R	2.1
MANCMP	*NB.OF POLOIDAL WAVE NUMBERS (HELICAL ANT.)	I	2.1
MPOLWN(MDFOUR)	*POLOIDAL WAVE NUMBERS (HELICAL ANT.)	IA	2.1
NANTYP	*SELECTS 1:HELICAL OR 2:LFS/HFS ANTENNA	I	2.1
NRSPEC	*NUMBER OF ION SPECIES	I	2.1
NLCOLD	*SELECTS COLD OR LUKEWARM PLASMA MODEL	L	2.1
NLDIP	*SELECTS MONO/DIPOLE ANTENNA FOR LFS OR HFS	L	2.1

C2.2 EQUILIBRIUM QUANTITIES

VERSION 10 LDV MARCH 1986 CRPP LAUSANNE

COMMON/COMEQU/

WCOMEG	COMPLEX NORMALIZED FREQUENCY	C	2.2
WEPS	DIELECTRIC TENSOR COMPONENT EPSILON N-N	C	2.2
WG	DIELECTRIC TENSOR COMPONENT EPSILON N-PERP	C	2.2
EQ(20,MDCHI)	EQUILIBRIUM QUANTITIES FOR PSI=CONSTANT	RA	2.2
WBETCH	NON-ORTHOGONALITY OF PSI,CHI (BETA-CHI)	R	2.2
WBPOL2	POLOIDAL FIELD SQUARED	R	2.2
WBTOR2	TOROIDAL FIELD SQUARED	R	2.2
WBTOT	TOTAL FIELD	R	2.2
WBTOT2	TOTAL FIELD SQUARED	R	2.2
WCHI	CHI AT CENTER OF THE CELL	R	2.2
WDCHI	CHI WIDTH OF CELL	R	2.2

WDS	S WIDTH OF CELL	R	2.2
WFRAC(MDSPEC)	MASS FRACTION OF ION SPECIES	RA	2.2
WGRPS2	GRADIENT OF PSI SQUARED	R	2.2
WH	COEFFICIENT H	R	2.2
WJAC	JACOBIEN OF PSI,CHI COORDINATE SYSTEM	R	2.2
WK	COEFFICIENT K	R	2.2
WNU	WAVE DAMPING	R	2.2
WOMCI(MDSPEC)	NORMALIZED ION-CYCLOTRON FREQUENCY	RA	2.2
WPSI	PSI	R	2.2
WQ	SAFETY FACTOR Q	R	2.2
WR2	R SQUARED	R	2.2
WRHO	MASS DENSITY	R	2.2
WS	S COORDINATE AT CENTER OF THE CELL	R	2.2
WT	TOROIDAL FLUX FUNCTION T	R	2.2
WTQ	T/Q	R	2.2

C3.1 (R,Z) AND (PSI,CHI) MESH VARIABLES

VERSION 10 LDV MARCH 1986 CRPP LAUSANNE

COMMON/COMESH/

CHI(MDCHI1)	CHI MESH VALUES	RA	3.1
CONMSH(3,5)	*COEFFICIENTS FOR IRREGULAR S-MESH	RA	3.1
CPSI(MDPSI1)	PSI MESH VALUES	RA	3.1
CR(MDCHI)	R(CHI,PSI=CONSTANT)	RA	3.1
CS(MDPSI1)	S MESH VALUES	RA	3.1
CZ(MDCHI)	Z(CHI,PSI=CONSTANT)	RA	3.1
DPDR(MDCHI)	DPSI/DR (CHI,PSI=CONSTANT)	RA	3.1
DPDZ(MDCHI)	DPSI/DZ (CHI PSI=CONSTANT)	RA	3.1
WIDTH	WIDTH OF DISTRIBUTION OF CHI MESH POINTS	R	3.1
NCHI	*NUMBER OF CHI INTERVALS IN UPPER HALF-PLANE	I	3.1
NPOL	*TOTAL NUMBER OF CHI INTERVALS	I	3.1
NPSI	*NUMBER OF S INTERVALS	I	3.1
NSHIFT	PERFORM SHIFT IN NQ	I	3.1

C3.2 NUMERICAL VARIABLES

VERSION 10 LDV MARCH 1986 CRPP LAUSANNE

COMMON/COMNUM/

AI1	INTEGRAND FOR Q INTEGRAL	R	3.2
AI2	INTEGRAND FOR DQ/DPSI INTEGRAL	R	3.2
AJR	CURRENT DENSITY	R	3.2
AR(201)	R DURING ANALYTICAL INTEGRATION	RA	3.2
AZ(201)	Z DURING ANALYTICAL INTEGRATION	RA	3.2
BP	POLOIDAL MAGNETIC FIELD	R	3.2
CPI	3.141592653589793	R	3.2
DBP2	PSI DERIVATIVE OF BP**2	R	3.2
DPR	DPSI/DR	R	3.2
DPZ	DPSI/DZ	R	3.2
FIT(16)	FIT PARAMETERS	RA	3.2
PSILIM	PSI AT LIMITER	R	3.2
XINT1(201)	INTEGRAL VALUES FOR Q AND CHI	RA	3.2
XINT2(201)	INTEGRAL VALUES FOR NON-ORTHOGONALITY	RA	3.2
LENGTH	*NB.OF ELEMENTS OF A MATRIX BLOCK	I	3.2

NAN	*NUMBER OF ANALYTIC PSI SURFACES	I	3.2
NANL	LEFT R COUNTER FOR ANALYTICAL FIT	I	3.2
NANR	RIGHT R COUNTER FOR ANALYTICAL FIT	I	3.2
NANZ	UPPER Z COUNTER FOR ANALYTICAL FIT	I	3.2
NCOLMN	*RANK OF A MATRIX BLOCK	I	3.2
NR	*NUMBER OF EQUILIBRIUM MESH POINTS IN R	I	3.2
NTURN	NUMBER OF TURNS FOR BALOONING CRITERION	I	3.2
NUM	MAX(NAN+1,SQRT(NPSI)+1)	I	3.2
NZ	*NUMBER OF EQUILIBRIUM MESH POINTS IN Z	I	3.2

C3.3 AUXILIARY VARIABLES FOR LION3 AND 4

VERSION 10 LDV MARCH 1986 CRPP LAUSANNE

COMMON/COMAUX/

CA(MDOVL)	OVERLAP SUBBLOCK OF MATRIX A	CA	3.3
CONA(6,6)	LOCAL (CELL) CONTRIBUTION TO A	CA	3.3
XC1(8)	CONSTANTS C-J OF WEAK FORM TERMS	CA	3.3
XETA(5)	CONSTANTS OF TEST-FUNCTIONS	CA	3.3
XKSI(5)	CONSTANTS OF UNKNOWNS	CA	3.3
XM(6,6)	CONTRIBUTION OF ONE TERM OF THE WEAK FORM	CA	3.3
XVETA(6)	VECTOR OF COEFFICIENTS FOR TEST-FUNCTIONS	CA	3.3
XVKSI(6)	VECTOR OF COEFFICIENTS FOR UNKNOWNS	CA	3.3
XF(16)	BASIS FUNCTIONS AT MESH POINTS	RA	3.3
NPLAC(6)	GLOBAL NUMBERING OF CELL MESH POINTS	IA	3.3
NLQUAD	QUADRATIC TERM IN THE WEAK FORM	L	3.3

C3.4 VECTORS FOR LION4

VERSION 10 LDV MARCH 1986 CRPP LAUSANNE

COMMON/COMVEC/

U(MDCOL)	VECTOR OF UNKNOWS FOR ONE BLOCK	CA	3.4
UT	TEMPORARY STORAGE	C	3.4
VA(MDCOL)	TEMPORARY STORAGE	CA	3.4
X(MDCOL)	VECTOR OF UNKNOWNS FOR ONE BLOCK	CA	3.4
XOHMR(MDIN2)	OHM VECTOR FOR POWER AT ANTENNA	CA	3.4
XT(MDCOMP)	TOTAL VECTOR OF UNKNOWNS	CA	3.4
XDCHI(MDIN2)	DELTA-CHI AT PLASMA SURFACE	RA	3.4
XDTH(MDIN2)	DELTA-THETA AT PLASMA SURFACE	RA	3.4

C3.5 NUMERICAL VARIABLES FOR LION4

VERSION 10 LDV MARCH 1986 CRPP LAUSANNE

COMMON/COMIVI/

EPSMAC	*ROUND-OFF ERROR OF COMPUTER	R	3.5
XNORM	VECTOR NORM SQUARED	R	3.5
M1	RANK OF MATRIX OVERLAP SUBBLOCK	I	3.5
M11	M1+1	I	3.5
M12	M1+M2 = RANK OF MATRIX BLOCK	I	3.5
M2	RANK OF MATRIX BLOCK - M1	I	3.5
N	NB. OF MATRIX BLOCKS (=NPSI)	I	3.5
NCOMP	NB. OF ELEMENTS OF SOLUTION VECTOR	I	3.5
NCONV		I	3.5

NEG		I	3.5
NIT		I	3.5
NITMAX		I	3.5
NLONG	NB. OF ELEMENTS IN A MATRIX BLOCK	I	3.5
NPIN(14)	INPUT PARAMETERS FOR ALGEBRAIC SOLVER	IA	3.5
NPOUT(14)	OUTPUT PARAMETERS FOR ALGEBRAIC SOLVER	IA	3.5
NSING	SINGULARITY INDICATOR (=-1 IF A IS SING.)	I	3.5

C5.1 CONTROL VARIABLES

VERSION 10 LDV MARCH 1986 CRPP LAUSANNE

COMMON/COMCON/

AHEIGT	*HEIGHT OF 2-D PLOTS	R	5.1
ALARG	*WIDTH OF 2-D PLOTS	R	5.1
ANGLE(16)	*TOROIDAL CUTS (DEGREES)	RA	5.1
ARSIZE	*SIZE OF ARROWS	R	5.1
ASYMB	*SIZE OF SYMBOLS	R	5.1
NCONTR	*NUMBER OF CONTOUR LINES	I	5.1
NFIG	*NUMBER OF TOROIDAL CUTS	I	5.1
NMESH	AUTOMATIC IRREGULAR S-MESH	I	5.1
NTCASE	*=2:SOLOVEV, =3:NUMERICAL EQUILIBRIUM	I	5.1
NLOTP0	*GENERAL LINE-PRINTER OUTPUT SWITCH	L	5.1
NLOTP1(4)	*OUTPUT SWITCHES FOR LION1	LA	5.1
NLOTP2(5)	*OUTPUT SWITCHES FOR LION2	LA	5.1
NLOTP3(2)	*OUTPUT SWITCHES FOR LION3	LA	5.1
NLOTP4(5)	*OUTPUT SWITCHES FOR LION4	LA	5.1
NLOTP5(25)	*OUTPUT SWITCHES FOR LION5	LA	5.1
NLPLO5(25)	*PLOT SWITCHES FOR LION5	LA	5.1
NLTORE	SELECTS THE TOROIDAL GEOMETRY	L	5.1
NLY		L	5.1

C5.2 I/O DISK CHANNELS NUMBERS

VERSION 10 LDV MARCH 1986 CRPP LAUSANNE

COMMON/COMOUT/

ITEST		I	5.2
MEQ	*EQUILIBIUM QUANTITIES	I	5.2
NDA	*MATRIX A	I	5.2
NDB		I	5.2
NDES	*R,Z COORDINATES AND NORMALS	I	5.2
NDLT	*DECOMPOSED MATRIX L,D,U	I	5.2
NDORY	*NUMERICAL EQUILIBRIUM	I	5.2
NDS	*SOLUTION VECTOR	I	5.2
NDSCRC	*SCRATCH SPACE	I	5.2
NPRNT	*LINE-PRINTER OUTPUT	I	5.2
NSAVE	*NAMELIST LINK LION1 TO 5	I	5.2
NSCRTC	*SCRATCH SPACE	I	5.2
NSUR	*PLASMA SURFACE	I	5.2
NVAC	*VACUUM QUANTITIES	I	5.2

---

9. BLANK COMMON

C9.1 MAPPING QUANTITIES FOR LION1

VERSION 2C 14/9/79 RG CRPP LAUSANNE

COMMON// (COMMAP)

A1(NRZ)	CONSTANT COEFFICIENT	RA	9.1
A2(NRZ)	COEFFICIENT FOR R**2	RA	9.1
A3(NRZ)	COEFFICIENT FOR R**4	RA	9.1
A4(NRZ)	COEFFICIENT FOR Z**2	RA	9.1
A5(NRZ)	COEFFICIENT FOR Z**4	RA	9.1
A6(NRZ)	COEFFICIENT FOR R**2*Z**2	RA	9.1
APP(10)	PARAMETERS FOR ANALYTICALLY GIVEN DP/DPSI	RA	9.1
ATTP(10)	PARAMETERS FOR T*DT/DPSI	RA	9.1
BETRZ(NR+2NZ)	NON ORTHOGONALITY IN CHI	RA	9.1
CHIRZ(NR+2NZ)	CHI(R,Z) AT CROSS POINTS WITH PSI=CONSTANT	RA	9.1
CPSEQ(NR,NZ)	PSI(R,Z) FROM EQUILIBRIUM CODE	RA	9.1
EQPS(NR)	DP/DPSI(R) GIVEN POINTWISE	RA	9.1
EQR(NR)	R MESH FROM EQUILIBRIUM	RA	9.1
EQT(NR)	T(R) GIVEN POINTWISE	RA	9.1
EQZ(NZ)	Z MESH FROM EQUILIBRIUM	RA	9.1
RAXIS	POSITION OF MAGNETICAL AXIS (IN EQU. UNITS)	R	9.1
RMAG	POSITION OF MAGNETICAL AXIS (IN ERATO=1)	R	9.1
RPSI1	PSI AT MAGNETICAL AXIS (IN EQU. UNITS)	R	9.1
RRO(NRZ)	RHO(PSI=CONSTANT)	RA	9.1
RRS(NRZ)	R(PSI=CONSTANT)	RA	9.1
RZS(NRZ)	Z(PSI=CONSTANT)	RA	9.1
TETA(NRZ)	TETA(PSI=CONSTANT)	RA	9.1
TLIM	ERATO T(AXIS)= 1 FIXED WHILE SCALING	R	9.1
To	T(AXIS) IN EQUILIBRIUM UNITS	R	9.1
ILOC(NCHI)	COUNTER FOR POLYNOMIAL WHICH CUTS CHI=CONST	IA	9.1
NRZ	NUMBER OF R-Z CUTS WITH PSI=CONSTANT	I	9.1
NRZS	NRZ(PSI AT SURFACE)	I	9.1

C9.2 VACUUM QUANTITIES FOR LION2

VERSION 10 LDV MARCH 1986 CRPP LAUSANNE

COMMON// (COMVID)

ANTR(MDIN2)	ANTENNA VECTOR	CA	9.2
OHMR(MDIN2)	OHM VECTOR	CA	9.2
REASCR	REACTANCE SCALAR	C	9.2
SAUTR(MDIN2)	JUMP ACROSS ANTENNA SURFACE	CA	9.2
SAUTX(MDIN2)	TEMPORARY	CA	9.2
SOURCE(MDIN2)	SOURCE VECTOR	CA	9.2
CA	CONSTANT TO DEFINE SHELL	R	9.2
CB	#	R	9.2
CC	#	R	9.2
D2ROP	D**2RHO/DTHETA**2 AT MID-POINT	R	9.2
DC(MD2CP2)	DELTA-CHI	RA	9.2
DRODT(4)	DRHO/DTHETA AT INTEGRATION POINTS	RA	9.2
DROPDT(4)	DRHOPRIME/DTHETA	RA	9.2

G(MDIN2,MDIN2,13)		
	ALL MATRICES	RA 9.2
QB	SAFETY FACTOR AT PLASMA SURFACE	R 9.2
RO(4)	RHO AT INTEGRATION POINTS	RA 9.2
RO2	RHO AT THE CENTER	R 9.2
RO2P	RHO PRIME AT THE CENTER	R 9.2
ROP(4)	RHO PRIME AT INTEGRATION POINTS	RA 9.2
SR(MD2CP2)	R(CHI) DEFINING PLASMA SURFACE	RA 9.2
SZ(MD2CP2)	Z(CHI) DEFINING PLASMA SURFACE	RA 9.2
T(MD2CP2)	THETA AT CHI MESH POINTS	RA 9.2
TB	TOROIDAL MAGNETIC FLUX AT PLASMA SURFACE	R 9.2
TH(MD2CP2)	THETA AT CENTER OF CHI MESH	RA 9.2
TP(4)	THETA PRIME AT INTEGRATION POINTS	RA 9.2
TT(4)	THETA AT INTEGRATION POINTS	RA 9.2
NDIM	DIMENSION OF MATRICES	I 9.2

C9.3 MATRIX BLOCKS FOR LION 3 AND LION4

VERSION 10 LDV MARCH 1986 CRPP LAUSANNE

COMMON// (COMMTR)

A(MDLENG)	MATRIX BLOCK OF DISCRETIZED WEAK FORM	CA 9.3

C9.5 OUTPUT AND PLOT QUANTITIES FOR LION5

VERSION 10 LDV MARCH 1986 CRPP LAUSANNE

COMMON// (COMPLO)

BNL	NORMAL COMPONENT OF WAVE MAGNETIC FIELD	C 9.5
BPARL	PARALLEL COMP. OF WAVE MAGNETIC FIELD	C 9.5
BPL	PERP. COMP. OF WAVE MAGNETIC FIELD	C 9.5
DVDC	DV/DCHI	C 9.5
DXDC	DX/DCHI	C 9.5
DXDS	DX/DS	C 9.5
ENL	NORMAL COMPONENT OF WAVE ELECTRIC FIELD	C 9.5
EPL	PERP. COMP. OF WAVE ELECTRIC FIELD	C 9.5
FREN(13,MDPSI)	FOURIER DECOMPOSITION IN CHI OF E-N	CA 9.5
FREP(13,MDPSI)	FOURIER DECOMPOSITION IN CHI OF E-PERP	CA 9.5
FRINT(7,MDCHI)	INTEGRAL FOR FOURIER DECOMPOSITION	CA 9.5
VC	V	C 9.5
XC	X	C 9.5
ABSPOW(MDPSI)	POWER ABSORBED ON PSI=CONST.	RA 9.5
APHI	TOROIDAL ANGLE PHI	R 9.5
CCHI(MDIN2)	CHI VALUES AT CENTER OF CELLS	RA 9.5
CCR(MDPSI,MDCHI)		
	R AT CENTER OF CELLS	RA 9.5
CCS(MDPSI)	S VALUES AT CENTER OF CELLS	RA 9.5
CCZ(MDPSI,MDCHI)		
	Z AT CENTER OF CELLS	RA 9.5
CDEVIA	WIDTH OF POWER DISTRIBUTION IN CHI	R 9.5
CELPOW(MDPSI,MDIN2)		
	POWER ARBSORBED IN THE CELLS	RA 9.5
CHIPOW(MDIN2)	POWER ABSORBED ON CHI=CONST.	RA 9.5

CMEAN	CENTER OF POWER DISTRIBUTION IN CHI	R	9.5
CNR(MDPSI,MDCHI)	NORMAL TO PSI=CONST., R COMPONENT	RA	9.5
CNZ(MDPSI,MDCHI)	NORMAL TO PSI=CONST., Z COMPONENT	RA	9.5
CPL	POWER ABSORBED IN A CELL	R	9.5
CPLE	POWER IN A CELL DUE TO NU	R	9.5
DENPOW(MDPSI,MDIN2)	POWER ABSORPTION DENSITY	RA	9.5
DPL	POWER ABSORPTION DENSITY AT CENTER OF CELL	R	9.5
DPLE	POWER ABSORPTION DENSITY DUE TO NU	R	9.5
ECHEL	SCALE FACTOR FOR 2-D PLOTS	R	9.5
ELEPOW	POWER DUE TO NU	R	9.5
FLUPOW(MDPSI1)	POWER ABSORBED INSIDE PSI=CONST.	RA	9.5
SDEVIA	WIDTH OF POWER DISTRIBUTION IN S	R	9.5
SFLUX(MDPSI)	POYNTING FLUX ACROSS PSI=CONST.	RA	9.5
SMEAN	MINOR RADIUS OF HALF POWER ABSORPTION	R	9.5
SN(MDPSI,MDIN2)	NORMAL COMPONENT OF POYNTING	RA	9.5
SNL	NORMAL COMPONENT OF POYNTING	R	9.5
SPAR(MDPSI,MDIN2)	PARALLEL COMPONENT OF POYNTING	RA	9.5
SPARL	PARALLEL COMPONENT OF POYNTING	R	9.5
SPERP(MDPSI,MDIN2)	PERP. COMPONENT OF POYNTING	RA	9.5
SPL	PERP. COMP. OF POYNTING	R	9.5
VOUT1(MDPSI,MDIN2)	TEMPORARY STORAGE	RA	9.5
VOUT2(MDPSI,MDIN2)	TEMPORARY STORAGE	RA	9.5
XS(MDRZ)	R COORDINATES OF PLASMA SURFACE	RA	9.5
YS(MDRZ)	Z COORDINATES OF PLASMA SURFACE	RA	9.5
NRZSUR	NUMBER OF POINTS FOR PLOTTING THE SURFACE	I	9.5

/